

Title	グラフェンナノ電子機械（NEM）スイッチングデバイスの研究
Author(s)	王, 文楨
Citation	
Issue Date	2017-06
Type	Thesis or Dissertation
Text version	ETD
URL	http://hdl.handle.net/10119/14754
Rights	
Description	Supervisor:水田 博, マテリアルサイエンス研究科, 博士

Doctoral Dissertation

Graphene-based Nanoelectromechanical
(NEM) Switching Devices

Wenzhen Wang

Supervisor: Prof. Hiroshi Mizuta

School of Materials Science

Japan Advanced Institute of Science and Technology

June 2017

DECLARATION

I, Wenzhen Wang, hereby declare that this thesis, which is submitted for the assessment of my research leading to the degree of Doctor of Philosophy, entirely originated from my own study. It includes nothing, which is taken from the work completed by other researchers without proper citation and acknowledgement. This thesis has not been previously submitted, in part or whole, to any University of the institution for any degree, diploma, or other qualification.

Signed: _____

Date: _____

–

Wenzhen WANG

Japan Advanced Institute of Science and Technology

ABSTRACT

Energy and Environment Research Division

School of Material Science

Mizuta Laboratory

Doctor of Philosophy

Graphene-based Nanoelectromechanical (NEM) Switching Devices

BY WENZHEN WANG

Nanoelectromechanical (NEM) switch has become one of the promising candidates to overcome the limitations of conventional CMOS technology, which can offer extremely low leakage current, abrupt switching ($SS < 3$ mV/dec) and high ON/OFF ratio. By taking the advantages of graphene, which are atomic thin and high Young's modulus, we can further reduce the pull-in voltage and scale down the size of graphene NEM switches. An autonomous GNEMS sensor system was proposed by Prof. Hiroshi Mizuta in 2013. Graphene NEM switch is planned to be utilized as a power gating device to shut down the power supply at the sleep-mode of sensor, thus saving the total energy dissipation. Currently, the critical issue, which hinders the development of graphene NEM contact switches, is the device reliability. The irreversible stiction at the contact often occurred, as the most common failure mode of graphene NEM switches. Au-C chemical bonding was recognized, originating from the permanent stiction, which should be excluded from the switch design.

The aim of this study is to achieve stable switching operations of graphene NEM switches. To avoid the direct contact between graphene to metal, naturally grown oxide was selected as the contact material with graphene. The novel graphene contact devices, which combined transmission line method pattern (TLM) pattern with graphene NEM top-gated switches, were fabricated, intended to comprehensively investigate the graphene contact issues. In addition, periodic concave patterns were introduced into the contact interface to reduce the stiction. Static contact between graphene and Cr were studied from the TLM patterns, which indicated slightly negative values of static contact resistance owing to the doping from the metal and the substrate. All the dynamic GNEM contact switches showed clear pull-in operations, however, none of those

switches demonstrated the pull-out operations owing to a strong adhesive force. By analysing the measured contact resistance and contact pressure, plastic deformation of the Cr₂O₃ layer was discussed at the graphene-Cr₂O₃ contact interface, which resulted in the increase of vdW force, thus the irreversible stiction.

To reduce the stiction force, the periodic concave patterns at the bottom surface of the top gate were changed to the tip structures to further reduce the contact area. Besides, comparing with the geometry of GNEM switches studied in dynamic contact, shorter graphene beam length and larger air gap distance from suspended graphene to top gate were applied to the new design, aiming to increase the mechanical restoring force against the adhesive force. Additionally, the thickness of Cr₂O₃ was increased to around 2 nm to avoid the Joule heating due to the tunnelling current. After characterizing the redesigned graphene NEM switches, the hysteresis with clear pull-in and pull-out operations was observed first, but the pull-out operation was not observed in the 2nd cycle and after. We have attributed this phenomenon to the stored charge in the thicker Cr₂O₃ layer, which induced extra stiction force, resulting in the non-volatile operation. Moreover, an unexpected bi-stable NEM switch was realized experimentally by reversing the bias voltage on top electrodes. This was mainly due to the charge injection with opposite polarity to the Cr₂O₃, canceling the build-up charge in dielectric and further reducing the stiction force. A novel graphene NEM non-volatile logic device was interpreted from the bi-stable switching behaviour, offering the possibility for the instant-off and instant-on applications, further to be applied as a sleep transistor to the system to cut-off the standby energy consumption.

Keywords: NEMS, Graphene, Switch, Contact, Charge storage

ACKNOWLEDGEMENTS

First of all, I would like to express my sincere acknowledgement to my supervisor, Professor Hiroshi Mizuta for all his support and guidance on not only research but also life. It is my greatest honor to be a member of Mizuta Lab. Thanks for his patience and suggestions along the years of my PHD study. Without his invaluable help and encouragement, there is no chance for me to complete this study. His insight towards to the research and his seriousness on the physics behind the results allow me to see a deeper and larger image of my study, which will certainly benefit the rest of my life.

I would also like to show my great appreciation to Dr. Muruganathan Manoharan in Mizuta Lab for all his help and support. The knowledge and skills he taught me will benefit my future career life. Moreover, he gives me a vivid example of an excellent researcher in every aspect. Many thanks for not giving me up at last, and I do need to apologize to him for my poor characteristics.

Besides my supervisors, I would to acknowledge Professor Eisuke Tokumitsu, Professor Mikio Koyano, Professor Hideyuki Murata, and Professor Daniel Moraru, who are my PHD qualification committee, for the kind suggestions and respective expertise, which helped me to review my study from a multidisciplinary view, thus giving me a more comprehensive understanding towards to my research.

I also would like to acknowledge my friends in Mizuta lab, who are Dr. Marek Edward Schmidt, Takuya Iwasaki, Jothiramalingam Kulothungan, and Ahmed Hammam. Thanks for their kind discussion and support during my study. It is my honour to be their friends and working with them daily.

Last but not the least, I would like to thank my family members, who are behind me and giving me huge support. Without them, I would not be able to reach to the final stage.

CONTENTS

1	INTRODUCTION.....	1
1.1	MOORE`S LAW AND CMOS LIMITATIONS	1
1.2	GRAPHENE	3
1.2.1	<i>Electrical properties of graphene</i>	4
1.2.2	<i>Mechanical properties of graphene</i>	4
1.3	REVIEW OF RELEVANT LITERATURE	5
1.3.1	<i>MEMS and MEMS switches</i>	5
1.3.2	<i>NEMS and NEMS switches</i>	7
1.3.3	<i>Non-Volatile logic</i>	12
1.4	MOTIVATION AND CONTRIBUTION	13
1.5	THESIS STRUCTURE.....	14
1.6	REFERENCES	16
2	RELATED THEORY	19
2.1	ELECTROMECHANICAL ANALYSIS	19
2.1.1	<i>Pull-in analysis</i>	19
2.1.2	<i>Pull-out analysis</i>	21
2.2	THE SHORT RANGE FORCES	22
2.3	CONTACT STUDY.....	23
2.3.1	<i>Static contact of graphene</i>	24
2.3.2	<i>Dynamic contact of graphene</i>	27
2.4	POLARIZATION/CHARGING OF DIELECTRIC	28
2.5	REFERENCE.....	32
3	FABRICATION OF GRAPHENE NEM SWITCHING DEVICES.....	35
3.1	INTRODUCTION	35
3.2	FABRICATION OF SWITCHES WITH LOCAL BOTTOM ELECTRODES.....	36
3.2.1	<i>Fabrication Process</i>	36
3.2.2	<i>Comparison</i>	45
3.3	FABRICATION OF SWITCHES WITH LOCAL TOP ELECTRODES	46
3.3.1	<i>Fabrication Process</i>	46
3.3.2	<i>Fabrication of dynamic contact device</i>	46
3.4	SUMMARY.....	51
3.5	REFERENCE.....	52

4	STUDY OF CONTACTS FOR GRAPHENE NEM SWITCHES	53
4.1	INTRODUCTION	53
4.2	GRAPHENE NEM SWITCHES WITH LOCAL BOTTOM ELECTRODES	53
4.3	GRAPHENE CONTACT DEVICE	55
4.3.1	<i>Static contact study</i>	56
4.3.2	<i>Dynamic contact</i>	57
4.3.3	<i>Finite element method simulation</i>	61
4.3.4	<i>Comparison with classic dynamic contact modeling</i>	63
4.4	SUMMARY	65
4.5	REFERENCES	67
5	CHARACTERIZATION OF GRAPHENE NEM SWITCHING	
	DEVICES.....	69
5.1	INTRODUCTION	69
5.2	DEVICE STRUCTURE AND DIMENSION	70
5.3	RESULTS AND DISCUSSION	72
5.3.1	<i>Pull-in characterization</i>	72
5.3.2	<i>Type of deformation</i>	74
5.3.3	<i>Bi-stable NEM switch</i>	75
5.4	SUMMARY	81
5.5	REFERENCE	82
6	SUMMARY AND FUTURE WORK.....	83
6.1	SUMMARY	83
6.2	FUTURE WORK	84

LIST OF TABLES

TABLE 2-1 SUMMARY OF MEASURED STATIC GRAPHENE-METAL CONTACT RESISTANCE	26
TABLE 3-1 THREE DIFFERENT DRY ETCHING CONDITIONS	38
TABLE 3-2 PMMA ETCHING RATES UNDER THREE ETCHING CONDITIONS.....	39
TABLE 4-1 TABLE DEVICE PARAMETERS OF THE DYNAMIC CONTACT GNEM SWITCHES, A-D.	57
TABLE 5-1 DEVICE PARAMETERS OF FOUR MEASURED CONTACT SWITCHES	70
TABLE 5-2 DEVICE PARAMETERS OF FOUR MEASURED CONTACT SWITCHES	73

LIST OF FIGURES

FIGURE 1.1 THE TREND OF POWER CONSUMPTION WITH CMOS SCALING [2].	2
FIGURE 1.2 COMPARISON OF TRANSFER CHARACTERISTICS BETWEEN A CONVENTIONAL MOSFET AND OTHER EMERGING TECHNOLOGY.	3
FIGURE 1.3 UTILIZING GRAPHENE TO BUILD ALL-DIMENSIONAL CARBON MATERIALS [4].	4
FIGURE 1.4 MEASURED ELASTIC CONSTANT OF MONOLAYER GRAPHENE [7]	5
FIGURE 1.5 SCHEMATIC OF A MICRO-GRIPPER AS AN EXAMPLE OF ELECTROSTATIC-ACTUATED MEM DEVICE.	6
FIGURE 1.6 (A) SEM IMAGE OF THE FABRICATED SUSPENDED-GATE MOSFET. (B) SWITCHING CHARACTERIZATION OF THE SUSPENDED-GATE MOSFET [16].	7
FIGURE 1.7 (A) SEM IMAGE OF THE FABRICATED NANOWIRE-BASED SWITCHING FET. (B) SWITCHING CHARACTERIZATION OF THE NANOWIRE-BASED SWITCHING FET [17].	9
FIGURE 1.8 (A) SEM IMAGE OF THE FABRICATED CNT-BASED CAPACITIVE NEM SWITCH. (B) C-V CHARACTERIZATION OF THE CNT-BASED CAPACITIVE NEM SWITCH [21].	10
FIGURE 1.9 (A) AFM IMAGE OF THE FABRICATED BILAYER GRAPHENE NEM SWITCH. (B) SWITCHING CHARACTERIZATION OF THE BILAYER GRAPHENE NEM SWITCH WITH LOCAL BOTTOM ELECTRODE [28].	11
FIGURE 1.10 MECHANISM OF A NEM MEMORY CELL [30].	12
FIGURE 1.11 THE AUTONOMOUS GNEMS SENSOR SYSTEM PROPOSED BY PROF. HIROSHI MIZUTA [31].	13
FIGURE 2.1 1D PARALLEL PLATE MODEL TO CALCULATE THE VOLTAGE OF PULL-IN EFFECT	19
FIGURE 2.2 1D PARALLEL PLATE MODEL TO CALCULATE THE VOLTAGE OF PULL-OUT EFFECT	21
FIGURE 2.3 DIFFERENCE BETWEEN TWO VAN DER WAALS FORCE APPROXIMATION AT THE VERY SHORT RANGE [8].	23
FIGURE 2.4 CHANNEL WIDTH TYPE AND AREA TYPE OF CONTACT RESISTIVITY [15].	25
FIGURE 2.5 A TYPICAL TLM PATTERN TO EXTRACT THE CONTACT RESISTANCE	26

FIGURE 2.6 RELATIONSHIP BETWEEN TIME AND DIFFERENT TYPES OF POLARIZATION [26]	29
FIGURE 2.7 TWO POLARIZATION AND CHARGING MECHANISM FOR THE (A) CONTACTLESS MODE (B) CONTACT MODE OF NEM/MEM SWITCHES [28]	30
FIGURE 2.8 IN CONTACT STATE, CHARGING AND DISCHARGING OCCUR FROM BOTH DIRECTIONS.	31
FIGURE 3.1 FABRICATION PROCESS OF GRAPHENE NEM SWITCHES WITH LOCAL ACTUATION ELECTRODES.	37
FIGURE 3.2 RELATIONSHIPS BETWEEN ETCHED PMMA THICKNESS AND ETCHING DURATION UNDER THREE DRY ETCHING CONDITIONS.	39
FIGURE 3.3 (A) OPTICAL MICROSCOPY IMAGE OF PRE-DEFINED TRENCHES. (B) SEM IMAGE OF PRE-DEFINED TRENCHES. (C) AND (D) TOPOGRAPHIC IMAGE OF A PRE-DEFINED TRENCH AND THE EXTRACTED PROFILE.	40
FIGURE 3.4 (A) AND (B) AFM IMAGES OF PRE-DEFINED TRENCHES WITH EVAPORATED SiO ₂ . (C) EXTRACTED LINE PROFILE OF THE TRENCH WITH SiO ₂ .	41
FIGURE 3.5 (A)-(D) OPTICAL AND SEM IMAGES OF TWO EXFOLIATED GRAPHENE FLAKES LYING ON PRE-DEFINED TRENCHES	42
FIGURE 3.6 (A) AND (B) OPTICAL IMAGES OF THE DEVICE BEFORE AND AFTER DEPOSITING THE METAL CONTACT.	43
FIGURE 3.7 (A) PMMA ETCHING MASK TO PATTERN RIBBON-SHAPED GRAPHENE. (B) ETCHING MASK TO PATTERN TWO GRAPHENE CANTILEVERS.	44
FIGURE 3.8 (A) AND (B) TWO FABRICATED GRAPHENE-BASED CANTILEVER-TYPE NEM SWITCHING DEVICES WITH LOCALLY ACTUATED ELECTRODES.	44
FIGURE 3.9 FABRICATION PROCESS OF GRAPHENE NEM SWITCH WITH LOCAL BOTTOM ACTUATION ELECTRODE BY USING A SACRIFICIAL POLYMER SPACER [3].	45
FIGURE 3.10 FABRICATION PROCESS OF THE LOCAL TOP ACTUATION ELECTRODE. [4]	46
FIGURE 3.11 (A) SCHEMATIC DIAGRAM OF THE STATIC CONTACT GNR DEVICE. (B) SCHEMATIC DIAGRAM OF THE DYNAMIC CONTACT GRAPHENE NEM DEVICES WITH DCUR AND DCPD. (C) FABRICATION PROCESS OF A GNEM SWITCH WITH PERIODIC PATTERNS ON THE TG.	48
FIGURE 3.12 THREE FABRICATED GRAPHENE STATIC CONTACT DEVICES WITH TLM PATTERN.	49

FIGURE 3.13 (A, B) AFM IMAGES OF HSQ PATTERN AND DEPOSITED SiO ₂ ON THE HSQ PATTERN. THE INSETS INDICATE THE SCHEMATICS OF THE PROCESS. (C) HEIGHT PROFILES MEASURED ALONG THE DOTTED RED AND SOLID GREEN LINES IN (A) AND (B). (D) DIMENSIONS OF THE DESIGNED HSQ SQUARES ARRAY. (E, F) AFM IMAGES OF THE DYNAMIC CONTACT GRAPHENE NEM DEVICE BEFORE AND AFTER DEPOSITING THE TGS. THE GRAY SOLID LINE IN (E) INDICATES THE PATTERNED GNR.	50
FIGURE 3.14 RELATIONSHIP BETWEEN vdW FORCE AND SEPARATION DISTANCE.	50
FIGURE 3.15 SEM IMAGES OF A TYPICALLY FABRICATED GRAPHENE CONTACT DEVICES.	51
FIGURE 4.1 DOUBLE-CLAMPED TYPE AND CANTILEVER TYPE OF GRAPHENE NEM SWITCHES	54
FIGURE 4.2 MEASUREMENT CONFIGURATIONS OF BOTH DOUBLE-CLAMPED TYPE AND CANTILEVER TYPE OF GRAPHENE NEM SWITCHES.	54
FIGURE 4.3 (A) AFM IMAGE OF CONTACT DEVICE D1 AND OPTICAL MICROSCOPY IMAGES OF DEVICES D2 AND D3. GREY SOLID LINES (D2, D3) INDICATE THE LOCATION AND SHAPE OF THE GNRs. (B) TLM FITTING FOR CONTACT DEVICES D1, D2, AND D3. OVERALL RESISTANCE OF D1 AND D2 AFTER BHF ETCHING. THE INSET SHOWS THE FITTING RESULTS FOR A SMALL RANGE OF INTERSPACING DISTANCES (0-1 μM).	56
FIGURE 4.4 (A, B) CHARACTERIZATION OF DYNAMIC CONTACT RESISTANCE OF TWO GRAPHENE-BASED NEM SWITCHES A AND B WITH UNIFORM ROUGHNESS ON TG (DCUR). INSETS: ITB-VTB CURVES OF THE 1ST SWITCHING OPERATION, AND THE TWO-TERMINAL MEASUREMENT CONFIGURATION FOR THE DYNAMIC CONTACT STUDY. (C) SEM IMAGE OF DEVICE A AFTER THE MEASUREMENT; SCALE BAR: 0.5 μM. SCHEMATIC DIAGRAM OF GRAPHENE-TG CONTACT WITH THE UNIFORM ROUGHNESS SURFACE (DCUR). (D, E) CHARACTERIZATION OF DYNAMIC CONTACT RESISTANCE OF SWITCHES C AND D WITH THE PERIODIC PATTERNS ON THE BOTTOM SURFACE OF THE DYNAMIC CONTACT (DCPP), AS SHOWN IN (F). INSET: ITB-VTB CURVES OF THE FIRST SWITCH OPERATION. (F) SEM IMAGE OF DEVICE D AFTER THE MEASUREMENT; SCALE BAR: 0.3 μM. SCHEMATIC DIAGRAM OF GRAPHENE-TG CONTACT WITH THE PERIODIC PATTERNS.	58

- FIGURE 4.5 (A) FEM MODEL OF A GRAPHENE NEM SWITCH WITH THE PERIODICALLY PATTERNED ELECTRODE. DIMENSIONS ARE BASED ON THE MEASURED SWITCH D. (B) ONE-DIMENSIONAL PLOT OF BEAM DISPLACEMENT WITH THE APPLIED VOLTAGE. INSET: 1D PLOT OF BEAM DISPLACEMENT AFTER INITIAL PULL-IN. (C) BEAM DISPLACEMENT AT PULL-IN VOLTAGE OF 1.5 V. (D) BEAM DISPLACEMENT IN THE PERIODIC CONCAVE PATTERNS (4.5 V). DISPLACEMENTS IN (C) AND (D) ARE INDICATED BY THE SAME COLOUR BAR. 62
- FIGURE 4.6 CONTACT FORCE VERSUS CONTACT RESISTANCE CURVES FROM MEASURED GENM SWITCHES B, C, AND D AND TWO DYNAMIC CONTACT MODELS OF ELASTIC AND PLASTIC DEFORMATIONS. DOTTED LINES: SHIFTED CONTACT RESISTANCE OF TWO CLASSICAL MODELS TO COMPARE WITH THE MEASURED RESULTS. MAGNIFIED PLOTS: COMPARISON BETWEEN THE EXPERIMENTAL RESULTS WITH TWO CONTACT MODELS FOR SMALL CONTACT FORCE RANGES. 65
- FIGURE 5.1 2D PEAK OF A GRAPHENE RAMAN SPECTROSCOPY WITH FOUR LORENTZIAN FITTING 70
- FIGURE 5.2 (A) DESIGN OF A TYPICAL NET-LIKE PATTERN OF HSQ (B) AFM IMAGE OF PATTERNED HSQ UNDER THE E-BEAM EVAPORATED SiO₂ (C) AND (D) EXTRACTED PROFILES FROM RED AND GREEN LINES. 71
- FIGURE 5.3 (A) OPTICAL IMAGE OF A FABRICATED GNEM SWITCH. (B) SEM IMAGES OF PATTERNED A NEM CONTACT SWITCH WITH THE SUSPENDED GRAPHENE AND LOCAL TOP ELECTRODE. 72
- FIGURE 5.4 CHARACTERIZATION OF PULL-IN EFFECT OF FOUR GNEM SWITCHES. 73
- FIGURE 5.5 CONTACT FORCE VERSUS CONTACT RESISTANCE CURVES FROM MEASURED GENM SWITCHES A, AND B, AND TWO DYNAMIC CONTACT MODELS OF ELASTIC AND PLASTIC DEFORMATIONS. DOTTED LINES: SHIFTED CONTACT RESISTANCE OF TWO CLASSICAL MODELS TO COMPARE WITH THE MEASURED RESULTS. INSETS: MEASURED RESPONSES BETWEEN THE APPLIED VOLTAGE AND THE CURRENT FROM SWITCH A AND SWITCH B AFTER THE 1ST PULL-IN. 75
- FIGURE 5.6 (A) TYPICAL MEASUREMENT CONFIGURATION FOR CHARACTERIZING A NEM SWITCH. (B) NEW MEASUREMENT CONFIGURATION WITH A REVERSED BIASED 76
- FIGURE 5.7 CHARACTERIZATION OF SWITCH A WITH REVERSED BIAS CONFIGURATION AND NORMAL SWITCHING CONFIGURATION. 77
- FIGURE 5.8 COMBINATION OF ALL THE FOUR MEASUREMENT CYCLES (SWITCH A). 77

FIGURE 5.9 GRAPHENE NEM MEMORY STATES CORRESPONDING TO THE BEAM POSITIONS.	79
FIGURE 5.10 CHARACTERIZATION OF A BI-STABLE NON-VOLATILE LOGIC CELL (SWITCH D) WITH REVERSED BIAS CONFIGURATION AND NORMAL SWITCHING CONFIGURATION.	79
FIGURE 5.11 EXPLANATION OF CHARGE STORAGE WHEN APPLYING THE FORWARD BIAS AND REVERSE BIAS.	79
FIGURE 5.12 PULL-IN AND PULL-OUT EFFECT MEASURED FROM SWITCH B	80
FIGURE 5.13 A COMPARISON OF THE SCALABILITY BETWEEN SI-BASED NEM SWITCHING DEVICES AND GRAPHENE-BASED NEM SWITCHING DEVICES.	81

1 Introduction

1.1 MOORE'S LAW AND CMOS LIMITATIONS

In 1959, Richard Feynman's gave an impressive lecture "Plenty of Room at the Bottom", and he enlightened a new field where humans can manipulate and control things on a tiny scale, which was regarded as the beginning of nanotechnology. Six years later, Gordon Moore released his famous article "Cramming more components onto integrated circuit", and he had observed that the density of transistors per square inch would be doubled every year, although the pace was amended from every year to every 18 months, which is the origins of the term of Moore's law [1]. Now, we still keep benefiting from their foreseen deeply and widely in the modern life. The size of personal computer shrinks from the room-size to the palm-size, while the processing speed is even much faster. Our mobile phone has been redefined as a multi-functional device which consists of a digital camera, global position satellite (GPS) and music/video player. Accelerometers have been implanted into the airbag of a modern car and the controllers of game consoles, which make our life safer and more colourful.

However, it is not possible to maintain the exponential growth indefinitely, and the channel length of complementary metal-oxide-semiconductor field effect transistor (CMOS FET) has reached 14 nm until the year of 2017, which is close to the physical limitations. Moreover, while continue the miniaturization of the device to improve the performance of the chip, the standby power consumption of CMOS technology

becomes an inevitable and serious issue of the power dissipation. As shown in Figure 1.1, the leakage power is almost at the same level with the dynamic power when the gate length is lower than 40 nm [2]. Huge interests and attempts have been conducted to explore the novel technology beyond the conventional CMOS technology. Micro-electromechanical systems (MEMS) and nanoelectromechanical systems (NEMS) shrinking the moveable element from micrometer-scale to nanometer-scale become one promising direction to overcome the bottleneck of conventional technology due to the nearly zero leakage current and the adaptability of the harsh environment.

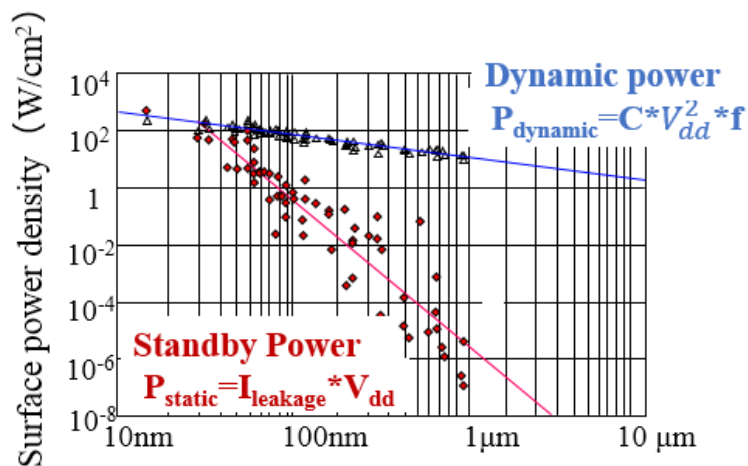


Figure 1.1 The trend of power consumption with CMOS scaling [2].

Besides, the subthreshold swing (SS), which is considered as a parameter to evaluate the switching behaviour of a transistor, is defined as the required voltage to modulate the source to drain current by one order of magnitude. The SS of conventional MOSFET is limited as 60 mV/dec at room temperature, while MEM/NEM switching devices have the strength of much smaller voltage swing, which is shown in Figure 1.2.

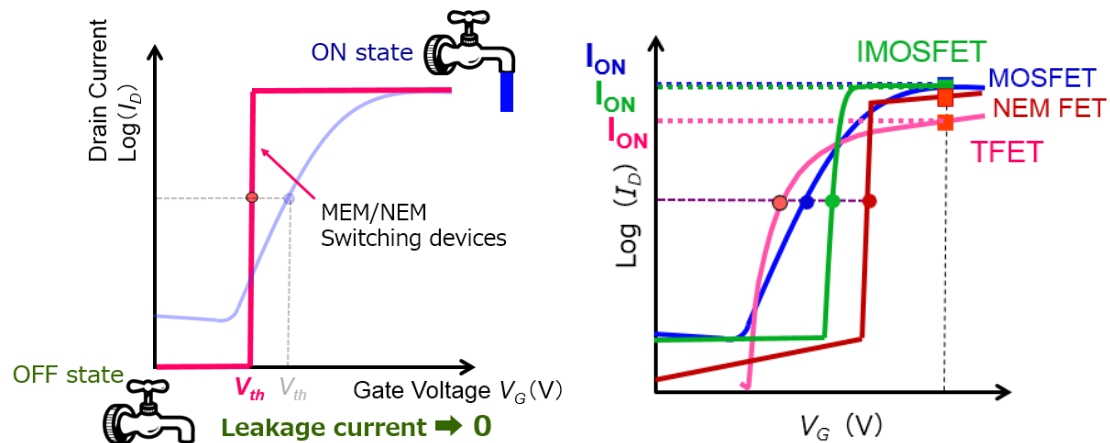


Figure 1.2 Comparison of transfer characteristics between a conventional MOSFET and other emerging technology.

A comparison between MOSFET and emerging technologies, which are tunnel FET(TFET), impact-ionization MOSFET (IMOSFET) is shown above. Although, from the structure point of view, both of TFET and IMOSFET look similar. They are based on different mechanisms, TFET is using tunneling process to have on current, while IMOSFET is utilizing the avalanche effect. Both of these two technologies can achieve sub-thermal switching. Currently, the issue of TFET is the low on current. IMOSFET has a relatively large threshold voltage and high off-current, which is not ideal for an ideal switching device. In terms of the NEM FET, the biggest advantage of NEM FET is the very small subthreshold voltage, which can achieve around 2 mV/dec on 2007 [16]. In addition, NEM FET keeps a low standby leakage current and large ON/OFF ratio. The high threshold voltage and reliability are still the problems of NEM FET.

Additionally, as the era of the Internet of things (IOT) is coming, there are extremely high demands on novel sensors, which requires a well-developed technique for power management. NEM switching device will be one of the promising candidates for this application to save the power consumption.

1.2 GRAPHENE

Graphene is an atomically-thick two-dimensional (2D) material, which consists of hexagonal lattice which is made from carbon atoms. Graphene originates from the bulk material graphite, which can be easily found from the pencil lead. Due to the difficulties of obtaining monolayer graphene with high quality, understanding of the intrinsic properties of graphene was limited at the beginning of the study. Thanks to Dr. Andre Geim and Dr. Konstantin Novoselov, who were awarded the Nobel Prize in Physics (2010), obtaining the free-standing and almost defect-free graphene flakes is no longer a tough task by simply mechanically exfoliating the graphite with the Scotch tape [3].

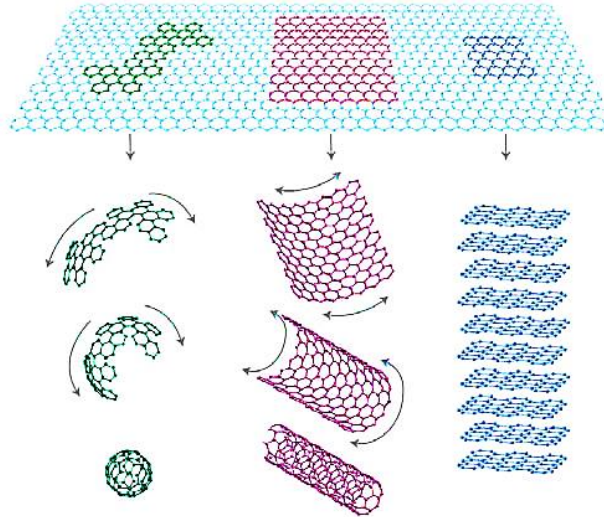


Figure 1.3 Utilizing graphene to build all-dimensional carbon materials [4].

1.2.1 ELECTRICAL PROPERTIES OF GRAPHENE

Comparing with other existing materials, Graphene has unique band structure. In simple words, the conduction band and valence band of graphene are connected at one point, known as the Dirac point, in other words, as the charge neutral point. Moreover, the linear dispersion relationships are observed from both the conduction band and valence band when the energy level is not far away from the charge neutral point. The effective electron mass of graphene is zero thanks to the linear relationship of momentum k and energy E . Due to this massless behavior, intrinsic suspended graphene possesses extremely high electron mobility, approaching to $200,000 \text{ cm}^2/\text{Vs}$ measured at the low temperature [5]. When the 2D graphene sheet contacting with the metal, since the limited density of states (DOS) near the Dirac point and the difference in the work function, the contact resistivity indicating the transport of charge carrier is less than $10^{-9} \Omega \text{ cm}^2$, which also plays an important role in the device performance [6].

1.2.2 MECHANICAL PROPERTIES OF GRAPHENE

Graphene, as a thin atomic layer of material, has the thickness of 0.42 nm. The in-plane stiffness of graphene, 340 N/m, was characterized from freely suspended circular shaped membranes by using the nano-indentation, corresponding to an impressively high Young's modulus of 1 TPa (Figure 1.4) [7]. The breaking strength was also reported from the same experiment, indicating to a bulk value of 130 GPa. Besides, breaking strain of 25% was investigated, and the graphene membranes were

easy to be broken under the nonlinear elastic regime. In the case of NEMS study, the mechanical properties of the moveable elements largely determine the performance and reliability of the device. These mechanical properties of graphene mentioned above are better than any of the thin-film materials under the use of NEM technology. In addition, graphene has another merit which is resistance to the natural oxidation, revealing that graphene-based NEM device has better reliability comparing with the device made from metals.

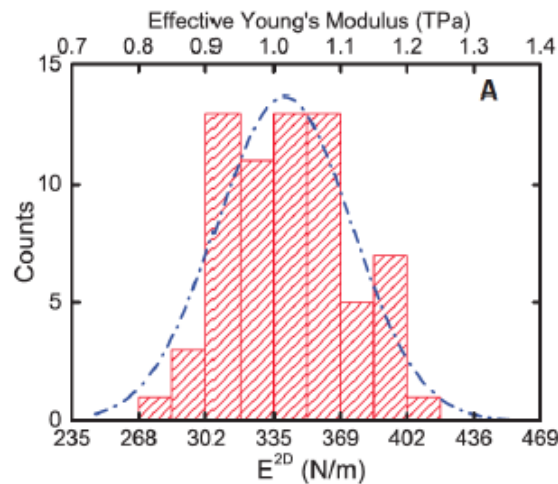


Figure 1.4 Measured elastic constant of monolayer graphene [7]

1.3 REVIEW OF RELEVANT LITERATURE

1.3.1 MEMS AND MEMS SWITCHES

Microelectromechanical system (MEMS) is a miniaturized engineering system which typically contains the MEMS components with the size ranging from micrometer scale to millimeter scale to perform specific functions (i.e., sensing, actuating and transducing). In general, a MEMS system has two main elements which are a sensor/actuator and a signal processing unit. Signals received from sensors or actuators are converted into readable forms by the converting unit [8].

An actuator driven by the external power sources is utilized to conduct the desired motion. There are four common actuating methods to achieve the motion of MEM devices, which are electrostatic forces, thermal forces, piezoelectric effect and shape memory alloys. The electrostatic switch is considered as a simple example of a simple actuator. In this thesis, we are mainly using electrostatic force to actuate the devices by

applying the voltage to metal electrodes. The configuration of electrostatic actuation is close to a two parallel-plate capacitor which charges two conducting plates in parallel and separate with a specific dielectric medium such as air and silicon dioxide. Direct-current (DC) voltage is applied to the conducting plates, resulting in the relative displacement of the movable plates from their original position due to the electrostatic forces [8]. The schematic of a micro-gripper as an example of the MEM device actuated by the electrostatic forces is displayed in Figure 1.5.

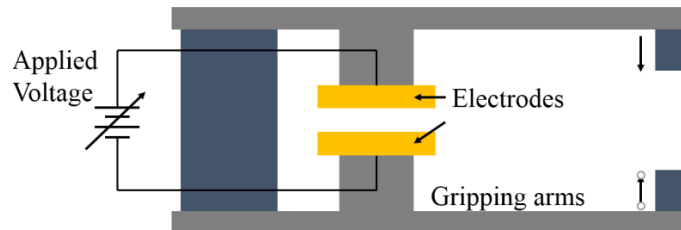


Figure 1.5 Schematic of a micro-gripper as an example of electrostatic-actuated MEM device.

The first MEM switch, which is a silicon-based membrane-shaped relay, was reported on 1979. After that, there were several conferences and journal papers studying about the MEM switches with different vertical moveable structure designs such as cantilever type, multi-clamped membrane, and doubly-clamped beam type. In addition, laterally moveable switches have also been investigated, which showed better dynamic switching performance than that of vertical switches. An integration of MEM switch with conventional integrated circuit (IC) platforms was studied by Gretillat in 1997, which demonstrated the possibility of reducing the cost of mass production. To release commercialized MEM switches, much efforts mainly focused on the switches for the radio frequency (RF) applications, since the advantages (almost no leakage current, very small ON resistance) proved by the previous studies meet the requirements from the RF community [9]. During the period from the 1990s to 2000, large companies such as IBM, Motorola had intensively studied the MEM contact switch, however, due to the issues of packaging, commercialization [10, 11]. In the academic field, Prof. G. M. Rebeiz from University of California, San Diego (UCSD) and his group contributed two significant review papers of RF MEMS. Cantilever-type and server other types of metal-contact switches have been demonstrated by UCSD group, which showed high reliability under a nitrogen testing environment [12, 13]. However, no devices were produced to the market. The company named Omron from Japan achieved the first

successful products of RF MEM contact switch with decent packaging to increase the reliability, which showed outstanding performance. The Omron switch utilized wafer-to-wafer bonding for the SOI-based nanostructures to achieve a high isolation, and it was well designed with large metal hard contact, no dielectric layer to avoid the contact issues and dielectric charging [14, 15]. Another attempt on the hybridization of silicon CMOS and MEMS techniques was investigated by the researchers in EPFL [16]. A suspended-gate MOSFET was fabricated and characterized, which showed abrupt switching with a very small SS as 2.16 mV/dec (Figure 1.6). The image taken from Scanning Electron Microscope (SEM) was also displayed in Figure 1.6.

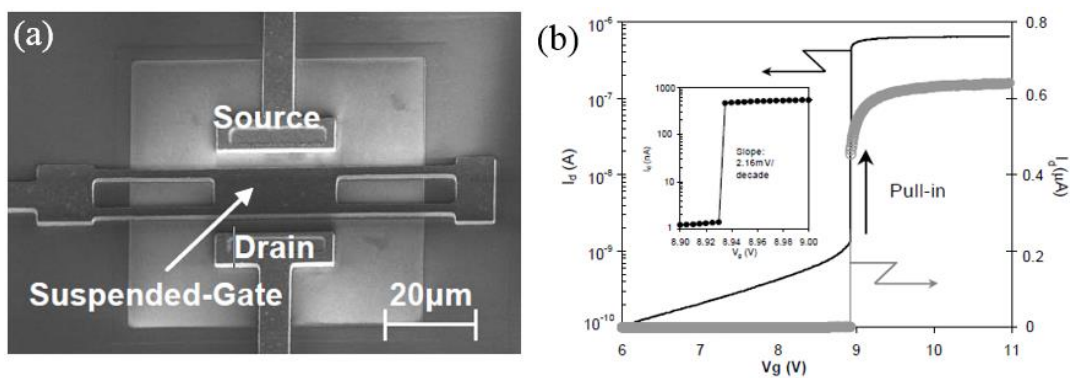


Figure 1.6 (a) SEM image of the fabricated suspended-gate MOSFET. (b) Switching characterization of the suspended-gate MOSFET [16].

1.3.2 NEMS AND NEMS SWITCHES

Nanoelectromechanical system (NEMS) is based on the heavily developed MEMS by further scaling the system down from micro-scale into nano-scale. The biggest motivation of researching the NEM devices is the almost zero power consumption at the OFF status. As known, conventional CMOS devices are facing with the bottleneck as an increase of standby power consumption when the sizes of the devices decrease.

NEM contact switches utilize electrostatic forces to deflect the moveable element mechanically, further forming a physical contact with the actuation electrode by applying the voltage between these elements, resulting in the conversion of status.

Thanks to the extremely low leakage current, NEM switches possess the huge advantages as reduced consumed power and increased ON/OFF ratio. Besides, the switching time of NEM switch is in the range of sub-microsecond, predicting from the analytical theory. NEM switches also have potential capability of working under the harsh environment like high radiation, external electric field and temperature, The

NEM switches have been widely explored for the several applications like a relay, a logic device, transistor and sensor, which is consistent with these switches based on the conventional semiconductor technology. However, currently, almost all the NEM contact switches were fabricated in the laboratory. It is still immature for the mass production on the wafer scale. Furthermore, the low reliability of the device performance mainly due to the adhesive forces at the contact limits the development of NEM contact switches.

Currently, most of the NEM switches were fabricated based on the conventional Si-based fabrication methods, using lithography to pattern the structure and then etching or depositing the desired materials to achieve the grounded structure. Finally, the grounded device will be immersed in the strong acid to release the movable elements like cantilevers and doubly-clamped beam. However, instead of using the top-down fabrication process, NEM switches fabricate by the bottom-up process were applied to fully utilize nanotubes and nanowires for building the nanostructures.

In this section, varieties of NEM switches actuated by electrostatic force are reviewed and discussed. These NEM switches are classified into four individual groups, referring from the material of moveable element. There is a silicon on insulator (SOI) based NEM switches, nanowire-based NEM switches, carbon nanotube (CNT) based NEM switches, graphene-based NEM switches.

- **Nanowire**-based NEM switches: Recently, a three-terminal NEM switching FET was successfully demonstrated by doubly clamped nanowire in experiments from the group in UCSD (Figure 1.7) [17]. Clear pull-in/pull-out operations were observed. Moreover, up to 130 switching cycles were measured, indicating the enhanced reliability due to three-terminal settings where the gate did not physically and electrically contact with the doubly-clamped nanowire thus largely reduced the contact issues such as creep and wear.

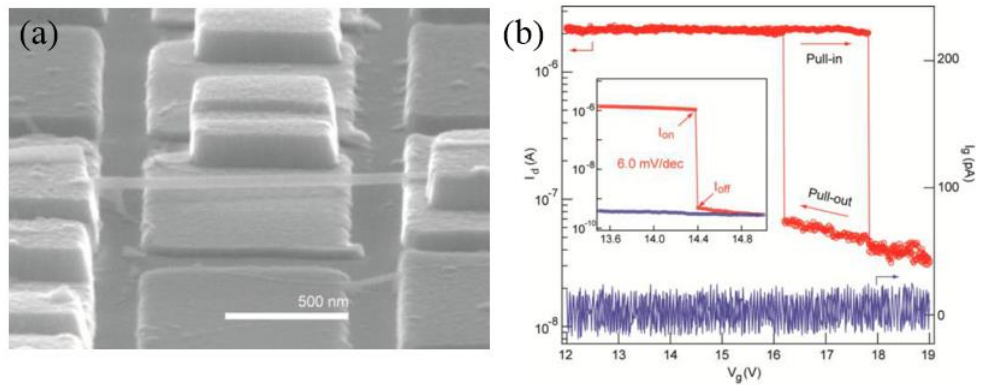


Figure 1.7 (a) SEM image of the fabricated nanowire-based switching FET. (b) Switching characterization of the nanowire-based switching FET [17].

- Carbon Nanotube** based NEM switches: A single-wall CNT was discovered by Prof. Iijima in 1991, which is a decade earlier than the observation of intrinsic monolayer graphene [18]. Interestingly, single-wall CNT can be considered as rolled-up graphene. Due to outstanding electrical properties (i.e., high conductivity) and mechanical properties (i.e., large Young's modulus), CNTs were applied for the NEM switches from the beginning of this century and became one of the promising materials for NEMS applications. In 2004, a three-terminal CNT NEM switch was demonstrated by the groups in Sweden [19]. Multiwall CNT was utilized as the cantilever-type nanostructure, and the CNT was deflected to contact with drain electrode by applying gate voltage. Switching hysteresis was observed experimentally from this device. Three years later, to adapt with existing CMOS technology, vertically aligned CNT-based capacitive switches were reported in Nature nanotechnology, showing the feasibility of large area fabrication of devices [20]. Horizontally aligned CNT switches were fabricated by the researchers from Switzerland (Figure 1.8) [21]. Low actuation voltage of 6 V was achieved. Owing to the high elastic stiffness of CNT and low mass, CNT-based switches showed improved performance at the frequency of gigahertz, which indicating the potential applications in the field of RF communications.

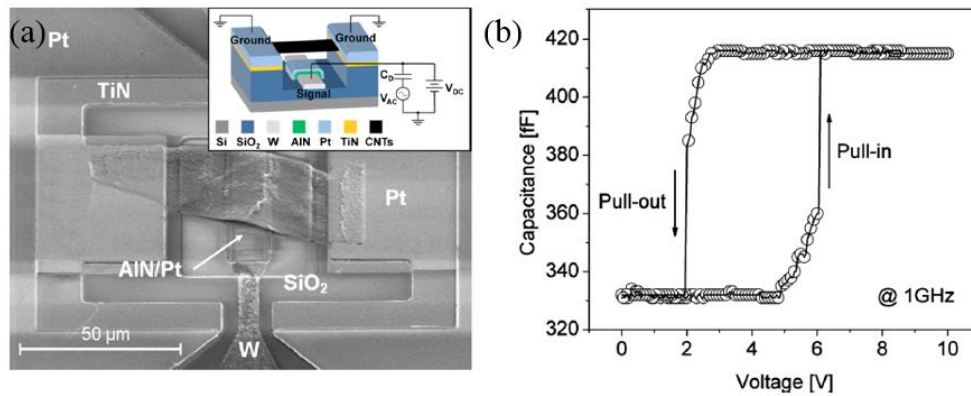


Figure 1.8 (a) SEM image of the fabricated CNT-based capacitive NEM switch. (b) C-V characterization of the CNT-based capacitive NEM switch [21].

- Graphene-based NEM switches:** Graphene is regarded as the material to improve the performance of NEM switches due to its better electrical (extremely high mobility) and mechanical properties (low mass, 1 TPa Young's modulus). In addition, due to its hydrophobic characteristics and weak interactions between the layers, graphene-based NEM was expected to solve the stiction problem and the reliability issues. Researchers from Massachusetts Institute of Technology (MIT) firstly reported the graphene-based NEM switches on 2009 [22]. They used polycrystalline graphene grown by the chemical vapor deposition (CVD) to define the moveable beam and bottom contact electrode. Graphene beam was broken after several cycles of operation. Two years later, a graphene NEM switch with very low pull-in voltage (1.85 V) was demonstrated by S. M. Kim and his colleagues, and their device fabrication showed the compatibility with the conventional CMOS technology [23]. Based on the quantitative study of exfoliated graphene-based NEM switches by Zhang's group, they found that monolayer graphene was not ideal for the NEM application since it was too easy to tear. Multilayer graphene-based NEM switch worked with a point contact with the probe of Scanning Tunneling Microscope (STM), which reached high reliability among the graphene NEM switching devices (~500 cycles). Instead of doubly clamped structure, cantilever-type graphene NEM switches were also measured using both two-terminal and three-terminal measurement by P. Li and his colleagues [24]. However, the reliability was still a severe issue of device performance. To overcome the adhesive forces, fully edge-clamped graphene membrane was intentionally designed to increase

the restoring force and to avoid the tear of graphene. Besides, in order to reduce the adhesive forces, line contact was applied to minimize the contact. Up to 30 cycles were achieved from this design [25]. To achieve large-scale fabrication of graphene NEM switches, CVD graphene was widely attempted, however, due to the grain boundaries in the graphene, the degradation of both electrical and mechanical properties of graphene occurred, which resulted in the problem of device reliability. Single-crystalline graphene-based NEM nano-scaled switches were fabricated, showing the lifetime of over 5000 switching cycles and low actuation voltage [26-27]. Recently, in Mizuta Lab, a bilayer graphene-based NEM switch with local bottom electrode was achieved with very low pull-in voltage, 1.8 V [28]. More importantly, the Au-C chemical bonding was firstly identified as the reason behind the stiction failure of the NEM switch. The Figure 1.9(a) of the fabricated graphene NEM switch from atomic-force microscopy (AFM) and the electrical characterization are shown below.

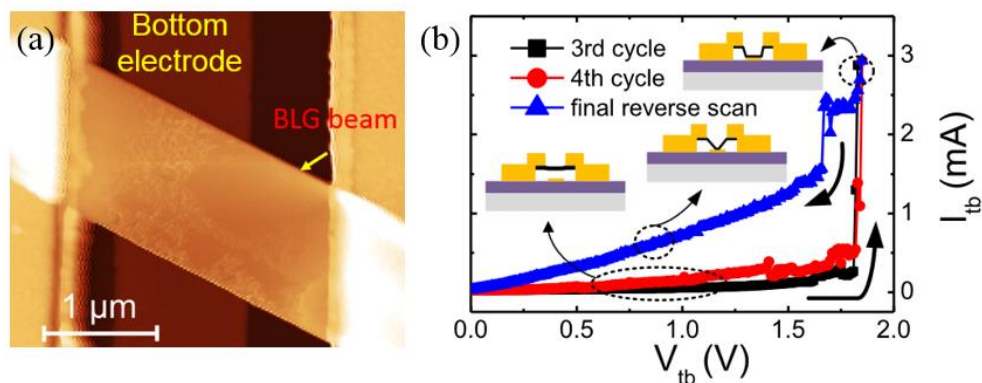


Figure 1.9 (a) AFM image of the fabricated bilayer graphene NEM switch. (b) Switching characterization of the bilayer graphene NEM switching device with a local bottom electrode [28].

- **Other 2D materials**-based switches: Molybdenum disulfide (MoS_2) as another two-dimensional material has also been an attempt for the application of NEM contact switch by T. Cui and his colleagues [29]. The actuation voltage was less than 10 V, which was much lower than conventional NEM switches. Furthermore, comparing with MoS_2 and graphene, the adhesive energy measured from MoS_2 is smaller than that of graphene. However, their MoS_2 -based switch only operated with only few cycles.

1.3.3 NON-VOLATILE LOGIC

Non-volatile logic, which is a new concept in the field of large-scale integration (LSI), is applied for the architecture design of the modern logic circuit. In general, there are two types of logic, which are the volatile type and non-volatile type. Regarding volatile logic, the circuit needs to supply the power from the extrinsic power source to maintain the bit state. By contrast, the information in non-volatile logic can be stored without continuously supplying the voltage. Currently, non-volatile logic is mainly used for the application of flash memory due to the large demands of high storage density and low power consumption. In addition, relatively low cost of non-volatile memory comparing with volatile type is another advantage of this technique. Moreover, by utilizing non-volatile logic, it has the possibility to overcome the bottleneck of von Neumann computing system, which is the limitation of time costing on data transfer, since the data storage and processing can be performed simultaneously under the non-volatile logic. New architecture design of non-volatile logic circuits, which could achieve bi-functions as data processing and memory, has attracted more and more attention from the community. Non-volatile switch, as a basic cell to build the logic circuit, has two fundamental requirements, which are nonvolatility and at least two stable switchable states. Floating-gate flash memory, as a conventional non-volatile memory, faces the limitation during the miniaturization. Several different approaches such as magnetic memory and ferroelectric memory were investigated. Thanks to the nano-scale sizes and fast switching time, utilizing NEMS technique, as one of the candidates to achieve non-volatile memory cell, can also achieve a bi-stable mechanical switch (Figure 1.10) [30]. Graphene, which is a promising material in terms of both mechanical and electrical properties, will also be a suitable material for fabricating the non-volatile memory.

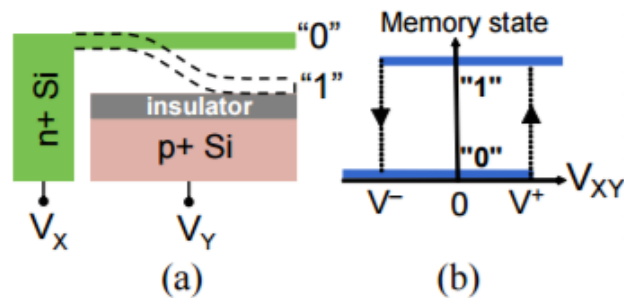


Figure 1.10 Mechanism of a NEM memory cell [30].

1.4 MOTIVATION AND CONTRIBUTION

Based on current research, NEM switch becomes as one of the promising candidates to overcome the limitations of conventional CMOS technology, which can offer extremely low leakage current, abrupt switching ($SS < 3 \text{ mV/dec}$) and high ON/OFF ratio. Thanks to the electrical and mechanical advantages of graphene, which are atomic thin and high carrier mobility, we can further scale down the size of NEM switches and reduce the pull-in voltage. Besides, as the era of Internet of things (IOT) is coming, Prof. Hiroshi Mizuta has proposed an complex, but comprehensive GNEMS sensor system (Figure 1.11) [31]. We can apply the graphene NEM switch to a power gating switch to cut the power supply when the sensor is in sleeping mode, thus effectively reducing the total energy dissipation. However, the critical point, hindering the development of graphene NEM switches, is the contact reliability. The irreversible stiction was often observed as the most common failure mode of GNEM switches. The chemical bond between Au and carbon was observed, which should be avoided from the design of GNEM switches [2].

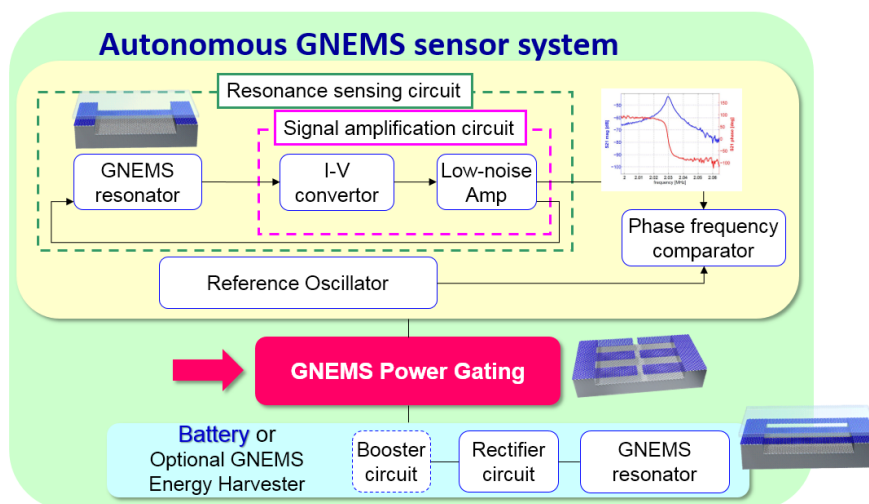


Figure 1.11 The autonomous GNEMS sensor system proposed by Prof. Hiroshi Mizuta [31].

In this study, the aim is to achieve stable switching operations of graphene NEM switches. Instead of the contact between graphene to metal, I chose natural oxide as the contact material with graphene to avoid the irreversible stiction. Static contact between graphene and Cr and also dynamic contact between graphene to Cr_2O_3 were studied in

detail by our novel graphene contact devices. The deformation type at the contact interface was investigated, offering an insight of graphene dynamic contact. Moreover, a bi-stable NEM switch was realized experimentally, which can work as a non-volatile memory cell to overcome the von Neumann bottleneck.

1.5 THESIS STRUCTURE

This dissertation is organized into six chapters. The content of these chapters is as follows:

- Chapter 2: **Related Theory.** In this chapter, several theories, which are related to my study of graphene NEM switching device, are introduced in sequence. The electromechanical analysis is firstly explained in detail, following with the introduction of short-range forces. After that, the graphene contact theories, which include both static contact and dynamic contact, are explained. Finally, the polarization and charging effect of the dielectric material is discussed.
- Chapter 3: **Fabrication of graphene NEM switching devices.** In this chapter, the detailed fabrication processes of my graphene NEM switches are explained. I start from the fabrication of graphene NEM switch with a local bottom electrode by pre-defining trenches. Then, the fabrication method of switches with a local top actuation electrode is discussed. Moreover, my graphene contact device, which combines transmission line method (TLM) pattern and high-resolution periodic pattern with the top-gated NEM switch, is introduced from a fabrication point of view.
- Chapter 4: **Study of contacts for graphene NEM switches.** In this chapter, the graphene NEM switches with local bottom gate, and contact devices are characterized to investigate the static and dynamic contact between the graphene and actuation electrode. With the help of a simulation of finite element method (FEM) and comparison with contact models, the contact issues are further discussed.
- Chapter 5: **Characterization of graphene NEM switching devices.** In this chapter, the fabricated graphene NEM switches with local top gates are characterized. A Periodic pillar structure is introduced into the contact interface.

Bi-stable switching behavior is observed and discussed, which is interpreted as a graphene NEM non-volatile memory cell.

- Chapter 6: **Summary and future work:** In this chapter, my study about graphene NEM switching devices is briefly concluded. The future work based on current conclusion is listed.

1.6 REFERENCES

- [1] G. E. Moore, "Cramming more components onto integrated circuits, Reprinted from Electronics, volume 38, number 8, April 19, 1965, pp.114 ff.," *IEEE Solid-State Circuits Soc. Newsl.*, vol. 11, no. 5, pp. 33–35, Sep. 2006.
- [2] W. Haensch *et al.*, "Silicon CMOS devices beyond scaling," *IBM J. Res. Dev.*, vol. 50, no. 4.5, pp. 339–361, Jul. 2006.
- [3] K. S. Novoselov *et al.*, "Electric Field Effect in Atomically Thin Carbon Films," *Science*, vol. 306, no. 5696, pp. 666–669, Oct. 2004.
- [4] A. K. Geim and K. S. Novoselov, "The rise of graphene," *Nat. Mater.*, vol. 6, no. 3, pp. 183–191, Mar. 2007.
- [5] K. I. Bolotin *et al.*, "Ultrahigh electron mobility in suspended graphene," *Solid State Commun.*, vol. 146, no. 9–10, pp. 351–355, Jun. 2008.
- [6] "Contact resistivity and current flow path at metal/graphene contact," *Appl. Phys. Lett.*, vol. 97, no. 14, p. 143514, Oct. 2010.
- [7] C. Lee, X. Wei, J. W. Kysar, and J. Hone, "Measurement of the Elastic Properties and Intrinsic Strength of Monolayer Graphene," *Science*, vol. 321, no. 5887, pp. 385–388, Jul. 2008.
- [8] "Wiley: MEMS and Microsystems: Design, Manufacture, and Nanoscale Engineering, 2nd Edition - Tai-Ran Hsu." [Online]. Available: <http://www.wiley.com/WileyCDA/WileyTitle/productCd-0470083018.html>. [Accessed: 13-Feb-2017].
- [9] G. M. Rebeiz, C. D. Patel, S. K. Han, C. H. Ko, and K. M. J. Ho, "The Search for a Reliable MEMS Switch," *IEEE Microw. Mag.*, vol. 14, no. 1, pp. 57–67, Jan. 2013.
- [10] R. E. Mihailovich *et al.*, "MEM relay for reconfigurable RF circuits," *IEEE Microw. Wirel. Compon. Lett.*, vol. 11, no. 2, pp. 53–55, Feb. 2001.
- [11] A. P. D. Silva *et al.*, "Motorola MEMS switch technology for high frequency applications," in *2001 Microelectromechanical Systems Conference (Cat. No. 01EX521)*, 2001, pp. 22–24.
- [12] G. M. Rebeiz, G.-L. Tan, and J. S. Hayden, "RF MEMS phase shifters: design and applications," *IEEE Microw. Mag.*, vol. 3, no. 2, pp. 72–81, Jun. 2002.

- [13] G. M. Rebeiz and J. B. Muldavin, "RF MEMS switches and switch circuits," *IEEE Microw. Mag.*, vol. 2, no. 4, pp. 59–71, Dec. 2001.
- [14] Y. Uno *et al.*, "Development of SPDT-structured RF MEMS switch," in *TRANSDUCERS 2009 - 2009 International Solid-State Sensors, Actuators and Microsystems Conference*, 2009, pp. 541–544.
- [15] T. Seki *et al.*, "Development of a large-force low-loss metal-contact RF MEMS switch," *Sens. Actuators Phys.*, vol. 132, no. 2, pp. 683–688, Nov. 2006.
- [16] "Suspended-gate MOSFET: bringing new MEMS functionality into solid-state MOS transistor - IEEE Xplore Document." [Online]. Available: <http://ieeexplore.ieee.org/document/1609384/>. [Accessed: 13-Feb-2017].
- [17] J.-H. Kim, Z. C. Y. Chen, S. Kwon, and J. Xiang, "Three-Terminal Nanoelectromechanical Field Effect Transistor with Abrupt Subthreshold Slope," *Nano Lett.*, vol. 14, no. 3, pp. 1687–1691, Mar. 2014.
- [18] S. Iijima and T. Ichihashi, "Single-shell carbon nanotubes of 1-nm diameter," *Nature*, vol. 363, no. 6430, pp. 603–605, Jun. 1993.
- [19] S. W. Lee *et al.*, "A Three-Terminal Carbon Nanorelay," *Nano Lett.*, vol. 4, no. 10, pp. 2027–2030, Oct. 2004.
- [20] J. E. Jang *et al.*, "Nanoscale memory cell based on a nanoelectromechanical switched capacitor," *Nat. Nanotechnol.*, vol. 3, no. 1, pp. 26–30, Jan. 2008.
- [21] D. Acquaviva *et al.*, "Capacitive nanoelectromechanical switch based on suspended carbon nanotube array," *Appl. Phys. Lett.*, vol. 97, no. 23, p. 233508, Dec. 2010.
- [22] Kaveh M. Milaninia *et al.*, "All graphene electromechanical switch fabricated by chemical vapor deposition," *Appl. Phys. Lett.*, vol. 95, no. 18, p. 183105, Nov. 2009.
- [23] Sung Min Kim *et al.*, "Suspended few-layer graphene beam electromechanical switch with abrupt on-off characteristics and minimal leakage current," *Appl. Phys. Lett.*, vol. 99, no. 2, p. 023103, Jul. 2011.
- [24] Peng Li *et al.*, "Graphene cantilever beams for nano switches," *Appl. Phys. Lett.*, vol. 101, no. 9, p. 093111, Aug. 2012.
- [25] X. Liu *et al.*, "Large Arrays and Properties of 3-Terminal Graphene Nanoelectromechanical Switches," *Adv. Mater.*, vol. 26, no. 10, pp. 1571–1576, Mar. 2014.

- [26] P. Li and T. Cui, "Single-crystalline graphene radio-frequency nanoswitches," *J. Micromechanics Microengineering*, vol. 25, no. 7, p. 075022, 2015.
- [27] P. Li *et al.*, "Single-crystalline monolayer and multilayer graphene nano switches," *Appl. Phys. Lett.*, vol. 104, no. 11, p. 113110, Mar. 2014.
- [28] J. Sun *et al.*, "Low pull-in voltage graphene electromechanical switch fabricated with a polymer sacrificial spacer," *Appl. Phys. Lett.*, vol. 105, no. 3, p. 033103, Jul. 2014.
- [29] P. Li, Z. You, and T. Cui, "Molybdenum disulfide dc contact MEMS shunt switch," *J. Micromechanics Microengineering*, vol. 23, no. 4, p. 045026, 2013.
- [30] K. Akarvardar and H.-S. P. Wong, "Nanoelectromechanical Logic and Memory Devices," *ECS Trans.*, vol. 19, no. 1, pp. 49–59, May 2009.
- [31] H. Mizuta, Grant-in-aid for Scientific Research 25220904 from JSPS, 2013-2018.

2 Related Theory

In this chapter, the basic physics and related equations behind the switching operations of MEMS/NEMS contact switches are introduced. Pull-in and pull-out of the movable element, as the fundamental operations of NEM contact switches, are explained at first. By using these equations, it is useful for designing the geometry structures of devices. Then, reliability issues of graphene NEM switching device, which is the most critical point of its development, are discussed from three different views which are static friction, graphene contact, and dielectric charging.

2.1 ELECTROMECHANICAL ANALYSIS

2.1.1 PULL-IN ANALYSIS

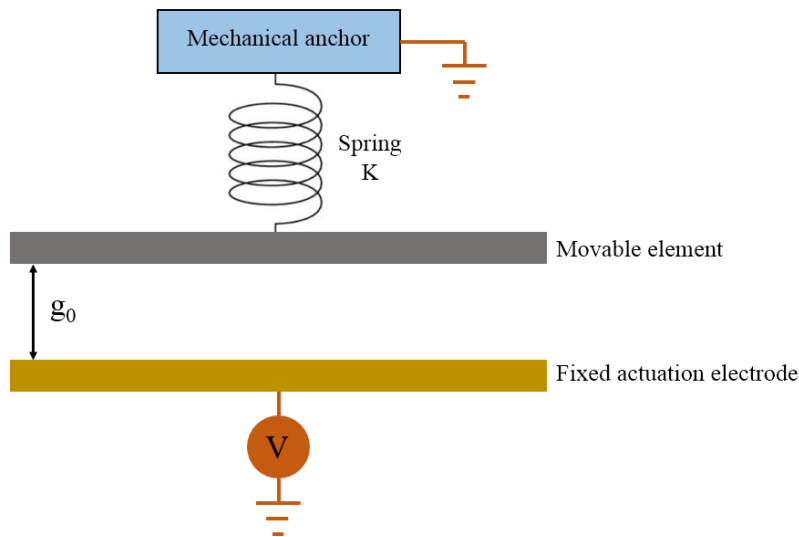


Figure 2.1 1D parallel plate model to calculate the voltage of pull-in effect

Figure 2.1 shows a typical one-dimensional (1D) parallel-plate model. One plate is fixed and controlled by a voltage source, which is normally considered as the fixed actuation electrode. The other plate, which is regarded as a movable element, is connected to the ground electrically. When applying the voltage on the fixed actuation electrode, electrostatic force generates owing to the potential difference, which attracts

the movable element approaching the actuation electrode. The electrostatic force related to the geometry of two plates and the applied voltage is express as below [1]:

$$F_{\text{electrostatic}} = \frac{\epsilon_0 W L V^2}{2g_0^2} \quad (2.1)$$

where ϵ_0 is the vacuum permittivity, L and W are the length and width of its geometrical shape, V is the applied voltage of the actuation electrode, and g_0 is air gap distance between the movable element and fixed electrode. The mechanical motion of a movable element modelled as a linear spring following the Hooke's law, which acts as restoring force. The spring constant is determined by the geometry of the movable elements. The equation indicating a linear response of restoring mechanical motion of the movable element is shown below.

$$F_{\text{restoring}} = Kd \quad (2.2)$$

where K is the spring constant of the movable element, and d is the distance moved from anchored electrode from its original position. For NEM contact switch study, double-clamped beam and single-clamped cantilever structure are often investigated. Spring constants of double-clamped beam and cantilever are expressed as [2, 3]:

$$K_{\text{double-clamped beam}} = \frac{32EWt^3}{L^3} \quad (2.3)$$

$$K_{\text{cantilever}} = \frac{EWt^3}{4L^3} \quad (2.4)$$

where E is Young's modulus of material used for the movable element, L and W are the length and width of its structure, respectively, and t is the thickness of beam or cantilever. The electromechanical system is mainly governed by the mechanical restoring force and electrostatic force. As the voltage applied to the actuation electrode, the movable element is approaching to the fixed electrode at the beginning, since those two forces mentioned above are under equilibrium state. However, at a certain position (usually two-thirds of original gap distance), the electrostatic force overwhelms the mechanical restoring force, resulting in a sudden collapse of movable element on the electrode and a sharp increase of current. The phenomenon mentioned above is called pull-in effect, and we can calculate the pull-in voltage from the estimated electrostatic and restoring force at the position of two-thirds of original gap. The pull-in equation is shown below:

$$V_{\text{pull-in}} = \sqrt{\frac{8Kg_0^3}{27\epsilon_0 WL}} \quad (2.5)$$

If we considered the spring constant of double-clamped beam and cantilever into the estimation of pull-in voltage, the equations of pull-in voltage could be rewritten as:

$$\text{Double-clamped beam: } V_{\text{pull-in}} = \sqrt{\frac{256Et^3g_0^3}{27\varepsilon_0L^4}} \quad (2.6)$$

$$\text{Cantilever: } V_{\text{pull-in}} = \sqrt{\frac{16Et^3g_0^3}{81\varepsilon_0L^4}} \quad (2.7)$$

2.1.2 PULL-OUT ANALYSIS

For the pull-out operation, the assumed initial position of both plates is in contact, which is shown in Figure 2.2. By applying the voltage, electrostatic force is generated, while the mechanical restoring force reaches to the highest value because of the maximum distance moved from anchored electrode from its original position. With the decrease of voltage applied between movable element and actuation electrode, the electrostatic force is reducing. Once the mechanically-restoring force overcomes the attraction force, the movable element will be detached from the actuation electrode, which is called as pull-out.

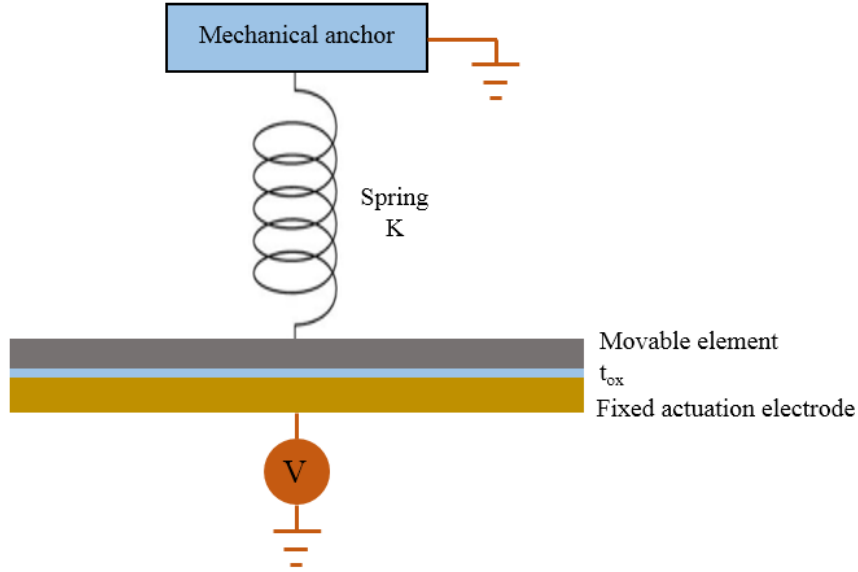


Figure 2.2 1D parallel plate model to calculate the voltage of pull-out effect

Owing to the existence of dielectric oxide layer at the contact interface, the polarized dielectric layer governs the electrostatic force. Assuming the dielectric layer having the thickness of t_{ox} , the pull-out voltage can be described by the equation below.

$$V_{\text{pull-out}} = \sqrt{\frac{2Kt_{ox}^2}{\varepsilon_{ox}\varepsilon_0WL}} (g_0 - t_{ox}) \quad (2.8)$$

where ε_{ox} is the relative permittivity of the dielectric oxide, and we can also applied this equation with the spring constants of double-clamped beam and cantilever, then the modified equations are listed below.

$$\text{Double-clamped beam: } V_{\text{pull-in}} = \sqrt{\frac{256Et^2g_0^3}{27\varepsilon_{ox}\varepsilon_0L^4}}(g_0 - t_{ox}) \quad (2.9)$$

$$\text{Cantilever: } V_{\text{pull-in}} = \sqrt{\frac{16Et^2g_0^3}{81\varepsilon_{ox}\varepsilon_0L^4}}(g_0 - t_{ox}) \quad (2.10)$$

The analytical equations describing the pull-in and pull-out voltage rely on ideal conditions such as material properties and precise geometry. In other words, these analytical models can be used for estimating or examining the proposed structures. There are always some gaps between estimated values and experimental results, since several physical factors, such as short range forces, dielectric charging effect, are not included in these models, which will be explained in next sections [4-5].

2.2 THE SHORT RANGE FORCES

The short ranges forces in the study of MEMS/NEMS contact switches are mainly van der Waals (vdW) force and Casimir force, which perform as adhesive forces hindering the movable element away from the actuation electrode. In general, induced dipole moment occurs on all molecules or atoms owing to the non-uniform distribution of positive and negative charges, resulting in the interatomic forces between atoms or molecules [6]. VdW force can be considered as a sum of interatomic forces. Although the vdW force is weaker than bonding forces like covalent bonds, this van der Waals interaction mainly dominates at the separation distance lower than 10 nm [7]. Figure 2.3 display the relationship between the separation distance of atoms and van der Waals interaction from two approximations. Positive pressure indicates repulsive force, and negative pressure shows interaction. The separation distance between 0.4 nm to 0.6 nm, which is close to the separation distance between two carbon atoms in graphene, gives relative high attractive force. Comparing with van der Waals force, Casimir force plays a dominant role at a relative longer range which is over 100 nm.

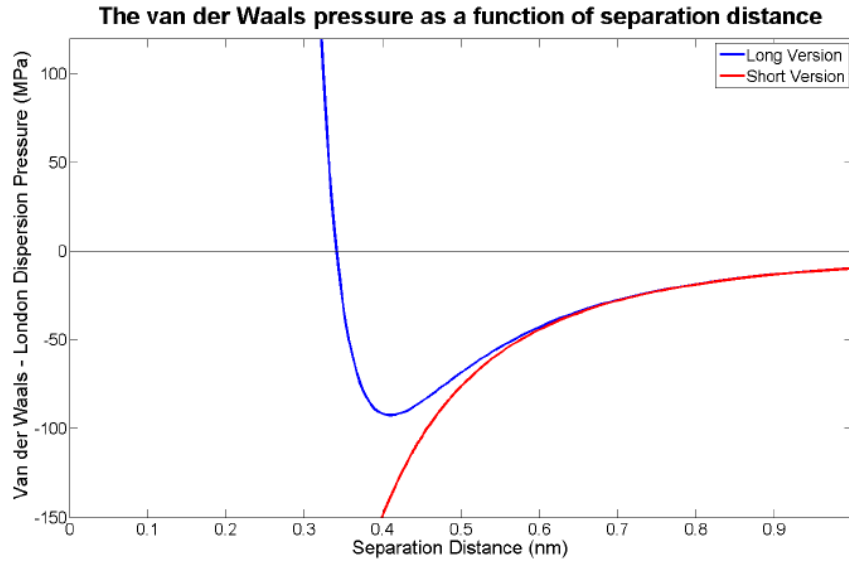


Figure 2.3 Difference between two van der Waals force approximation at the very short range [8].

As scaling down the size of contact switch from micro-scale to nano-scale, especially for NEMS contact devices, the vdW force plays a more important role than Casimir force when the movable element and actuation electrode are in contact. Besides, the surface roughness of evaporated metal is only around several nm. Thus, vdW force as one of the primary sources of adhesive force has to be considered. Novel saw tooth shaped actuation electrode is designed and fabricated aiming to control and minimize the short range forces [9]. In addition, physical adsorption of gas molecules on the surface of graphene also originates from the van der Waals interaction.

2.3 CONTACT STUDY

The common failure mode of graphene NEM switch is the irreversible static friction between the movable graphene and the fixed contact electrode. The total contact resistance of graphene contact switches consists of the static contact resistance at the clamping contact electrode and the dynamic contact resistance between the movable graphene and the actuation electrode. Thus, detailed studies of graphene-metal contacts, especially for the dynamic contact, can understand the stiction between the graphene and the anchored metal contact and to realize reversible NEM switch operation.

2.3.1 STATIC CONTACT OF GRAPHENE

The study of contact resistance between graphene and contact metals is widely conducted [10-15]. As reported, graphene devices on standard SiO₂ substrates are highly disordered, and the carrier mobility in graphene reduces due to the scattering from impurities or charged surface states. Besides, the surface roughness of substrate and optical phonons on the surface are another two factors limiting the graphene characteristics comparing with intrinsic properties [17,18]. Theoretically, to obtain a low contact resistivity, a large difference of work function between metal and graphene is preferred. The reason is that the density of states (DOS) in graphene under the metal contact considerably increases. Thus the electrons can be transferred from metal to graphene swiftly. Experimentally, the measured results show that the work function of graphene under metal is quite different with the work function of graphene only. The work functions of graphene under Ni or Cr are similar to that of Ni or Cr, respectively. However, almost the same work function is observed from the graphene-Au and graphene-Pd contact. The low work function of graphene under the metal contact is considered as an obvious trend for the high contact resistance. Besides, there are several related factors listed below, which affect the static contact resistance.

- **Wettability:** Wettability of the contact surface becomes a very important argument when discussing the metal to semiconductor contact. Making the contact surface hydrophilic is one of the scenarios to improve the contact. Palladium, which has high wettability and the intermediate work function of 4.6eV after contact, forms the best contact with graphene comparing with that of Cr [11].
- **Layer Number of graphene:** The layer number of graphene is almost independent of the contact resistance (R_c), and only the top one or two layers of graphene play the most important role in the formation of graphene and metal contact [10, 13].
- **Channel width:** The key parameter of the contact resistivity is the channel width rather than the contact area, which is illustrated by Fig. 2.4 [15].

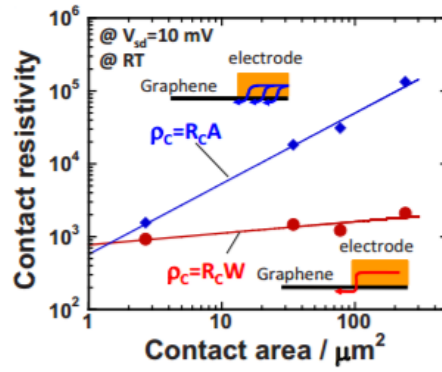


Figure 2.4 Channel width type and area type of contact resistivity [15].

- **Sheet resistance:** The sheet resistance of graphene is independent of the R_c . When the graphene channel is under high bias voltage from the back gate silicon, the total resistance is dominated by the contact resistance of the R_c [10, 12].
- **Annealing:** Post-annealing removing the contamination at the interface has a strong effect on reducing the contact resistance. Ambient will introduce p-doped into graphene due to the absorbed water molecules [10, 12, 14].
- **Metal deposition quality and methods:** By observing SEM images of the deposited metal surface, metal films like Pd, Ni, Co, which have small grains, has better contact performance than that of Ag, Fe, Cr. This is because that small grains in metal directly enhance the contact area with graphene layer [10]. Comparing with two metal deposition methods which are electron beam (e-beam) evaporation and sputter, larger amounts of defects and carbon vacancies are observed on sputtered sample than that of evaporated sample by analyzing the Raman spectra data. This is due to that sputtered metal atoms possess larger kinetic energy compared to evaporation method. Regarding the contact resistance, sputtered metal contacting with mono/bilayer graphene show high contact resistance with the samples using evaporated metal [16]. Depositing metal under a high vacuum level has a significant influence on the reducing the contact resistance [17].

Regarding measuring the static contact resistance, transmission line method (TLM) is a frequently applied method to extract the contact resistance (R_c) between a metal and a semiconductor. As shown in Fig. 2.5, a typical TLM structure has several metal contacts (normally 5-7 contacts) with different interspacing distance. The contact

area of each electrode should be kept as the same size.

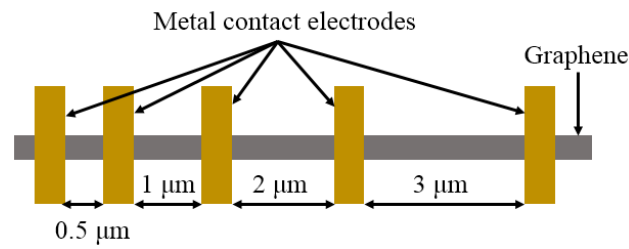


Figure 2.5 A typical TLM pattern to extract the contact resistance

For the TLM measurement, the total resistance (R_{total}) between two neighboring contact electrodes is including the graphene channel resistance (R_G) and static contact resistance (R_C) at graphene to metal contacts [15]. The relationship between R_{total} and R_C is shown by

$$R_{total} = R_G + 2R_C = \frac{\rho_G}{W}L + 2R_C . \quad (2.11)$$

where L and W are the length and width of the GNR channel, respectively, and ρ_G is the sheet resistance of graphene. Sheet resistance is a measure of the resistance of thin films which normally have a uniform thickness. Theoretically, the sheet resistance is the ratio of resistivity to the thickness of the thin film. The unit of sheet resistance is ohms per square (Ω/\square). By plotting the total resistance as a function of the interspacing distance between two neighbor contacts, we can extract the values of sheet resistance and contact resistance from the slope and the intercept in Y-axis, respectively. Finally, Table 2.1 displays A summary of experimental results of static graphene to metal contact resistance from literature is displayed in Table 2.1 [10-12,15].

Table 2-1 Summary of measured static graphene-metal contact resistance

Temperature	Pressure	Annealing	Materials	Channel Width	Results of contact resistance (From small to large)
RT	$\leq 10e-2$ Pa	300C 5 mins Ar+H2(3%)	Gr,Ti,Ag,Ni, Co,Cr,Fe,Pd	1 um	Co<Ni<Pd<Ti<Fe<Ag<Cr
RT	Ambient	Unknown	Gr,Cr,Ni,Pd, Au	10 um	Pd<Au<Ni<Cr
Unknown	Unknown	500-800C 30s, Ar	CNT,Pt,Pd,Ni,Au,Cu,Cr,Fe,Ti ,Nb,Al,Ag,Ga,Mn,Hf		Ti,Fe,Cr<Cu<Au<Pd,Ag<Nb,Pt <Ga<Mo<Hf
RT	Vaccum	300C 1h Ar+H2	Gr,Cr,Ni,Ti	Unknown	Ni<Cr,Ti

2.3.2 DYNAMIC CONTACT OF GRAPHENE

During NEMS contact switch fabrication, e-beam evaporation has been applied with a controlled low deposition rate to minimize the surface roughness. However, the surface roughness of deposited metal is still around several nanometers when examining the surface by the AFM. Thus, the contact resistance of movable element to metal electrode changes as the real contact area varies due to the change in electrostatic force, which is the origin of dynamic contact resistance in the study of contact switches. By monitoring the dynamic contact resistance of contact switches, type of electron transport and change in contact interface can be analyzed [19]. Electrical contact resistance, the same concept with dynamic contact resistance, has been widely applied as an in-situ tool to understand the behavior of MEMS contact switch [20,21]. Then, two types of contact deformation which are elastic and plastic deformation are introduced, which gives a simple prediction of contact resistance based on the contact theory [22].

- **Elastic deformation:** If the deformation is elastic, the deformed shape will return to its original shape once the applied forces retract. Assume a single asperity contact model, for elastic deformation, the contact area A is described as

$$A = \pi R \alpha \quad (2.12)$$

where R is asperity peak radius of curvature, and the vertical deformation is expressed by α . Then based on the contact area, the relationship between contact force F_{contact} and contact resistance R_{cDE} is shown below

$$R_{\text{cDE}} = \frac{\rho}{2} \left(\frac{4E'}{3RF_{\text{contact}}} \right)^{\frac{1}{3}} \quad (2.13)$$

where ρ is the resistivity of the conducting material, H is the Meyer hardness of the softer material. E' is the Hertzian modulus, which is related to Young's modulus (E) and Poisson's ratio (ν) of two contact materials.

$$\frac{1}{E'} = \frac{1-\nu_1^2}{E_1} + \frac{1-\nu_2^2}{E_2} \quad (2.14)$$

If combining equation 3.12 and 3.13, we can derive the effective contact radius (r) as

$$r = \left(\frac{3RF_{\text{contact}}}{4E'} \right)^{\frac{1}{3}} \quad (2.15)$$

To determine the elastic deformation from the measured contact resistance, the effective radius is a critical factor which should be analyzed.

- **Plastic deformation:** If the deformation is plastic, the deformed shape will not return to its original shape once the applied forces retract. The contact area expression changed owing to the irreversible deformation, and the relationship between contact resistance under plastic deformation (R_{cDP}) and contact force is shown below.

$$A = 2\pi R\alpha \quad (2.16)$$

$$R_{cDP} = \frac{\rho}{2} \left(\frac{H\pi}{F_{\text{contact}}} \right)^{\frac{1}{2}} \quad (2.17)$$

where H is the Meyer hardness of the softer material, and we also can derive effective contact radius listed below.

$$r = \left(\frac{F_{\text{contact}}}{H\pi} \right)^{\frac{1}{2}} \quad (2.18)$$

2.4 POLARIZATION/CHARGING OF DIELECTRIC

A net polarization of dielectric materials occurs when an external electric field is applied. Not only one, but five different types are in charge of the polarization, which is electronic, atomic, dipolar, intrinsic space charge and extrinsic spacing charge [23, 24]. The sum of these five types of polarization results in a net polarization of a dielectric.

- **Electronic Polarization**

Electrons which are bound to the atoms polarized when applying the external electric field. Electrons shift away from nuclei which possess positive charge. In this case, a temporary induced dipole can be assumed. This type of polarization occurs in every material, and also the speed of polarization is the fastest among those five types, which is around 10^{-15} second.

- **Atomic Polarization**

Comparing with electronic polarization, atomic polarization is based on the existence of permanent ionic dipoles, which is slightly slower for the response (10^{-14} - 10^{-12} seconds). Instead of shifting the electrons, the atoms move relatively once an external electric field is applied.

- **Dipolar Polarization**

Dipolar polarization, which is also called as molecular polarization, need permanent molecular dipoles. Without applying the voltage, these molecular dipoles are randomly distributed in the dielectric. Once the external field is generated, dipoles will be oriented, being parallel to the electric field.

- **Intrinsic and Extrinsic Spacing Charge Polarization**

Both intrinsic and extrinsic spacing charge polarization belong to the interfacial polarization, which describes the motion of free charges in/between heterogeneous materials. Polarization from intrinsic spacing charge origins from the relocation of the intrinsic charges inside of the dielectric under the electric field, which performs the opposite polarity with the electrodes. The source of extrinsic charges is usually from the contact electrodes, and charge carriers inject into the dielectrics. Polarization due to the extrinsic spacing charges shows the same sign of charges with the applied electrodes.

When discussing the dielectric effect, dipolar and interfacial polarization plays the major roles, since both of these two polarization are time-related [25]. The charging and relaxation time are from 10^{-12} seconds to years, and interfacial polarization is relatively slower than dipolar polarization [26].

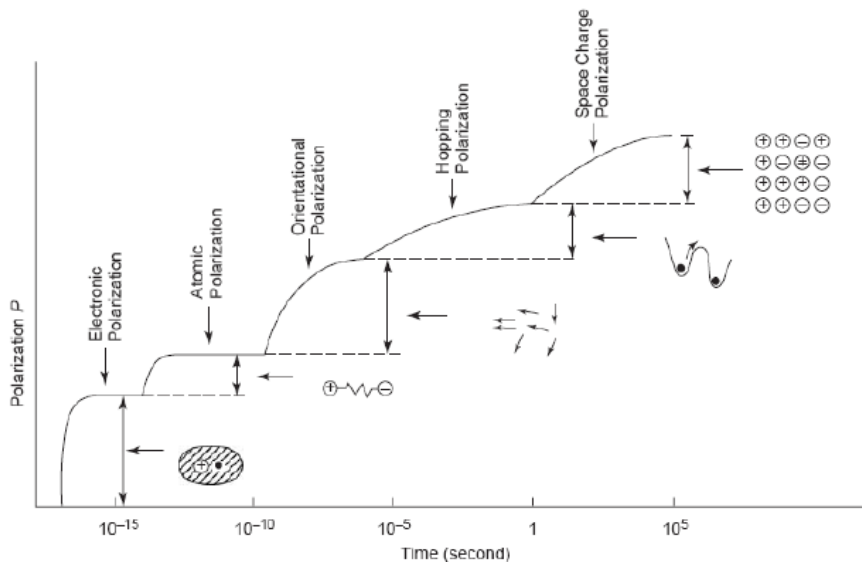


Figure 2.6 Relationship between time and different types of polarization [26]

The main challenge of NEMS contact switch is the irreversible adhesion between the movable element and actuation electrode. Since a thin oxide layer usually is applied on the contact interface to avoid the formation of bonding, the stiction of NEMS contact largely is due to the polarized dielectric layer. Once the voltage is applied to the

actuation electrode, randomly distributed dipoles in the dielectric get orientation. In addition, intrinsic and extrinsic spacing charge also plays an important role during the characterization of contact switch. Surface charges of the dielectric resulting from the polarization of molecular dipoles and intrinsic space charges show the opposite polarity, comparing with that of external electrodes. In contrast, polarization injected from the external charge carriers has the same polarity with the electrodes. It was reported that charge injection from either actuation electrode or moveable element resulted in irreversible stiction or variation of the pull-in voltage [27]. In terms of NEMS/MEMS contact switch, two different approaches of charging and polarization are conducted for the contactless state and contact state, which are illustrated in Figure 2.7 [28].

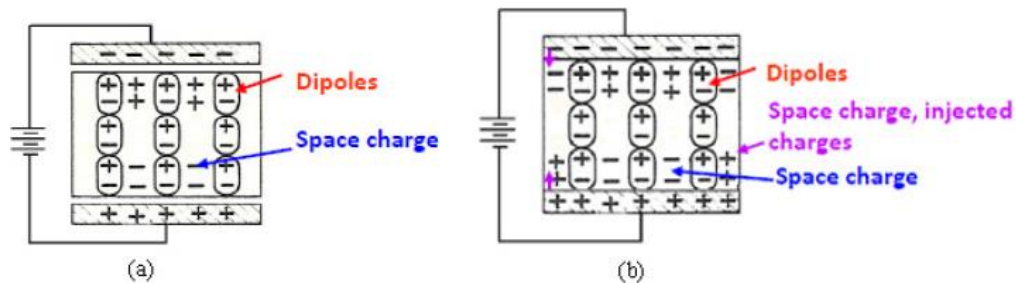


Figure 2.7 Two polarization and charging mechanism for the (a) contactless mode (b) contact mode of NEM/MEM switches [28]

When the NEM/MEM switch is under the non-contact mode with the dielectrics [Figure 2.7 (a)], the total polarization is considered as the sum of polarization from dipoles and polarization from intrinsic space charges, since both types of the polarization leading to the surface charges have the same polarity, which is opposite to the external electrodes. While the dielectric layer is contacted with external electrodes [Figure 2.7 (b)], additionally, polarization due to the external space charges is introduced and behaves like homo-charges. Charge injection and relaxation at the contact interface between the movable element and actuation electrode is more difficult than the other side because of the non-ideal contact. As reported, for the structure shown in Figure 2.8, charge injection from Al to SiO₂ had quicker charging time and slower discharging time, comparing with charge injection from metal electrode to the dielectrics [27]. Charging time is exponential to the applied voltage, and saturation of charging at the top contact is easier than that from metal-dielectric contact due to the difference in the real contact area.

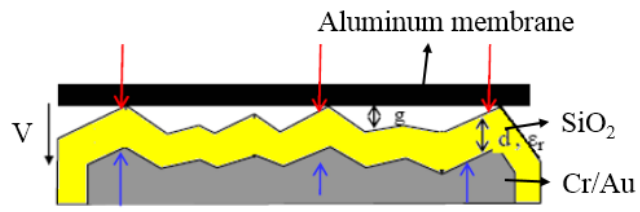


Figure 2.8 In contact state, charging and discharging occur from both directions.

2.5 REFERENCE

- [1] H. Kam and T.-J. King Liu. Pull-In and Release Voltage Design for Nano-electromechanical Field-Effect Transistors. *IEEE Transactions on Electron Devices*, 56(12), 2009.
- [2] S. Chakraborty, A. Bhattacharya, and T. K. Bhattacharyya. Experimental analysis of pull-out voltage of electrostatically actuated micro cantilever beam based on contact stiction model. *Micro & Nano Letters*, 6(1) 43-47, 2011.
- [3] K. Akarvardar, C. Eggimann, D. Tsamados, Y. S. Chauhan, A. M. Wan, G. C. and Ionescu, R. T. Howe, and H. S. Philip Wong. Analytical Modeling of the Suspended-Gate FET and Design Insights for Low-Power Logic *IEEE Transactions on Electron Devices*, 55(1), 2008.
- [4] G. Klimchitskaya, U. Mohideen, and V. Mostepanenko. Casimir and van der Waals forces between two plates or a sphere (lens) above a plate made of real metals. *Physical Review A*, 61(6), 2000.
- [5] R. K. Gupta, Electrostatic pull-in test structure design for in-situ mechanical property measurements of microelectromechanical systems (MEMS). PhD thesis, Massachusetts Institute of Technology, 1997.
- [6] R. H. S. Winterton. Van der Waals Forces. *Contemporary Physics*, 11(6) 559-574, 1970.
- [7] A. W. Rodriguez, F. Capasso, and S. G. Johnson. The Casimir effect in micro structured geometries. *Nature Photonics*, 5, 2011.
- [8] L. Boodhoo, Silicon-based non-volatile nano-electro-mechanical switch with controlled van der Waals force, PhD thesis, University of Southampton, 2015.
- [9] L. Boodhoo, F. Alkhalil, H. M. H. Chong, Y. Tsuchiya, W. Redman-White, T. Hasegawa, H. Mizuta, Novel Saw Tooth Gate for Stiction and Pull-in Voltage Controlled Ohmic Silicon NEMS Switch, the 41st Micro and Nano Engineering, 2015.
- [10] W. Eiichiro, et al., Low contact resistance metals for graphene based devices, *Diamond & Related Materials*, 2012.
- [11] M. S. Seung, et al., Determination of work function of graphene under a metal electrode and its role in contact resistance, *Nano Letters*, 2012.
- [12] C. L. Seong, et al., Contact resistance between metal and carbon nanotube

- interconnects: Effect of work function and wettability *Applied Physics Letters*, 2009.
- [13] A. Venugopal, et al., Contact resistance in few and multilayer graphene devices. *Applied Physics Letters*, 2010.
- [14] T. S. Joshua, et al., Reducing Contact Resistance in graphene devices through contact area patterning. *ACS NANO*, 2013.
- [15] K. Nagashio, et al., Contact resistivity and current flow path at metal/graphene contact, *Applied Physics Letters*, 2010.
- [16] L. Wenjun, et al., A study on graphene-metal contact, *Crystals*, 2013.
- [17] C. R. Dean, et al., Boron nitride substrates for high-quality graphene electronics, *Nature Nanotechnology*, 2010.
- [18] N. Kharche, et al., Quasiparticle band gap engineering of graphene and graphene on hexagonal boron nitride substrate, *Nano letters*, 2011.
- [19] G. Wexler, The size effect and the nonlocal Boltzmann transport equation in orifice and disk geometry, *Proc. Phys. Soc.* 89 927-941, 1966.
- [20] L. Kogut and K. Komvopolous, Electrical contact resistance theory for conductive rough surfaces, *Amer. Inst. Phys.*, 94 (5) 3153-3162, 2003.
- [21] L. Kogut et al., Electrical contact resistance theory for conductive rough surfaces separated by a thin insulating film, *Amer. Inst. Phys.*, 94 (2) 576-585, 2003.
- [22] S. Majumder et al., Study of contacts in an electrostatically actuated microswitch, *Sens. Act. A.*, 93 (1) 19-26, 2001.
- [23] A. V. Hippel, *Dielectric Materials and Applications*: John Wiley & Sons, 1954.
- [24] P. Harrop, *Dielectrics*: John Wiley & Sons, 1972.
- [25] C. J. F. Böttcher, *Theory of electric polarization*. Amsterdam: Elsevier, 1952.
- [26] K. C. Kao, *Dielectric Phenomena in Solids, With Emphasis on Physical Concepts of Electronic Processes*. Amsterdam: Elsevier, 2004.
- [27] Z. Peng, X. Yuan, J. C. M. Hwang, D. Forehand, and C. L. Goldsmith, "Top versus bottom charging of dielectric in RF MEMS capacitive switches," *Proc IEEE Asian Pacific Microwave Conference*, pp. 1535-1539, 2006.
- [28] N. Tavassolian, "Dielectric charging in capacitive RF MEMS switches with silicon nitride and silicon dioxide," PHD thesis, 2011.
- [29] C. L. Goldsmith, J. Ehmke, A. Malczewski, B. Pillans, S. Eshelman, Z. Yao, J. Brank, and M. Eberly, "Lifetime characterization of capacitive RF MEMS

switches," *Proc. IEEE International Microwave Symposium*, pp. 227-230, 2001.

3 Fabrication of Graphene

NEM Switching Devices

3.1 INTRODUCTION

This chapter reported the fabrication methods of graphene NEM switching contact devices. Two different fabrication processes were developed in JAIST clean room. In general, fabrication of NEMS devices followed the conventional methods, which were widely applied for the fabrication of MEMS devices, using lithograph technology to define the patterns. In addition, microfabrication techniques such as dry etching and deposition were also frequently utilized to remove or add specific materials. Owing to the requirements of scaling down for NEMS devices, electron beam (e-beam) lithography with high resolution, provided from Elionix, are heavily conducted instead of using photolithography. Graphene NEM switches, which had the drawback of high pull-in voltage, chose global Si back gate to attract the graphene movable element, since it has the difficulty to fabricate local actuation electrode [1]. To fabricate NEM switching devices with low actuation voltage, smaller than 5V, local actuation electrodes were introduced into the processes with two different positions, which were local bottom electrodes and local top gates. Besides, TLM pattern was also introduced into the structure of graphene contact device to investigate the static contact between graphene and metal. Moreover, the contact surface of actuation electrodes was intentionally modified for a detailed study of dynamic contact issues.

All of the developed fabrication approaches started from a heavily p-doped silicon substrate covered with 290 nm of thermal growth oxide. The SiO₂ surface was polished, which has only the surface roughness around 1 nm. The reason to choose the thickness of 290 nm was to introduce a 100-200 nm gap between the graphene and actuation electrode by etching the oxide away. The size of the substrate is 2 cm*1.5 cm.

Before using the substrate, the sample was cleaned by standard cleaning process with acetone and IPA, and two-minute sonication was also applied during the standard cleaning. To fully remove the residuals and an organic solvent, pirana cleaning is applied, following by drying the sample with a gentle nitrogen gas flow.

3.2 FABRICATION OF SWITCHES WITH LOCAL BOTTOM ELECTRODES

To obtain a relatively small switch ON voltage and independence of switching operation, local bottom actuation electrodes were introduced into the fabrication approach of NEM switches. Although, a small air gap distance has the advantage of low pull-in voltage, weak mechanical force due to the small gap distance is difficult to pull-out the graphene movable elements from the contact surface. The air gap distance between the movable element and activation electrodes was intentionally designed as 100-200 nm. Previously, there were several groups reported the graphene NEM switches with local bottom electrodes [2, 3]. Actuation electrodes were initially fabricated on a silicon dioxide substrate with conventional methods, following by burying the local bottom gates with new sacrificial oxide layer formed by plasma-enhanced chemical vapor deposition. However, there was a must to use the mechanical polishing process to obtain a smooth surface for the exfoliation of graphene. In addition, comparing with the thermally grown oxide, the quality of PECVD oxide was still poorer, resulting in a larger leakage current. To achieve almost zero leakage current, it was necessary to keep utilizing the high-quality thermal growth SiO₂. In this section, a new approach to introducing local actuation electrode was demonstrated, and by applying the methods, both graphene-based doubly clamped beam and cantilever types of NEM switches can be achieved. In general, the fabrication process flow is shown in Figure 3.1.

3.2.1 FABRICATION PROCESS

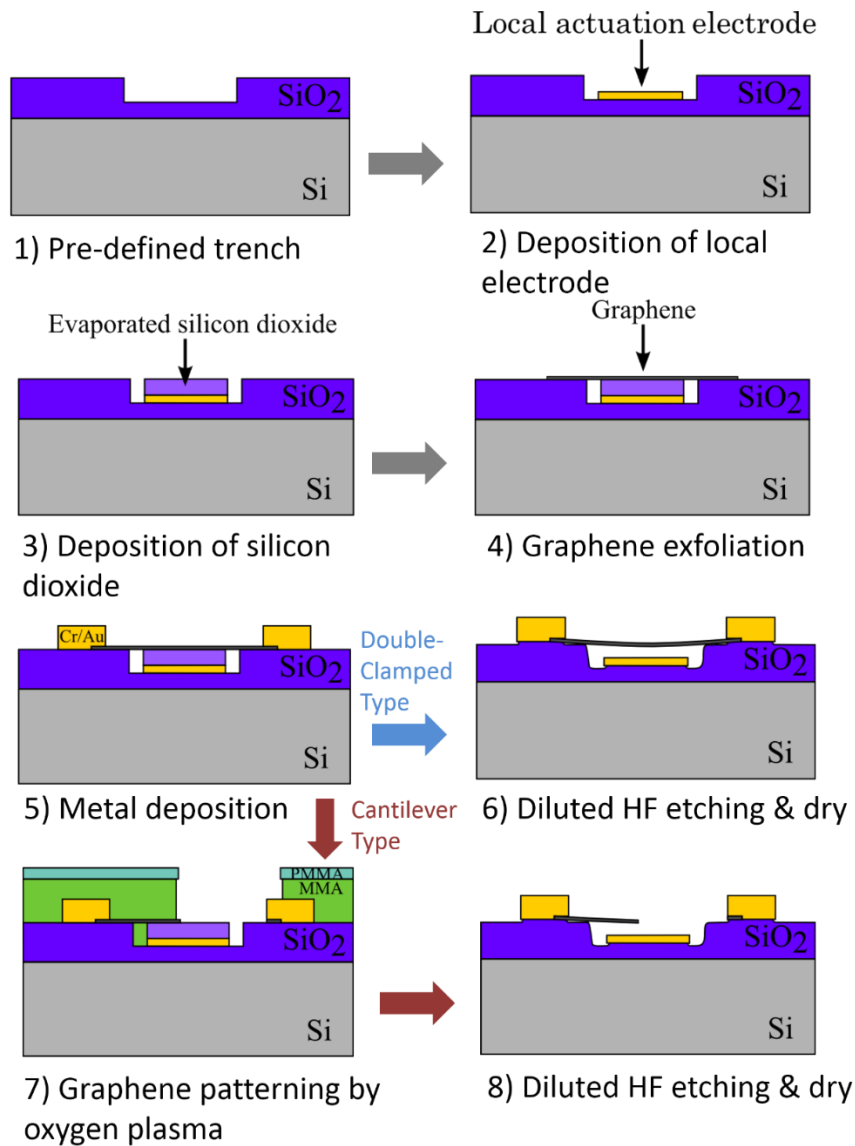


Figure 3.1 Fabrication process of graphene NEM switches with local actuation electrodes.

1) **Pre-defined trench:** the process started with a highly p-doped silicon substrate with 300 nm thermally grown SiO₂. An etching window was opened by the conventional process which did spin coating the positive resist firstly following by an electron beam (e-beam) lithography. The resist called polymethyl methacrylate (PMMA) was utilized as not only a positive e-beam resist but also as the protective layer towards the etching process. Reactive-ion etching (RIE) with tetrafluoromethane (CF₄) gas was applied to etch the unprotected SiO₂ away in a controlled duration. The etching condition and etching selectivity between SiO₂ and PMMA were discussed in detail in later

part of this section. After immersing the sample into acetone for 10 minutes to remove the e-beam resist, the trench was successfully fabricated.

In details, we firstly studied the dry etching rates of PMMA resist towards to the oxygen plasma etching, since it was necessary to protect the undefined area by PMMA resist after the dry etching. Three different dry etching conditions were performed by RIE and Inductively coupled plasma etching (ICP), which was listed in Table 3-1. The samples covered with PMMA resist were exposure by e-beam lithography to define the position of trenches. Then, developed samples were etched for a different duration, and the etched thickness was measured by atomic force microscopy (AFM). Figure 3.2 displayed the relationships between etched PMMA thickness and etching duration. Based on the PMMA etching result, we extracted the etching rates under each dry etching condition by conducting a linear fit, which was shown in Table 3-2. RIE was selected as the method applied to the device fabrication because of the lowest etching rate among the three etching conditions.

Table 3-1 Three different dry etching conditions

Process name	Gas settings	Power settings	Etch duration (s)
ICP1	O ₂ 5 sccm & Ar 40 sccm; 4 Pa	RF 30W; Bias 10W	15, 30, 45
ICP2	O ₂ 5 sccm & Ar 40 sccm; 4 Pa	RF 60W; Bias 50W	5, 10, 15
RIE	O ₂ 20 sccm; 2.6 Pa	20W	10, 20, 45

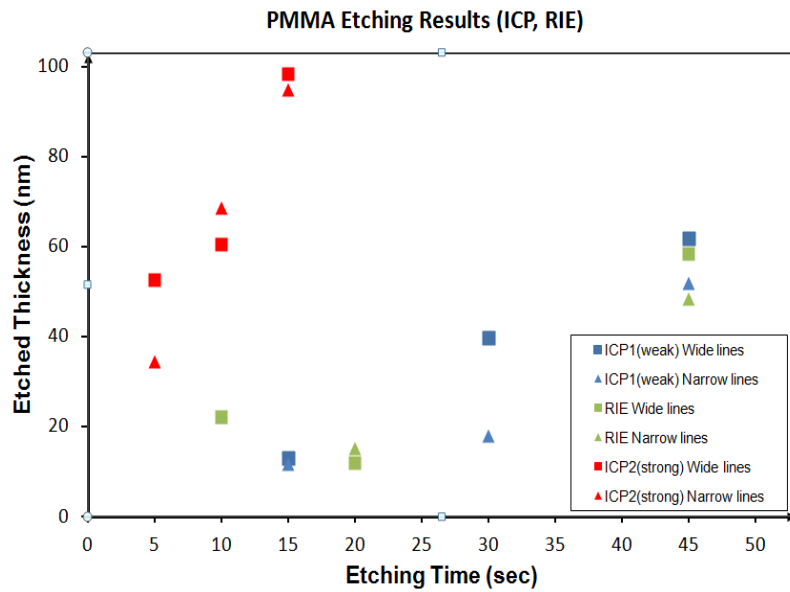


Figure 3.2 Relationships between etched PMMA thickness and etching duration under three dry etching conditions.

Table 3-2 PMMA etching rates under three etching conditions.

Etching Process	Etching rate (nm/sec)
ICP1 (Wide lines)	1.6
ICP1 (Narrow Lines)	1.3
ICP2 (Wide lines)	4.6
ICP2 (Narrow Lines)	6.1
RIE (Wide lines)	1.2
RIE (Narrow lines)	0.9

For the real device fabrication process, large numbers trenches were defined, following with the method mentioned above. Typical optical microscopy and SEM images were shown in Figure 3.3(a) and Figure 3.3(b). The width of the trench is 2.2 μm , and the length is 50 μm . In terms of the depth of the trench, the topographic image was taken by using AFM, and the extracted depth was 200 nm, which were displayed in Figure 3.3(c) and Figure 3.3(d). Since the total thickness of SiO_2 is 290 nm, after defining the trench structure, the thermal-grown SiO_2 was still left.

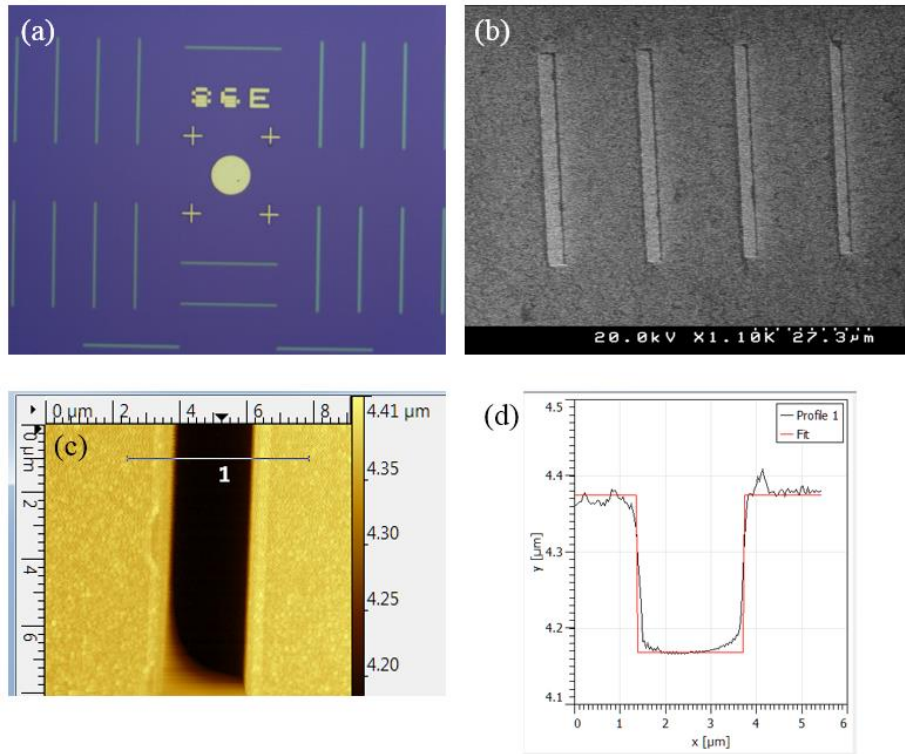


Figure 3.3 (a) Optical microscopy image of pre-defined trenches. (b) SEM image of pre-defined trenches. (c) and (d) Topographic image of a pre-defined trench and the extracted profile.

2) **Deposition of local electrode:** the local gate was introduced into the pre-defined trench during this step. Conventional nanofabrication techniques as e-beam lithography and metal evaporation were applied. To precisely locate the position of local bottom electrodes, the local registration (R3) of e-beam lithography system was conducted, which controls the misalignment distance within 150 nm. For example, if the width of trench is 1.5 μm , the width of bottom actuation electrode will be designed as 1.2 μm . A metal stack consisted of chromium (Cr) and gold (Au) was utilized for the local bottom gate to ensure a linear voltage to current response and also the resistance to strong acid solutions like hydrogen fluoride (HF). A typical thickness of the actuation electrode was 5 nm Cr and 25 nm Au.

3) **Deposition of SiO_2 :** SiO_2 was deposited on the top of local bottom electrodes by the e-beam evaporator. As shown in Figure 3.4, by considering the misalignment distance of the EBL system, evaporated SiO_2 was precisely located into pre-defined trenches, and the height of evaporated SiO_2 kept with the same level of the original thermally grown oxide. The evaporated SiO_2 was

utilized to fill up the trench, which gave a smooth surface for mechanical exfoliation of graphene. The other function of the evaporated SiO₂ was as a sacrificial spacer between the graphene and the local bottom electrode.

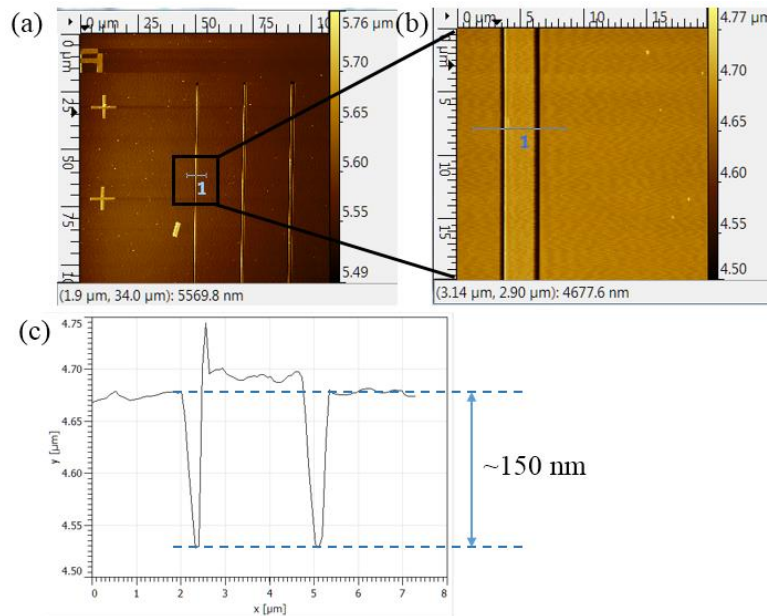


Figure 3.4 (a) and (b) AFM images of pre-defined trenches with evaporated SiO₂. (c) Extracted line profile of the trench with SiO₂.

4) **Graphene exfoliation:** Highly oriented pyrolytic graphite (HOPG) was mechanically exfoliated by the normal dicing tape in a clean room. We transferred the exfoliated graphene on the pre-patterned surface which had local bottom electrodes and evaporated SiO₂ layer. Exfoliated graphene flakes were identified by an optical microscope, and the layer number was confirmed by the Raman spectroscopy. Figure 3.5 illustrated two mechanical exfoliated graphene flakes lying exactly on the top of pre-defined trenches, which were identified by optical microscope and SEM.

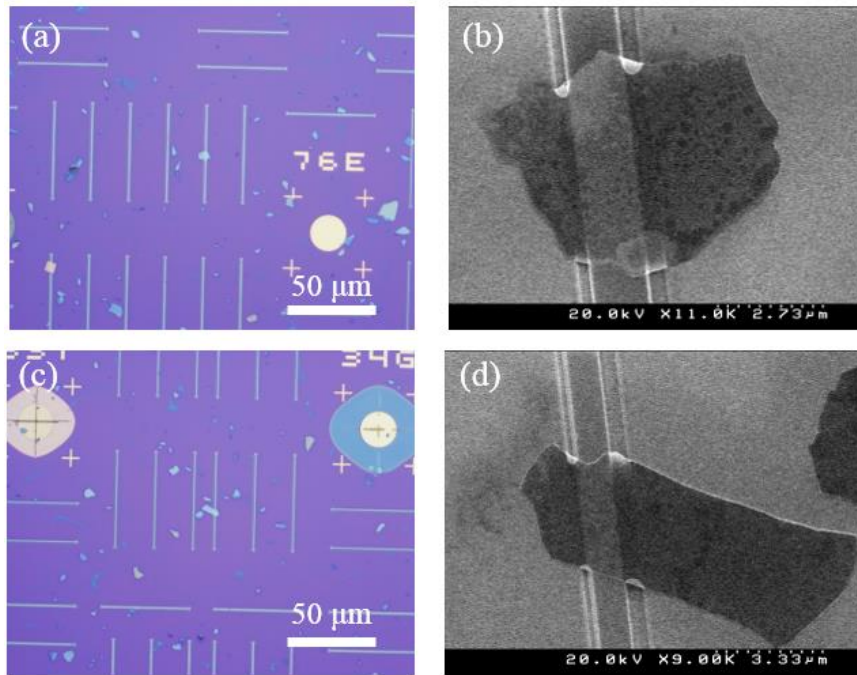


Figure 3.5 (a)-(d) Optical and SEM images of two exfoliated graphene flakes lying on pre-defined trenches

5) **Metal deposition:** E-beam evaporation was utilized to deposit the selected metal for electrodes. Before depositing the metal, e-beam lithography was used to define the area on bi-layer positive resist (PMMA and MMA). The exposure area was removed by the mixed MIBK:IPA solution (1:3), and developing time was carefully controlled, which was 120 seconds. For the deposition, we firstly evaporated 5 nm Cr, which had better adhesive forces to SiO₂ substrate comparing with Au. Then, Au with several tens of nm thickness was directly deposited on the top of Cr layer, which offered Ohmic contacts between two electrodes. The optical images of the device before and after metal evaporation were shown below (Figure 3.6).

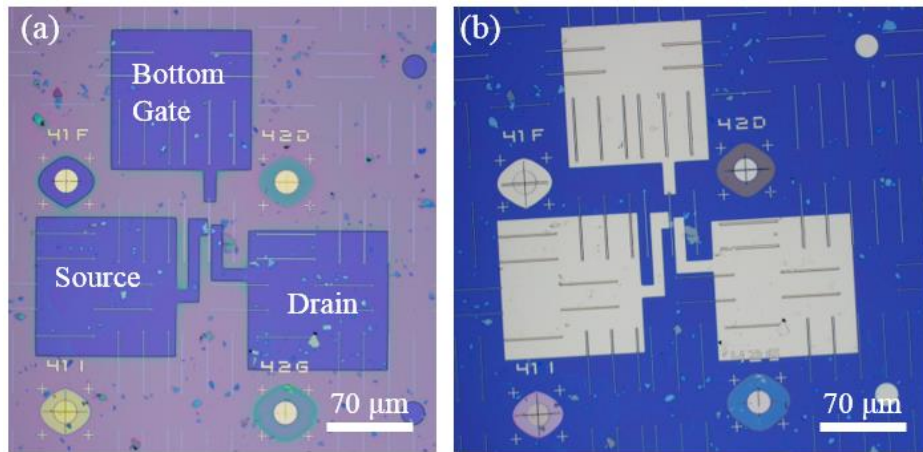


Figure 3.6 (a) and (b) Optical images of the device before and after depositing the metal contact.

6) **Buffered HF etching and dry:** To achieve suspension of double clamped graphene beam, buffered etch solution which comprised a 6:1 volume ratio of NH_4F (40%) and HF (49%) in water was used. The sacrificial layer which was made of evaporated SiO_2 is efficiently etched by BHF, and the typical etching duration was 40 seconds. To avoid the collapse of graphene movable elements owing to surface tension, critical point dryer was performed to dry the etched samples. To be mentioned, BHF etching is isotropic etching, thus not only the evaporated SiO_2 but also the thermal-grown oxide are etched away. The etching rate for thermal oxide is around 1.5 nm/sec, and underetching need to be considered. Bending or strain are possible to be introduced into the double-clamped beam, resulting in the change of pull-in voltage.

7) **Graphene patterning by oxygen plasma:** PMMA resist and e-beam lithography were used to define the etch mask. Reactive oxygen plasma was performed by the reactive ion machine to pattern the exfoliated graphene flakes into specific shapes like ribbon and cantilever. Figure 3.7 showed two PMMA etching masks designed for ribbon shape and cantilever shape.

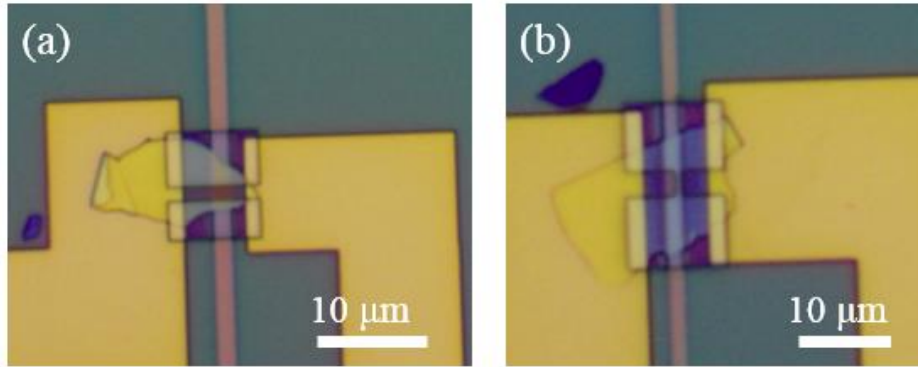


Figure 3.7 (a) PMMA etching mask to pattern ribbon-shaped graphene. (b) Etching mask to pattern two graphene cantilevers.

8) **Diluted HF etching and dry:** The same process with the step 6 mentioned above. Two fabricated cantilever-type GNEM switching devices were shown in Figure 3.8. These SEM images were taken after the device characterization to avoid the charging effect.

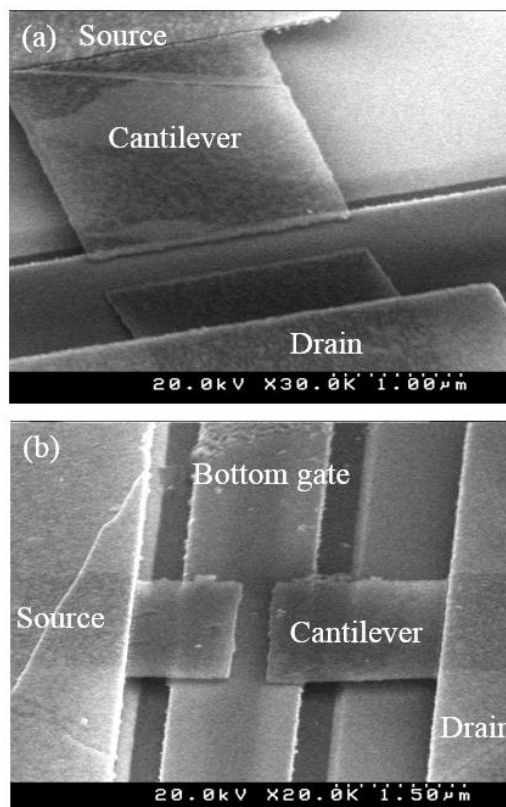


Figure 3.8 (a) and (b) Two fabricated graphene-based cantilever-type NEM switching devices with locally actuated electrodes.

3.2.2 COMPARISON

During the development of fabrication process based on the trench method, the other process was mainly investigated by Jian, which used a polymer sacrificial spacer to achieve local actuation electrode [3]. The fabrication of Jian's method was listed in Figure 3.9. Instead of predefining trenches, the bottom electrode was directly deposited on a 300 nm thermally grown SiO₂ substrate, following with spinning coating a sacrificial polymer layer (PMMA) on the top. Mechanically exfoliated graphene was transferred to PMMA layer, and flakes were identified by an optical microscope. The fabrication of metal contact electrodes was followed by a conventional method. Finally, suspended graphene structure and contact electrodes were achieved by dissolving all the polymer layer with a conventional solvent for lift-off process.

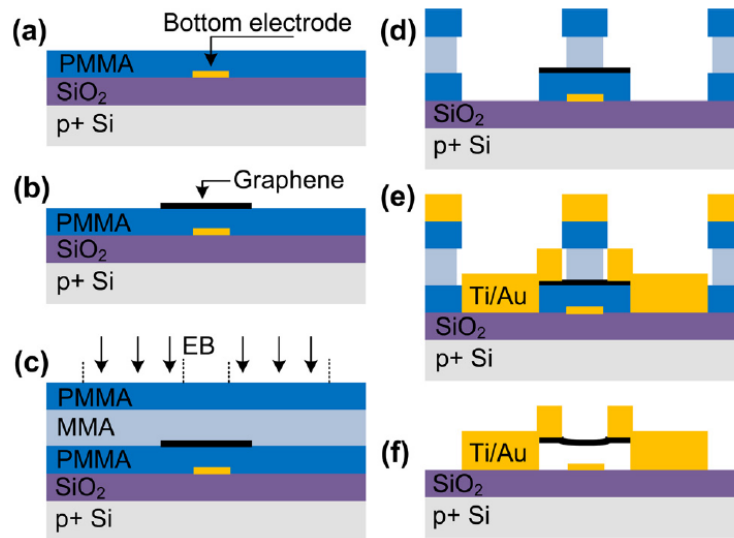


Figure 3.9 Fabrication process of graphene NEM switch with local bottom actuation electrode by using a sacrificial polymer spacer [3].

Comparing the trench-based method with Jian's method, there were two advantages. Firstly, the exfoliated flakes can be patterned into desired shapes such as beam and cantilever, which offered the convenience to investigate the switching performance with a comparable geometry. The other merit is that the air gap thickness can be controlled by the depth of the trench, while the thickness of the sacrificial polymer was almost fixed. The maximum mechanical restoring force which was determined from the air gap thickness between graphene movable element and actuation electrode was critical to overcoming the adhesive forces to obtain the pull-out effect. However, the trench-based method also has a weakness as slanted sidewalls of

the trench, which may result in stiction problem due to the reduce of mechanical restoring force.

3.3 FABRICATION OF SWITCHES WITH LOCAL TOP ELECTRODES

3.3.1 FABRICATION PROCESS

After investigating the existence of Au-C bonding at the graphene to gold contact, the fabrication process must be modified. Besides, comparing with switches with local bottom electrodes, much stronger mechanical restoring was preferred to have bigger chance to achieve pull-out operation. Moreover, the fabrication process was simplified by introducing local top contact electrode instead of a local bottom gate, since a conventional bottom-up process can be followed. The fabrication process of graphene NEM switch with the local top gate was initially developed by Chikuba and Kanetake in Mizuta lab [4, 5]. The process was based a common method to fabricate GNR device, which consisted of mechanical exfoliation, graphene patterning, and deposition of contact metal. After that, as shown in Figure 3.10, a bilayer of hydrogen silsesquioxane (HSQ), which was a negative tone e-beam resist, was utilized as the sacrificial spacer to separate the graphene and top electrode. After depositing metal electrode with a stack of Cr/Au, the top gate was released by the BHF and critical point dryer.

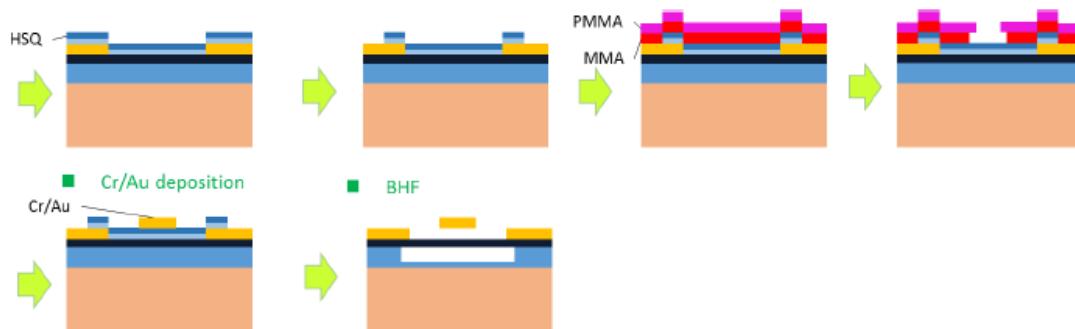


Figure 3.10 Fabrication process of the local top actuation electrode. [4]

3.3.2 FABRICATION OF DYNAMIC CONTACT DEVICE

In this study, a modified process was developed to carefully control the air gap thickness by introducing evaporated SiO₂. Furthermore, in order to investigate the graphene contact, TLM pattern and periodic pattern were introduced into the structure of the device.

All the dynamic contact devices were fabricated on mechanically exfoliated graphene on a SiO₂/Si substrate. The fabrication process of a doubly clamped graphene NEM contact switching device with a local metal top gate and the periodic concave is illustrated in Figure 3.11(c). We transferred a graphene flake mechanically exfoliated from highly oriented pyrolytic graphite (HOPG) onto the thermally grown SiO₂ with the thickness of 290 nm. The fabrication processes are as follows. (1) Polymethyl methacrylate (PMMA) polymer was spun onto the sample. The graphene flake was patterned into a nanoribbon shape by electron-beam (e-beam) lithography and O₂ plasma etching. (2) Then, static contact electrodes were fabricated with a Cr/Au (10/50 nm) metal stack by a conventional microfabrication processes. (3) HSQ, a negative tone e-beam resist, was employed to be patterned into an array of square concaves with high-resolution as a seed of the periodic pattern at the bottom surface of TG. (4) Next, the e-beam-evaporated SiO₂ sacrificial layer was deposited to cover both the GNR and the HSQ pattern. (5) After that, a top contact electrode was fabricated with Cr/Au (5/160 nm) via the conventional methods used in step (2). The deposition rate of the top gate was controlled at a low speed of 0.5-1 Å/s for the first 20-nm-thick metal, assuring good reproducibility of the HSQ patterns from the top surface of the SiO₂ sacrificial layer. (6) Finally, the device was immersed in the buffered hydrofluoric acid (BHF) for removing the sacrificial layer to release the GNR beam, and then the device was dried in the critical point drier in order to prevent the collapse of the suspended graphene nanoribbon due to the capillary force. The fabricated device was placed in ambient condition for eight hours to allow the natural oxidization of chromium at the bottom surface of the TG.

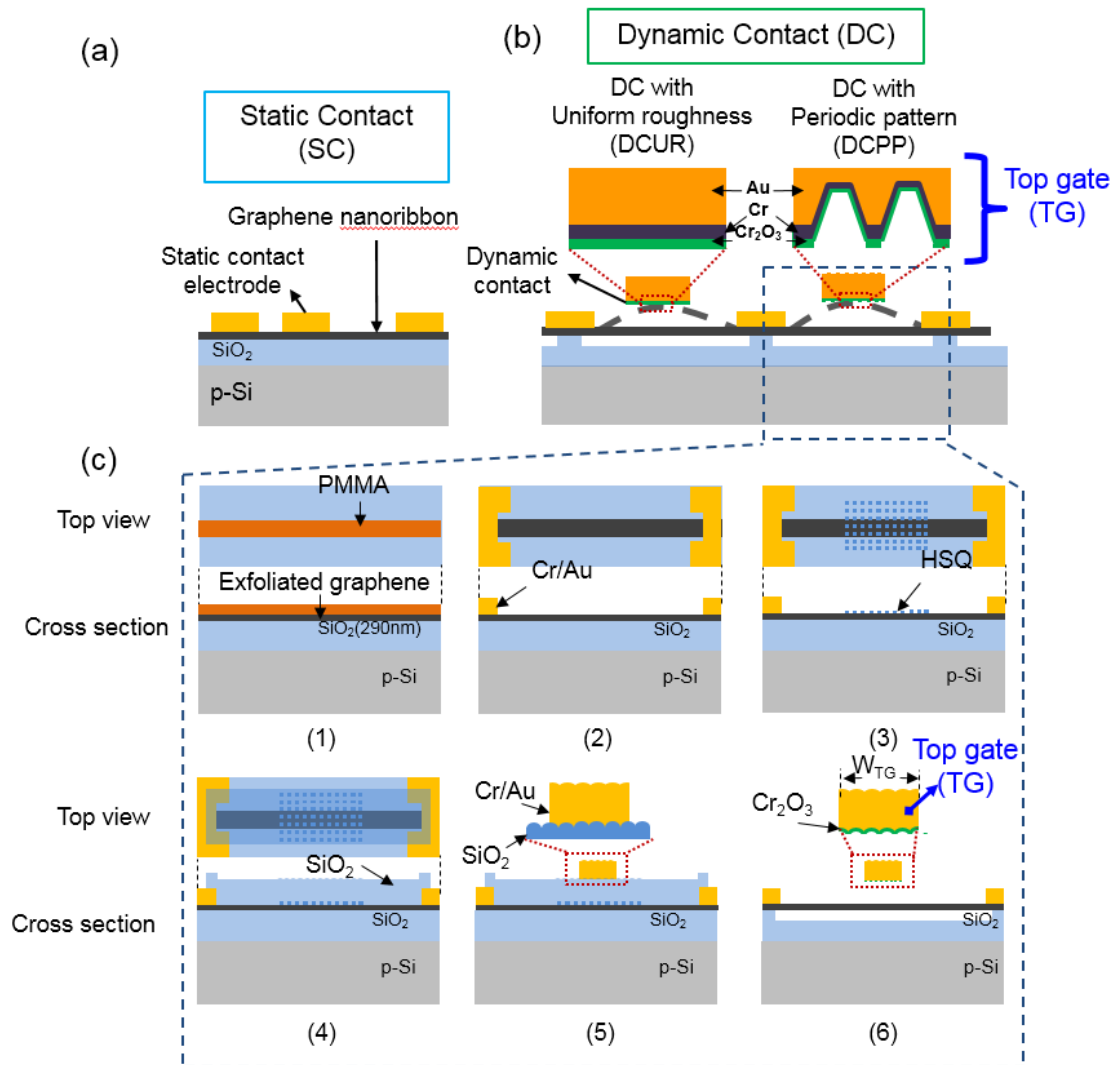


Figure 3.11 (a) Schematic diagram of the static contact GNR device. (b) Schematic diagram of the dynamic contact graphene NEM devices with DCUR and DCPP. (c) Fabrication process of a GNEM switch with periodic patterns on the TG.

- Transmission line method (TLM) pattern:** TLM pattern, which was applied to study the static contact, was added into the fabrication of graphene contact device. At least five contact electrodes were needed for the TLM structure. Thus there was a strong demand of large sizes of exfoliated graphene flakes. Flakes were patterned into long ribbons by oxygen plasma and e-beam lithography. Three fabricated graphene-based static contact devices were displayed in Figure 3.12, and the minimum spacing distance between two adjacent electrodes was 300 nm. Additionally, considering the undercut due to the final BHF process, anchored parts of these contact electrodes were intentionally larger than the area nearby the GNRs.

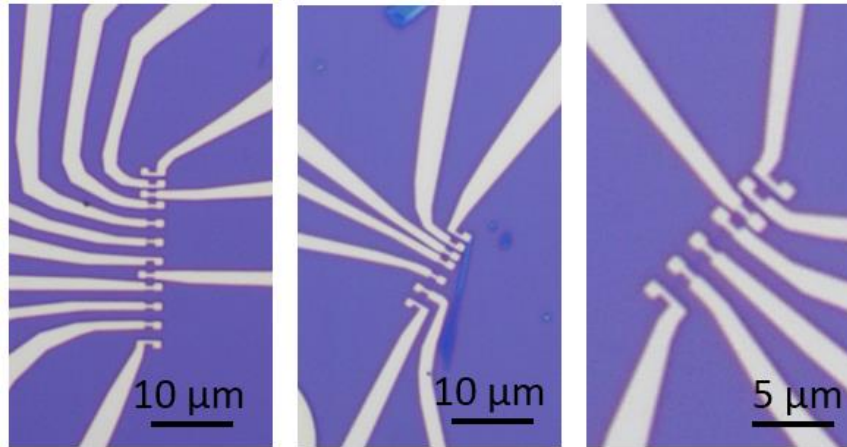


Figure 3.12 Three fabricated graphene static contact devices with TLM pattern.

- Periodic pattern at the contact interface:** The topographic images of the HSQ pattern and e-beam-evaporated SiO₂ sacrificial layer were obtained by AFM as shown in Figure 3.13(a)-2(c). In this work, an array with the designed square dimension of 80 nm and the interspacing distance of 80 nm was used to realize the periodic concave pattern on the bottom surface of the TG to reduce the total dynamic contact area [Figure 3.13 (d)]. The height profile in Figure 3.13 (c) shows that the height of the HSQ pattern was ~20 nm, which is consistent with the thickness of HSQ under a high spin rate (5000 rpm). However, there was a remarkable difference of approximately 7.5 nm in depth between the HSQ and SiO₂ concave patterns. This is mainly due to the evaporated SiO₂ being partly deposited on the slanted sidewall of the HSQ pattern, resulting in a reduced depth when transferring the HSQ periodic pattern to the sacrificial SiO₂ layer. In the case of the bottom surface of the TG with DCP, the profile of the bottom surface should follow the topography of the evaporated SiO₂ layer. Thus, by comparing with the original HSQ patterns, shallower concave periodic patterns with slanted sidewalls were expected to be transferred to the dynamic contact surface. The AFM images in Figure 3.13(e) and Figure 3.13(f) illustrate the device before and after defining the top electrodes (i.e., dynamic contacts). The difference between the designed structure and real results of HSQ patterns was mainly attribute to the proximity effect, which can be optimized by controlling the dose and beam current. These top electrodes have been deposited on the surface with different HSQ patterns on SiO₂, revealing the successful introduction of the periodic pattern into the dynamic contact interface. The

significance of periodic is illustrated in Figure 3.14. We plotted the relationship between the vdW force and separation distance according to the analytical equation, indicating that the critical range of separation distance was under 2 nm. By introducing the HSQ pattern, the separation distance was enlarged, resulting in the large decrease of vdW force.

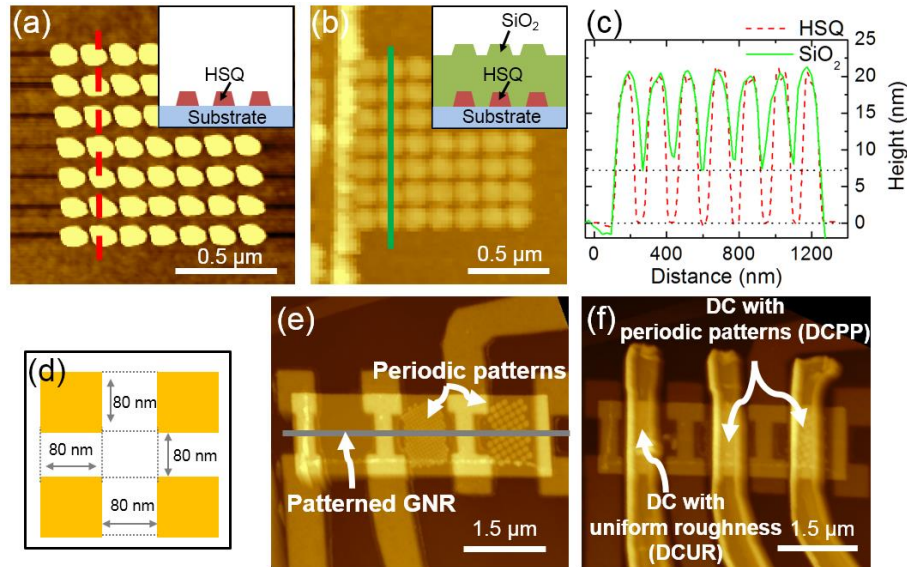


Figure 3.13 (a, b) AFM images of HSQ pattern and deposited SiO₂ on the HSQ pattern. The insets indicate the schematics of the process. (c) Height profiles measured along the dotted red and solid green lines in (a) and (b). (d) Dimensions of the designed HSQ squares array. (e, f) AFM images of the dynamic contact graphene NEM device before and after depositing the TGs. The gray solid line in (e) indicates the patterned GNR.

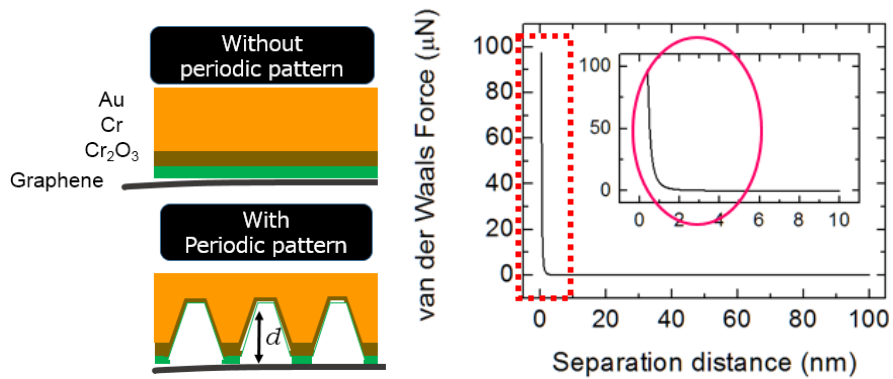


Figure 3.14 Relationship between vdW force and separation distance.

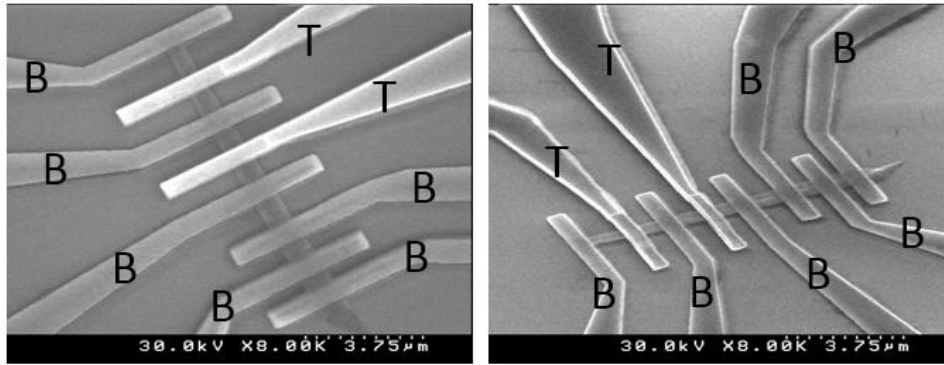


Figure 3.15 SEM images of a typically fabricated graphene contact devices.

SEM pictures of a typically fabricated graphene contact device were displayed in Figure 3.15. Six bottom contact electrodes were fabricated to form the TLM pattern, aiming to study the static contact between graphene to Cr. In addition, two suspended top gates were defined to achieve two graphene NEM switches. For this particular device, the periodic pattern was not included in the top gate, and further characterization of graphene NEM switches and graphene contact devices were demonstrated in the next two chapters.

3.4 SUMMARY

In this chapter, the fabrication process developed for graphene NEM switch with local bottom electrode was introduced firstly. The pre-defined trench was applied to place the local bottom gate. By using this process, both cantilever-type and doubly clamped beam type of graphene NEM switches were fabricated. The weakness of the trench approach was analyzed, and a comparison with Jian' s fabrication process was discussed. After that, the fabrication method of graphene contact device was given, which basically followed the conventional method to fabricate the GNR device with a local top gate. In addition, TLM pattern and periodic pattern originating from the high-resolution HSQ pattern were explained in detail, which were introduced into the fabrication process to investigate the static and dynamic contact between graphene and metal.

3.5 REFERENCE

- [1] Peng Li et al., “Graphene cantilever beams for nano switches,” *Appl. Phys. Lett.*, vol. 101, no. 9, p. 093111, Aug. 2012.
- [2] Z. Shi et al., “Studies of graphene-based nanoelectromechanical switches,” *Nano Res.*, vol. 5, no. 2, pp. 82–87, Feb. 2012.
- [3] J. Sun et al., “Low pull-in voltage graphene electromechanical switch fabricated with a polymer sacrificial spacer,” *Appl. Phys. Lett.*, vol. 105, no. 3, p. 033103, Jul. 2014.
- [4] C. Takuo, “Study of suspended graphene NEMS,” *Master thesis*, 2015.
- [5] K. Nozomu, “Study of graphene NEMS switch,” *Master thesis*, 2015.

4 Study of contacts for graphene NEM switches

4.1 INTRODUCTION

Understanding the contact mechanisms for graphene to metal contact in physics was a challenge. Failure of switching operation was often due to the contact issues like deformation and real contact area, which was widely discussed in RF MEMS. However, there was no detailed study about graphene to metal contact, which was important to improve its reliability. In this chapter, the contact between graphene to actuation electrode was investigated. We started from the graphene NEM switches with local bottom electrodes. Then, by analyzing the graphene contact devices, the static contact and dynamic contact were discussed, respectively. Finally, the deformation type of graphene to chromium oxide was revealed.

4.2 GRAPHENE NEM SWITCHES WITH LOCAL BOTTOM ELECTRODES

Based on the fabrication method described in Chapter 3.2, two types of graphene NEM switches, which were graphene double-clamped beam and graphene cantilever, were fabricated and characterized in vacuum condition. All the measurement was conducted in a closed probe station provided by the company called System Brain. Besides, the probe station was connected to the semiconductor analyzer, Agilent B1500A. Figure 4.1 displayed two measured devices. One was the double-clamped device with the beam length of 1.5 μm and 120 nm air gap thickness, and the other device was graphene cantilever type, which had a 500 nm-long cantilever and the gap

distance of 90 nm. Multilayer graphene was used for both devices to obtain a strong mechanical restoring force. A two-terminal measurement configuration was applied to both kinds of devices, shown in the insets of Figure 4.2. As the applied voltage increased, the current between the graphene movable elements and local bottom electrode were monitored.

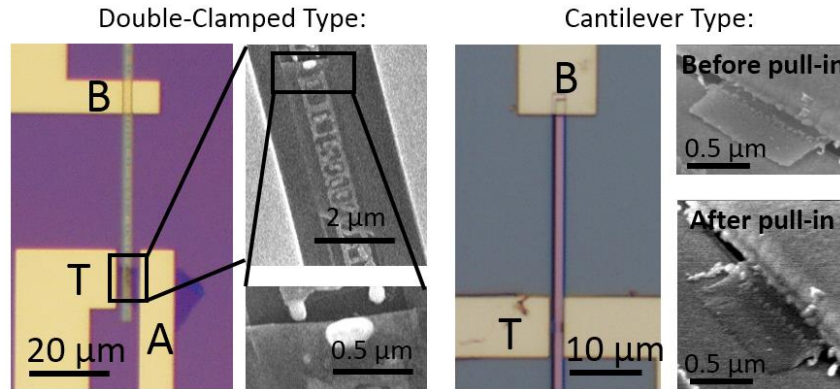


Figure 4.1 Double-clamped type and cantilever type of graphene NEM switches

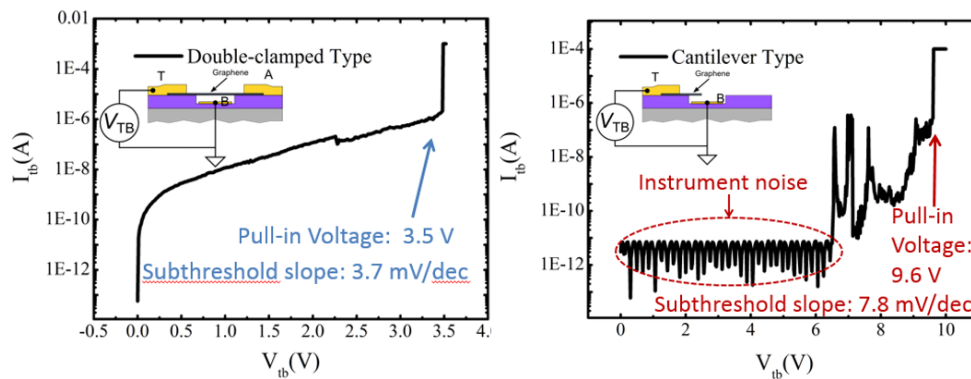


Figure 4.2 Measurement configurations of both double-clamped type and cantilever type of graphene NEM switches.

Clear and sharp pull-in behaviour were observed on both devices at the voltage of 3.5 V and 9.6 V, respectively. A very low pull-in voltage was obtained, lower than 5 V, which was compatible with the modern CMOS techniques. Theoretically, the pull-in voltage of cantilever type of device should be smaller than that of clamped beam device owing to a weaker spring constant. In this study, due to a thicker layer thickness of graphene for the cantilever switch, which was understood from the Raman spectroscopy, larger pull-in voltage was measured. By reducing the layer number to bilayer or monolayer graphene, the reduce of pull-in voltage can be expected. However, both of the devices suffered from a stiction failure after the pull-in operation. The formation of Au-C chemical bonding was attributed as the main reason of the stiction

[1]. Besides, slanted sidewall was observed at the predefined trench by using AFM, which may result in a decrease of mechanical restoring force and increase of adhesive force like vdW force. Based on those issues mentioned above, we changed to graphene NEM switches with local top gate, which offered a different contact mechanism.

By using Jian's method, another bilayer graphene GNEM switch was fabricated. The layer number was confirmed by the Raman spectroscopy, since four Lorentzian sub-peaks were fit to the 2D band of the spectroscopy of graphene. The optical and AFM images of the fabricated device were displayed below, and the length and width of the graphene ribbon were 2.5 μm and 1.5 μm , respectively. From the electrical characterization, the device showed small leakage current before the physical contact between the graphene beam and the bottom actuation electrode. At the voltage of 1.8, a sudden increase in current was observed, which was regarded as the pull-in voltage, and the pull-in voltages were stable during the first several cycles. However, at the final cycle, the current did not return to the background leakage level even the applied voltage was back to 0 V. Permanent stiction between the graphene and gold was observed, which was attributed to the Au-C chemical bonding.

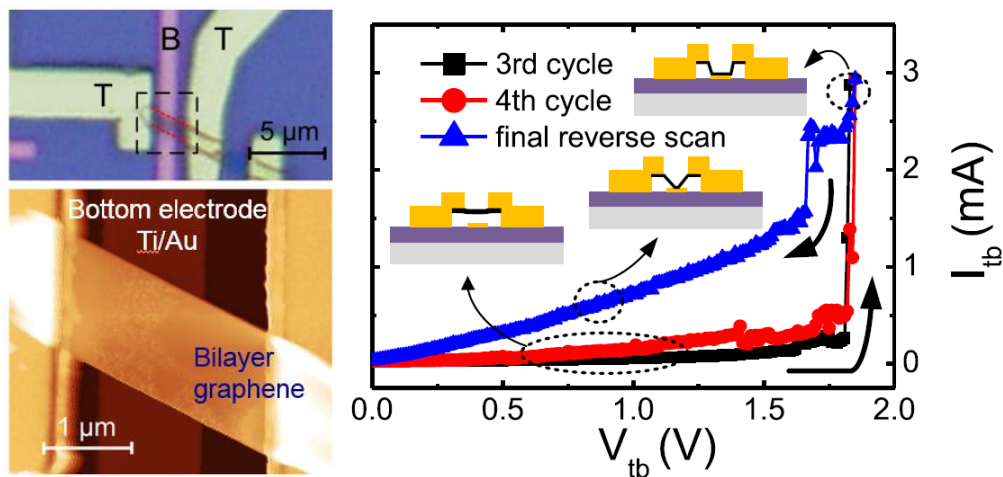


Figure 4.3 The optical, AFM images and electrical characterization of the fabricated bilayer GNEM switch with a local bottom actuation electrode [1].

4.3 GRAPHENE CONTACT DEVICE

The total contact resistance of our graphene NEM switches was obviously composed of the static contact resistance at the clamping points and the dynamic contact resistance between the movable graphene and the top gate. TLM method was introduced into graphene contact device to study the graphene/Cr contact. Moreover,

by introducing local top contact electrode with the metal stack of Cr/Au, the dynamic contact was changed to graphene to chromium oxide because of the existence of instant oxidation of Cr layer. In addition, we also introduced a periodically patterned square concave array at the dynamic contact interface, aiming to reduce the GNR-contact stiction force. This pattern made the contact area, and hence the van der Waals (vdW) interaction, smaller and was expected to facilitate the reversible switching operation.

4.3.1 STATIC CONTACT STUDY

In the TLM measurement, the total resistance (R_{total}) between two adjacent static contact electrodes consists of the resistance of the graphene channel (R_G) and the static contact resistance (R_C) at the graphene to metal contacts [2]. The relationship between R_{total} and R_C is shown by

$$R_{\text{total}} = R_G + 2R_C = \frac{\rho_G}{W}L + 2R_C . \quad (1)$$

where L and W are the length and width of the GNR channel, respectively, and ρ_G is the contact electrodes is regarded as a function of the length (L) in the TLM equation. The contact resistance is extracted from the intercept at $L = 0$ of a linear fit of Eq. (1). All the measurements are conducted at room temperature and a low pressure of ~ 0.1 Pa to reduce the influence of the atmospheric environment.

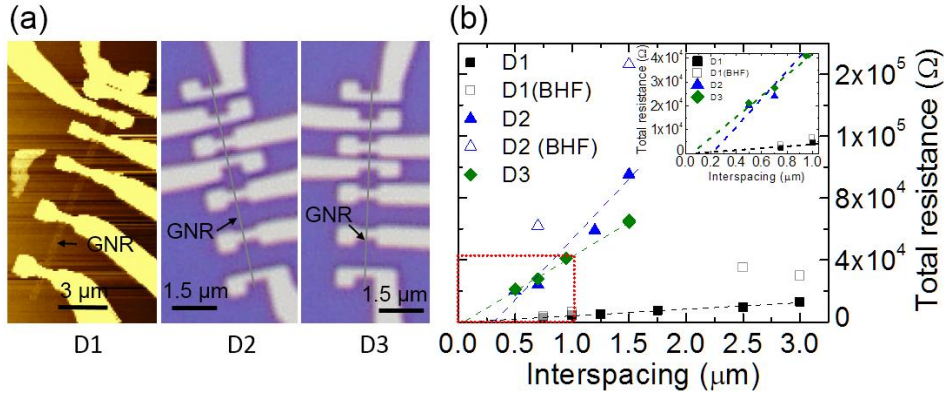


Figure 4.3 (a) AFM image of contact device D1 and optical microscopy images of devices D2 and D3. Grey solid lines (D2, D3) indicate the location and shape of the GNRs. (b) TLM fitting for contact devices D1, D2, and D3. Overall resistance of D1 and D2 after BHF etching. The inset shows the fitting results for a small range of interspacing distances (0-1 μm).

Initially, we deposited the Cr with a slow rate by the e-beam evaporator to ensure a static contact between Cr-graphene-SiO₂, the static contact resistance we analyzed

was between graphene - Cr interfaces. For this purpose, we fabricated three static contact devices based on the patterned bilayer graphene nanoribbons (GNRs) (D1, D2, and D3), which were indicated in the AFM and optical images in Figure 4.3(a). The GNRs for these three devices were 400, 140, and 120 nm, in width, respectively. The measured total resistance shows good linear dependence on L, and the static contact resistance extracted from the intercept of the fitting lines displays slightly negative values. The inset of Figure 4.3(b) displays the TLM fitting for a small interspacing range indicated by a red dotted rectangle, and the intercept values extracted from linear fitting for D1, D2, and D3 are -218.6, -23497, and -2060.3 Ω , respectively. The contact resistance originating from carrier injection/extraction at the interface of graphene to Cr should be positive [3]. The negative contact resistance from the TLM measurements is primarily due to the underestimation of the inhomogeneity of the GNR channel and the impacts from metal or surrounding insulators [4]. Charge puddles and carrier doping from the metallic electrodes and substrates are dominant origins of the carrier inhomogeneity in the contact and channel regions [5, 6]. The impacts of the material deposition and acid etching can also be vital. All the fabricated static contact devices showed an overall increase in total resistance after the GNR channels were suspended as a result of the BHF etching. The total resistances measured for some of the D1 and D2 devices are shown for comparison by using squares and triangles in Figure 4.3(b). Because of the high acidity and the undercut of SiO₂, the graphene/Cr bonds at the static contact interface weakened, which will result in the increase in contact resistance.

4.3.2 DYNAMIC CONTACT

To analyze the dynamic contacts of the GNR and Cr/Au contacts, four different double-clamped GNEM switches were characterized. Details of these switches are given in Table 4-1. GNEM switches A and B have uniform microscopic roughness under the TG, as shown in Figure 4.4(c). The bottom surface of the TG for GNEM switches C and D have the periodic concave structure created using controlled HSQ arrays (Table 4-1), which leads to reduced surface roughness area, as shown in Figure 4.4(f).

Table 4-1 Table Device parameters of the dynamic contact GNEM switches, A-D.

	A	B	C	D
Periodic patterns	No	No	Yes	Yes
Length of GNR, L (μm)	1.5	1.5	1.5	1.5
Width of GNR, W (μm)	0.5	0.2	0.2	0.2
Air gap, g_0 (nm)	70	65	90	90
Contact length, L_c (μm)	0.5	0.5	0.5	0.5
Layer number of graphene	1	Multi (3 nm)	Multi (3 nm)	2
Measured pull-in voltage (V)	3.4	3.7	7.4	3.9
Calculated pull-in voltage (V)	0.47	2.8	4.5	1.25

The two-terminal measurement configuration shown in the inset of Figure 4.4(a) was used to characterize the switching performance. By gradually increasing the actuation voltage V_{TB} between top gate and bottom contact electrodes, and electrostatic force increased with the electric field between the top gate and bottom contact resulting in the deflection of the GNR. At the pull-in voltage, the electrostatically deflected graphene which overwhelmed the mechanical restoring force formed a physical contact with the top gate. A sudden increase in the current I_{TB} from the leakage level was expected to be observed owing to physical contact. All these measurements were conducted by a semiconductor analyzer (Keithley 4200 SCS).

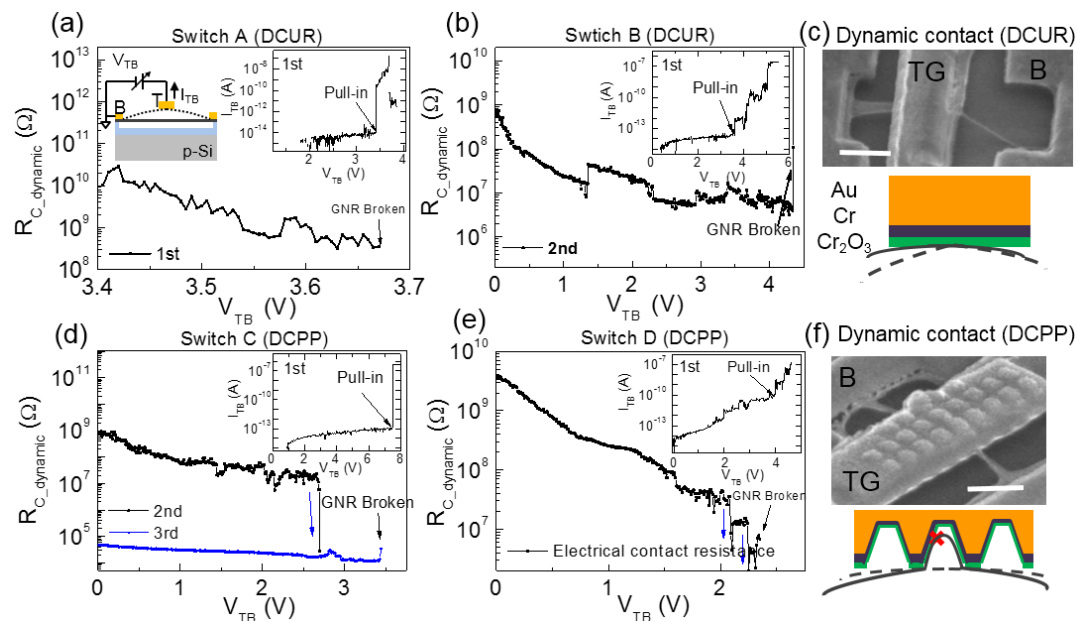


Figure 4.4 (a, b) Characterization of dynamic contact resistance of two graphene-based NEM switches A and B with uniform roughness on TG (DCUR). Insets: I_{TB} - V_{TB} curves of the 1st switching operation, and the two-terminal measurement configuration for the dynamic contact study. (c) SEM image of device A after the measurement; scale bar: 0.5 μm . Schematic diagram of graphene-TG contact with the uniform roughness

surface (DCUR). (d, e) Characterization of dynamic contact resistance of switches C and D with the periodic patterns on the bottom surface of the dynamic contact (DCPP), as shown in (f). Inset: ITB-VTB curves of the first switch operation. (f) SEM image of device D after the measurement; scale bar: 0.3 μm . Schematic diagram of graphene-TG contact with the periodic patterns.

The insets of Figure 4.4(a), 5(b), 5(d), and 5(e) depict the initial pull-in of all four GNEM switches A, B, C, and D. The pull-in voltage is marked by arrows. Note the abrupt and clear pull-in operation as expected for GNEM switches. At low V_{TB} , only the pico-ampere level currents were measured, which was the leakage current indicating the open contact between the TG and the graphene beam. This is normally considered as the “OFF” status of a switch. The ON states of these switches were defined at the voltage when the corresponding current suddenly changed by approximately two orders of magnitude from the leakage (OFF states) to high current. At the voltage of 3.4 V (Switch A), 3.7 V (Switch B), 7.4 V (Switch C), and 3.9 V (Switch D), abrupt increases in current were observed, indicating the physical pull-in of the graphene beam onto the bottom surface of the TG. For GNEM switch A, the lowest pull-in voltage of 3.4 V was achieved due to the monolayer graphene. On the other hand, GNEM switch D, showing a reasonably low leakage current in the pico-ampere range, exhibited a slightly higher $V_{\text{pull-in}}$ of 3.9 V presumably due to the use of a thicker bilayer graphene. Owing to the uneven contact surface from the concave patterns, another sudden increase in contact resistance was observed. The air gap between the TG and GNR was reduced to 65 nm for GNEM Switch B, which resulted in a relatively low $V_{\text{pull-in}}$ of 3.7 V even with multilayer GNR. The step-like behavior in the inset of Figure 4.4(b) was attributed to the contact with the lift-off ears at the TG. However, the multilayer GNR with 90 nm air gap (GNEM switch C) showed the highest $V_{\text{pull-in}}$ of 7.4 V.

The pull-in voltage of the doubly clamped beam is given by

$$V_{\text{pull-in}} = \sqrt{\frac{8Kg_0^3}{27\varepsilon_0WW_{\text{TG}}}}, \quad K = \frac{32EWt^3}{L^3}, \quad (2)$$

where K is the spring factor of the graphene double-clamped beam, g_0 is the initial gap between the dynamic contact and the suspended graphene beam, ε_0 is the vacuum permittivity, E is the Young's modulus of graphene, L and W are the length and width of the GNR, respectively, and t is the beam thickness, which is closely related

to the layer number of graphene. W_{TG} is the width of the TG shown in Fig. 1(c). The measured and calculated pull-in voltage are given in Table 4-1. For simplicity, the pull-in voltage for the GNEM switches with the periodic pattern TG (GNEM switches A and B) were calculated by assuming the same footprint as that for the uniform roughness devices (GNEM switches C and D). A quantitative comparison of the measured and calculated pull-in voltage did not show good agreement. Nevertheless, the trends observed with variations in GNR thickness and air gap appear consistent with the calculations. An increase in effective gap distance expected as a result of the release of strain and also the degradation of the contacts due to the undercut of SiO_2 after the BHF etching could be possible origins for the increase in measured pull-in voltage.

However, after the initial pull-in operation, a finite conductance remained between the top and bottom contacts, which implies that the graphene beam is still in contact with the TG even after the applied voltage was set to 0 V. All four GNEM switches showed irreversible characteristics after the initial pull-in operation. It was expected for GNEM switches with the periodic pattern that contacts would facilitate the pull-out operation owing to the reduced contact area. However, no reversible switching operation was observed for GNEM switches C and D. It is likely that the mechanical restoring force was generally insufficient for achieving the pull-out operation. The formation of carbon – metal chemical bonds is unlikely in our present devices because of the presence of a thin Cr_2O_3 layer in the dynamic contact [1].

To obtain detailed information on the dynamic contact characteristics to investigate the switching failure mode after the initial pull-in stiction, we performed electrical contact resistance (ECR) analysis in all of these GNEM switches [7]. Traditional microscopy techniques cannot be used to conduct the in situ monitoring of the NEM contact interface. ECR analysis is used as an in-situ diagnostic tool to study the contact interface behavior of the microelectromechanical system (MEMS) [8-10]. Owing to the presence of a thin chromium oxide layer and periodic concave patterns at the contact surface, we monitored the change in dynamic contact resistance at the graphene-top gate contact interface by gradually increasing the electrostatic force. In this case, we used the same measurement configuration shown in Figure 4.4(a). Figure 4 shows the measured characteristics of the applied voltage versus ECR (i.e., $R_{C_dynamic}$) for all four switches. In Figure 4.4(a) and 4(b), the dynamic contact resistance steadily

decreases with the increase in electrostatic force, which indicates the gradual increase in contact area with applied electric field, as indicated in Figure 4.4(c). By contrast, a sudden decrease in dynamic contact resistance for the graphene switches with the periodic pattern is observed [Figure 4.4(d) and 5(e)]. We succeeded in observing the 3rd measurement cycle only for GNEM switch C as the burnout of the GNR was avoided during the 2nd measurement by setting the current compliance appropriately. The contact resistance measured from the results of the 3rd evaluation retained the same order of values at the end of the 2nd measurement. The other switches suffered from burnout at the end of the 2nd measurement cycle as indicated in the individual figures. In terms of GNEM switch D, the contact resistance was gradually decreased in the same manner as switches A and B at the beginning, indicating a steady increase in contact area. However, at a voltage of 2.08 and 2.24 V, two sudden drops by about one order of magnitude in contact resistance were observed. We attributed these sudden contact changes to the locally abrupt pull-in of the GNR to the inner slanted sidewall of the concave patterns, which is illustrated in Figure 4.4(f). Suspended GNRs were first pulled-in onto the natural Cr₂O₃ on top of the concave globally, and then some of the GNRs were physically broken beyond a certain critical voltage, as shown in the SEM image in the inset in Figure 4.4(c). This breakdown might be assisted by the point defects and edge irregularities in the GNR [11, 12]. In the case of GNEM switch C, a very high current density of 0.5×10^{-2} A/ μm was reached before the GNR was broken. This is consistent with the observation of breakdown current density due to second-order three-phonon scattering in the suspended exfoliated graphene ribbon [13]. The other switches A, B, and D, might have reached such a high current density just before GNRs were broken down.

4.3.3 FINITE ELEMENT METHOD SIMULATION

Interestingly, the second pull-in was observed for the DCPN NEM switches, as shown by blue colored arrows in Figure 4.4(d)-4(e), which is attributable to the GNR pulled-in locally onto the sidewalls in the concave. To verify our scenario, we performed a 3D FEM simulation as follows.

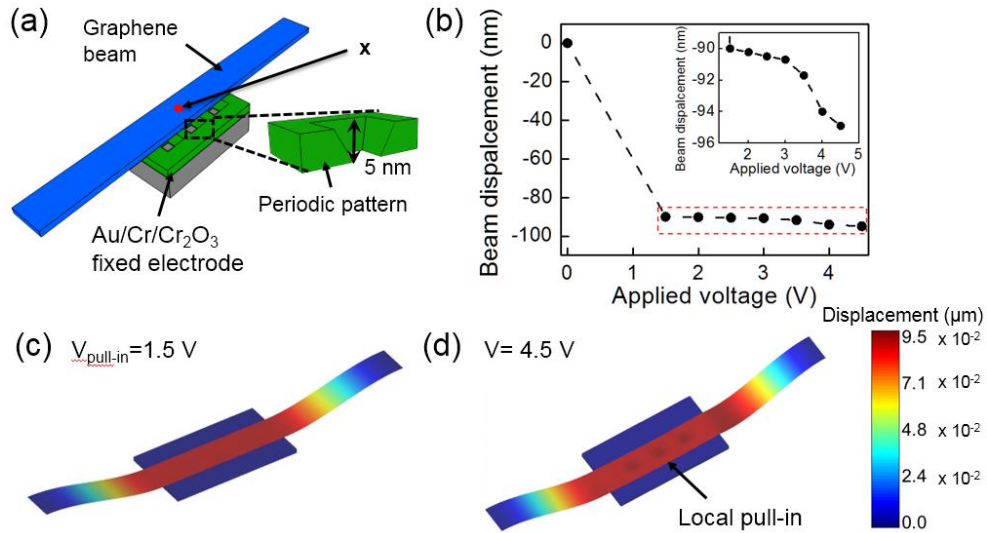


Figure 4.5 (a) FEM model of a graphene NEM switch with the periodically patterned electrode. Dimensions are based on the measured switch D. (b) One-dimensional plot of beam displacement with the applied voltage. Inset: 1D plot of beam displacement after initial pull-in. (c) Beam displacement at pull-in voltage of 1.5 V. (d) Beam displacement in the periodic concave patterns (4.5 V). Displacements in (c) and (d) are indicated by the same colour bar.

The electrical and mechanical properties of the NEM contact switches were analyzed by FEM based on the software, IntelliSuite [14]. The dimensions were adapted from the experimental GNEM switch D (Table 4-1). The GNR was modelled as an isotropic and elastic material with a thickness of 0.7 nm. The initial air gap between the suspended graphene beam and the substrate is 90 nm. The concave periodic patterns with slanted-sidewall surfaces with a depth of 5 nm were included. The model was meshed with mechanically adaptive meshing to refine the deflection of the suspended beam locally. Figure 4.5(a) illustrates the geometry of the doubly clamped GNEM switch and the periodic concave patterns of the actuation electrode. The material properties of the graphene were obtained from Ref. 15. Figure 4.5(b) shows the graphene beam displacement with the applied voltage. The displacement was measured at the centre of the suspended graphene beam denoted as X in Figure 4.5(a). The pull-in occurred at 1.5 V, at which the beam displaced by 90 nm and made contact with the bottom electrode [Figure 4.5(c)], which was considered as the overall pull-in. When the applied voltage was increased beyond the pull-in voltage, the beam started to pull-in into the slanted concaves. The displacement of the graphene beam inside the concave

pattern is shown in the inset of Figure 4.5(b), and the local pull-in was observed from the simulation. Figure 4.5(c) visualizes the beam deformation at the pull-in voltage. Moreover, Figure 4.5(d) shows the beam displacement inside the concaves at the voltage of 4.5 V. It is evident from Figure 4.5(d) that the beam pulled-in locally inside the periodic concave patterns.

4.3.4 COMPARISON WITH CLASSIC DYNAMIC CONTACT MODELING

For an understanding of the GNR dynamic contacts, we also performed classical dynamic contact modeling analysis of the ECR characteristics. The contact forces generated at the dynamic contact interface are defined as the difference between the electrostatic force and the mechanical restoring force, and the electrostatic force and the mechanical restoring force of a doubly clamped beam are expressed as [16, 17]

$$F_{\text{contact}} = F_{\text{electrostatic}} - F_{\text{restoring}} , \quad (3)$$

$$F_{\text{electrostatic}} = \frac{A\epsilon_0\epsilon_r V^2}{2(g_0-d)^2} , \quad (4)$$

$$F_{\text{restoring}} = Kd , \quad (5)$$

where A is the area of the electrodes, ϵ_0 and ϵ_r are the vacuum permittivity and relative permittivity of the medium between two electrodes, respectively, V is the applied voltage, g_0 is the initial gap between two electrodes, d is the beam deflection distance, and K is the spring factor of the beam mentioned above. The thickness of the graphene was extracted from the AFM image (Table 4-1). In our dynamic contact study, after the graphene reaches the pull-in state, the electrostatic force tends to be infinite from Equation (4). However, we should consider the existence of thin naturally oxidized chromium oxide (Cr_2O_3) as the medium between two electrodes. Approximately 1-nm-thick natural Cr_2O_3 can be assumed, and its dielectric constant is 11.8 [18]. In addition, the initial gap thickness was chosen as the deflection distance for calculating the mechanical restoring force, since the graphene remained in contact with the TG during the measurement. The applied voltage versus dynamic contact resistance for NEM switches B, C & D were converted to the contact force versus contact

resistance (Figure 4.6) using the method mentioned above. Two classical dynamic contact resistances models of elastic and plastic deformation types were applied to the graphene/Cr₂O₃/Cr interface [17]. Elastic modeling is generally for contacts with relatively low contact forces where the deformed surface can return to its original shape after removing the contact force. In contrast, permanent surface change occurs owing to the displacement of atoms in the plastic deformation [17].

Equations (6) and (7) display the relationship between the contact force F_{contact} and the dynamic contact resistance ($R_{C_dynamic}$). R_{cDE} is the elastic material deformation dynamic contact resistance, while R_{cDP} is the plastic deformation dynamic contact resistance [19]. The relationship between the contact resistance and the contact force for elastic and plastic contacts is given by

$$R_{cDE} = \frac{\rho}{2} \left(\frac{4E'}{3RF_{\text{contact}}} \right)^{\frac{1}{3}}, \quad \frac{1}{E'} = \frac{1-v_1^2}{E_1} + \frac{1-v_2^2}{E_2}, \quad (6)$$

$$R_{cDP} = \frac{\rho}{2} \left(\frac{H\pi}{F_{\text{contact}}} \right)^{\frac{1}{2}}, \quad (7)$$

where E' is the Hertzian modulus, and E_1 and E_2 are the elastic modulus; v_1 and v_2 are Poisson's ratios for two contact materials. ρ is the resistivity of the conducting material, R is the asperity peak radius of curvature, and H is the Meyer hardness of the softer material. Here, Young's modulus and Poisson's ratios of graphene and Cr₂O₃ are 1 TPa, and 0.165, and 124 GPa and 0.25, respectively [20-22]. The Meyer hardness of Cr₂O₃ is 21 GPa [23].

The dynamic contact resistances measured for GNEM switches B, C, and D were analyzed using both elastic and plastic deformation contact models in Figure 4.6. The measured curve has a large offset in contact resistance with these models. This is only attributed to the diffusive current flow considered in these models (Eqs. (6) and (7)). Other conducting modes such as ballistic or quasi-ballistic are not included. These two classic models basically follow the power law, resulting in a proportional relationship between contact force and the contact resistance. The difference between these two models was mainly observed for a small contact force range. Interestingly, for all these GNEM switches, the measured dynamic contact resistance showed good agreement

with the plastic deformation model, $R_{cDP} \propto F_c^{-\frac{1}{2}}$, which was illustrated by the magnified plots in Figure 4.6.

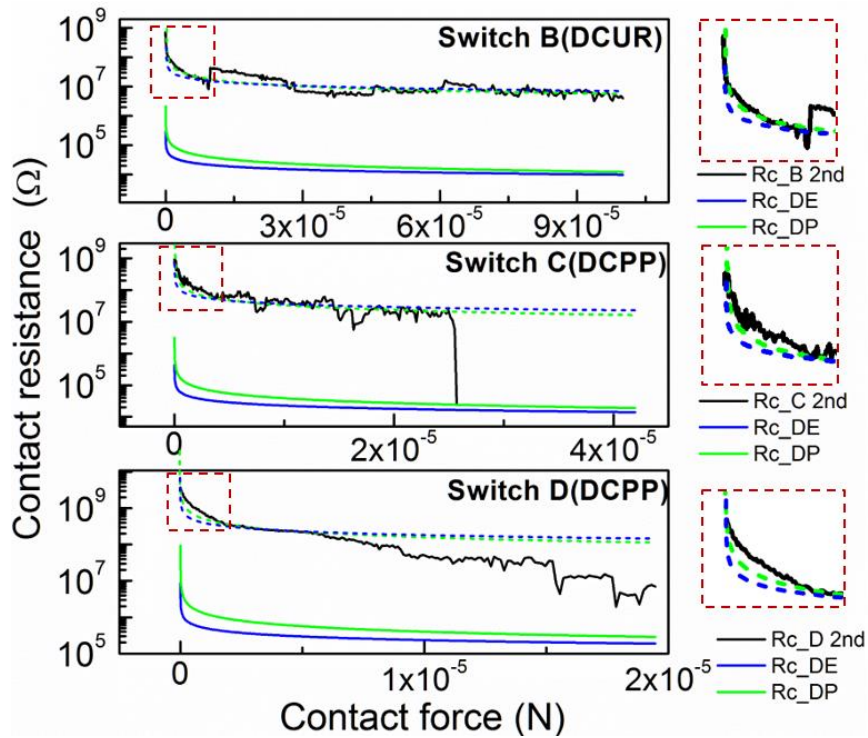


Figure 4.6 Contact force versus contact resistance curves from measured GENM switches B, C, and D and two dynamic contact models of elastic and plastic deformations. Dotted lines: shifted contact resistance of two classical models to compare with the measured results. Magnified plots: comparison between the experimental results with two contact models for small contact force ranges.

4.4 SUMMARY

First of all, both cantilever-type and beam-type of graphene NEM switches with local bottom gate were measured, showing abrupt pull-in at low voltage. However, both of the devices failed due to the stiction from Au-C bonding. After that, graphene contact devices were investigated. We reported graphene-metal contacts by fabricating the transmission line model (TLM) pattern of Au/Cr static contact electrodes onto a graphene nanoribbon (GNR), which was cointegrated with GNR nano-electro-mechanical (GNEM) switches and suspended top electrodes for dynamic contacts. The static contacts showed the linear channel length dependence of total resistance, which

was amenable to the standard TLM theory. The slightly negative contact resistance extracted from the TLM analysis was attributable to the inhomogeneity of the GNRs due to the doping from the metal and the substrate. To investigate the Au/Cr – GNR dynamic contact properties, we introduced two types of Au/Cr actuation electrode surfaces with and without a lithographically patterned periodic array of square concaves, which were expected to reduce the Au/Cr – GNR stiction effectively. For both surface structures, clear pull-in operations were observed for the GNEM switches with doubly clamped mono-, bi-, and multilayer GNRs. However, none of the GNEM switches achieved pull-out operation regardless of the introduction of the periodic surface pattern. It was found for the periodically patterned dynamic contacts that the GNRs first showed global pull-in onto the top surface of the pillar array and then exhibited local pull-in onto the slanted sidewall surfaces of the concave, resulting in an increase in stiction. Such a local pull-in phenomenon was confirmed by 3D FEM simulation. In addition, plastic deformation at the contact, increasing the vdW interaction, was observed as a result of the local pull-in failure mode, which completely hindered the GNRs from pulling out from the contact surface.

4.5 REFERENCES

- [1] J. Sun, W. Wang, M. Muruganathan, and H. Mizuta, *Appl. Phys. Lett.* **105**, 033103 (2014).
- [2] A. Venugopal, L. Colombo, and E. M. Vogel, *Appl. Phys. Lett.* **96**, 013512 (2010).
- [3] R. Nouchi, T. Saito, and K. Tanigaki, *J. Appl. Phys.* **111**, 084314 (2012).
- [4] J. Martin, N. Akerman, G. Ulbricht, T. Lohmann, J. Smet, K. Von Klitzing, and A. Yacoby, *Nat. Phys.* **4**, 144 (2007).
- [5] Y. Zhang, V. W. Barr, C. Girit, A. Zettl, and M. F. Crommie, *Nat. Phys.* **5** 722 (2009).
- [6] C. Casiraghi, S. Pisana, K. Novoselov, A. Geim, and A. Ferrari, *Appl. Phys. Lett.* **91**, 233108 (2007).
- [7] L. Almeida, R. Ramadoss, R. Jackson, K. Ishikawa, and Q. Yu, *J. Micromech. Microeng.* **16**, 1189 (2006).
- [8] S. Majumder, N. E. McGruer, G. G. Adams, P. M. Zavracky, R. H. Morrison, and J. Krim, *Sens. Actuators A* **93**, 19 (2001).
- [9] A. Lumbantobing, L. Kogut, and K. Komvopoulos, *J. Microelectromech. Syst.* **13**, 977 (2004).
- [10] B. McCarthy, G. G. Adams, N. E. McGruer, and D. Potter, *J. Microelectromech. Syst.* **11**, 276 (2002).
- [11] M. Muruganathan and H. Mizuta, *Carbon* **64**, 416 (2013).
- [12] M. Muruganathan and H. Mizuta, *Mater. Res. Express* **1**, 045605 (2014).
- [13] V. E. Dorgan, A. Behnam, H. J. Conley, K. I. Bolotin, and E. Pop, *Nano Lett.* **13**, 4581 (2013).
- [14] J. Kulothungan, M. Manoharan, and H. Mizuta, *Micromachines* **7**, 143 (2016).
- [15] G. Cao, *Polymers* **6**, 2404 (2014).
- [16] H. Sedaghat-Pisheh and G. M. Rebeiz, *IEEE MTT-S Int. Microwave Symp. Dig.*, 2010, p. 304
- [17] B. F. Toler, R. A. Coutu, Jr., and J. W. McBride, *J. Micromech. Microeng.* **23**, 103001 (2013).
- [18] P. H. Fang and W. S. Brower, *Phys. Rev.* **129**, 1561 (1963).
- [19] R. A. Coutu, Jr., J. R. Reid, R. Cortez, R. E. Strawser, and P. E. Kladitis, *IEEE Trans. Components Packag. Technol.* **29**, 341 (2006).
- [20] C. S. Richard, J. Lu, G. Beranger, and F. Decomps, *J. Therm. Spray Technol.* **4**, 342

(1995).

- [21] C. Lee, X. Wei, J. W. Kysar, and J. Hone, *Science* **321**, 385 (2008).
- [22] X. Pang, W. Gao, H. Yang, L. Qiao, Y. Wang, and A. A. Volinsky, *Adv. Eng. Mater.* **7**, 594 (2007).
- [23] A. S. Kao, M. F. Doerner, and V. J. Novotny, *J. Appl. Phys.* **66**, 5315 (1989).
- [24] N. E. McGruer, G. G. Adams, L. Chen, Z. J. Guo, and Y. Du, 19th IEEE Int. Conf. MEMS, 2006, p. 230.
- [25] J. van der Lit, M. P. Boneschanscher, D. Vanmaekelbergh, M. Ijäs, A. Uppstu, M. Ervasti, A. Harju, P. Liljeroth, and I. Swart, *Nat. Commun.* **4**, 2023 (2013).

5 Characterization of graphene NEM switching devices

5.1 INTRODUCTION

Last chapter, the dynamic contact between graphene and naturally oxidized chromium was investigated. Plastic deformation was observed by examining the relationship between contact force and dynamic contact resistance. Contact area increased due to the plastic deformed interface, resulting in the increase of adhesive force and further the irreversible stiction at the contact. To improve the reliability of graphene NEM switches, the stiction failure from the plastic deformation should be minimized. In this chapter, a set of GNEMS switches was fabricated, which increased the deposited thickness of Cr at the bottom of TG to enhance the hardness of contact material. Besides, the geometry of devices was redesigned, which had larger air gap and short beam length to largely increase the mechanical restoring force. Moreover, instead of square concave structure which is applied to the dynamic contact device, periodic pillar pattern was introduced into the bottom surface of the top gate by utilizing the same technique explained in Chapter 3.3.2. Then, more detailed information about the new graphene NEM switches is given in the next section.

5.2 DEVICE STRUCTURE AND DIMENSION

In this study, the graphene NEM switches kept using double-clamped graphene beam with local top electrodes. Bilayer graphene exfoliated from HOPG was used to obtain reliable mechanical properties and low thickness. The layer number was verified by Raman spectroscopy, and 2D components of the measured spectroscopy shown in Figure 5.1 was analyzed by four Lorentzian fitting, which agreed with the reported experiment data [1].

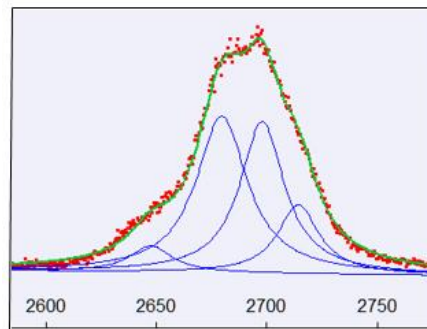


Figure 5.1 2D peak of a graphene Raman spectroscopy with four Lorentzian fitting

Two bilayer graphene-based contact switches were fabricated for characterizing, and detailed parameters of these four devices are listed in Table 1. To achieve stronger mechanical restoring force comparing with the previous study, the shortest length of beam reached to 0.75 μm , and the air gap thickness was increased to 120 nm.

Table 5-1 Device parameters of four measured contact switches

	Previous design		Improved design	
	A	B	C	D
Length of GNR, L (μm)	1.5	1.5	0.75	1
Width of GNR, W (μm)	0.5	0.2	0.4	0.4
Air gap, g_0 (nm)	70	90	120	120
Layer number of graphene	1	multi	2	2

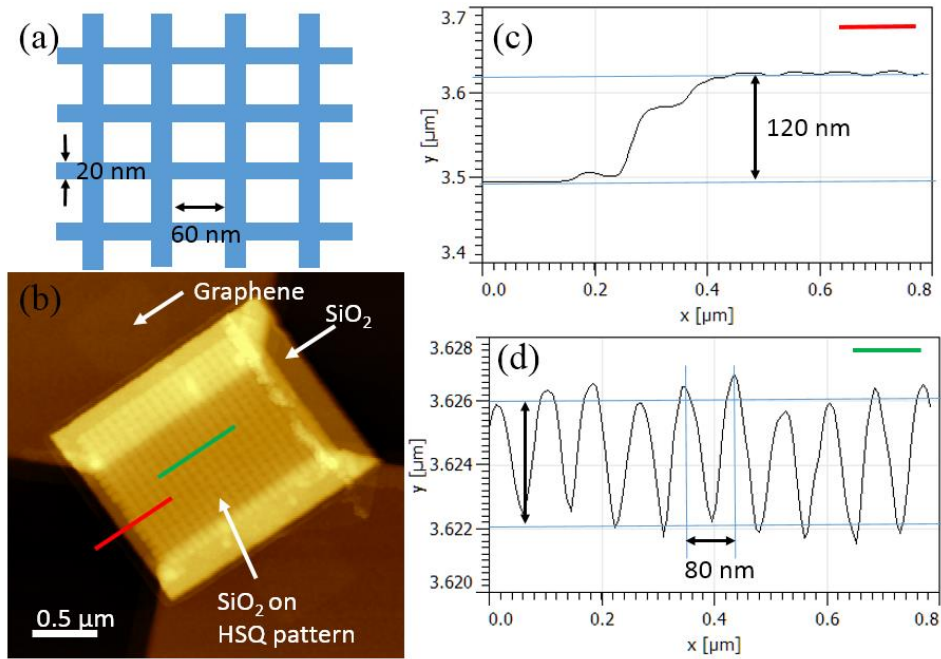


Figure 5.2 (a) Design of a typical net-like pattern of HSQ (b) AFM image of patterned HSQ under the e-beam evaporated SiO₂ (c) and (d) Extracted profiles from red and green lines.

Moreover, the structure of lithographically patterned HSQ was changed, aiming to achieve periodic pillars at the bottom of the local top gate. The designed HSQ pattern with a net-like structure was illustrated in Figure 5.2(a), followed with an AFM image of patterned HSQ under the e-beam evaporated SiO₂. The topology was analyzed from the AFM image, which indicated the total height of HSQ and SiO₂ was around 120 nm. More importantly, thanks to the slanted sidewall of evaporated SiO₂ demonstrated in previous dynamic contact study; saw-like profile was clearly observed with a depth of around 4 nm and ~80 nm interspacing, which was the origin of periodic pillars in TG. Finally, optical and SEM pictures of a fabricated suspended graphene NEM switch with a local top gate were displayed below (Figure 5.3). Large sizes of anchored metal electrodes were intentionally designed, which offered a good mechanical stability after the BHF etching.

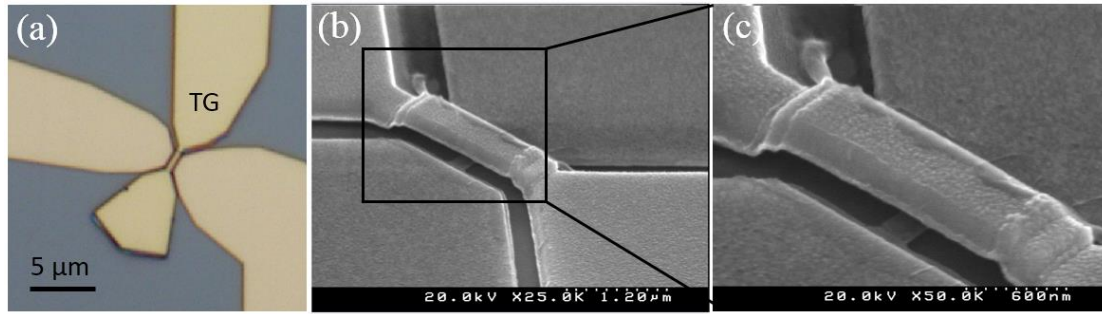


Figure 5.3 (a) Optical image of a fabricated GNEM switch. (b) SEM images of patterned a NEM contact switch with the suspended graphene and local top electrode.

5.3 RESULTS AND DISCUSSION

5.3.1 PULL-IN CHARACTERIZATION

Two devices listed in Table were characterized by the two-terminal measurement configuration which was shown in the inset of Figure 5.4. When gradually increasing the applied voltage on TGs, the current between TG and anchored electrode was monitored. The sudden and sharp increase in current was observed from each of the four GNEM contact switches, which indicated double-clamped graphene beam was physically contacted with the top actuation electrode. The compliance of current was set as 200 nA to avoid the stiction from a high level of current due to the joule heating. Pull-in effect was clearly observed on the four contact switches, and the measured pull-in voltage was 22.45 V (Switch C), 29.9 V (Switch D). Comparing with the previous study, the measured voltage was relatively large, which was due to the shorter beam length and the larger air gap thickness.

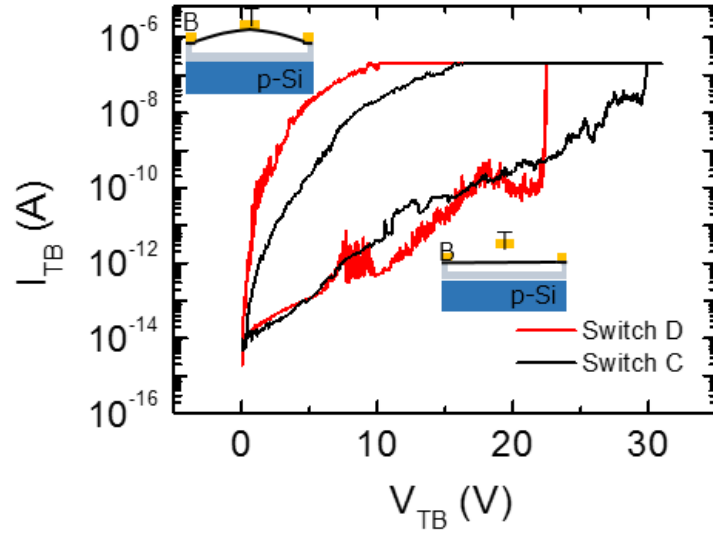


Figure 5.4 Characterization of pull-in effect of four GNEM switches.

As mentioned in the previous chapter, the pull-in voltage of the doubly clamped beam is given by

$$V_{\text{pull-in}} = \sqrt{\frac{8Kg_0^3}{27\epsilon_0 WW_{\text{TG}}}}, \quad K = \frac{32EWt^3}{L^3}, \quad (2)$$

where K is the spring constant of the graphene beam, g_0 is the initial air gap between the suspended top gate and the graphene, ϵ_0 is the electric constant, E is Young's modulus of the material of beam, L and W are the length and width of the GNR, respectively, and t is the beam thickness, which is also considered as the thickness of GNR in this study. W_{TG} is the width of the top actuation electrode. By using the device parameters in Table 5-2, the corresponding analytical values of spring constant and pull-in voltage were listed in Table 5-2.

Table 5-2 Device parameters of four measured contact switches

	Previous design		Improved design	
	A	B	C	D
Length of GNR, L (μm)	1.5	1.5	0.75	1
Width of GNR, W (μm)	0.5	0.2	0.4	0.4
Air gap, g_0 (nm)	70	90	120	120
Layer number of graphene	1	multi	2	2
Measured pull-in voltage (V)	3.4	7.4	29.9	22.45
Effective spring constant (N/m)	0.755	0.673	4.64	3.49

As discussed in Chapter 4, the gap between the analytical values and measured data may attribute to the difference between the assumed flat surface and the surface

modified at the bottom of TG due to the HSQ pattern, and also to the released strain after suspension of the device. Thus, it will be useful to calculate the effective spring constant based on the measured pull-in voltage, which has considered these unknown parameters inside the device. As expected, for the devices with improved design, the effective spring constants were at least 5 times larger than that of previous devices. However, after graphene beams collapsed on the top gates, strong stiction was observed among these four devices by checking, which was indicated by a linear electrical response between the TG and anchored electrode when we applied a small voltage bias. The stiction problem should be clear to improve the reliability of our graphene NEM switch.

5.3.2 TYPE OF DEFORMATION

As the graphene beams were stuck to the top contact surface, the same method used for dynamic contact study was conducted to investigate the type of contact between the graphene and the surface with periodic pillar structures. Measured responses between the applied voltage and the current from Switch A and Switch B after first pull-in were utilized to analyze the contact pressure and contact resistance, which were shown in insets of Figure 5.5. Furthermore, both elastic and plastic deformation models for the contact of graphene and Cr_2O_3 , which were demonstrated in Chapter 4, were compared with the measured data (Figure 4.6). The deformation between graphene and the pillar-structured surface was still plastic deformation, which was consistent with the results in the last chapter. However, if we compare the contact resistance measured from periodic pillar patterned surface with that from concave pattern top gate (Figure 4.6), the resistance from pillar surface was four orders larger than that from concave patterned surface when the contact force was weak, indicating that the real contact area between graphene beam and pillar structure was much smaller than that from the previous study. Less contact area, which was good for graphene NEM switch, had less adhesive force. As the increase of contact force, a relatively fast drop of contact resistance was observed, suggesting a rapid increase of contact area as the graphene beam and pillar deformed. The small contact force is preferred to reduce the stiction force. Since the relation between contact force and contact resistance followed the power law, to achieve low contact force practically, the pull-in voltage of switch should be lower than 0.5 V, which is not realistic to achieve stable pull-out operation

by considering a very weak mechanical restoring force and short range force like vdW force. Besides, plastic deformation was often observed from MEMS contact switches. Another mechanism of stiction needs to be investigated to enhance the reliability of graphene NEM switch.

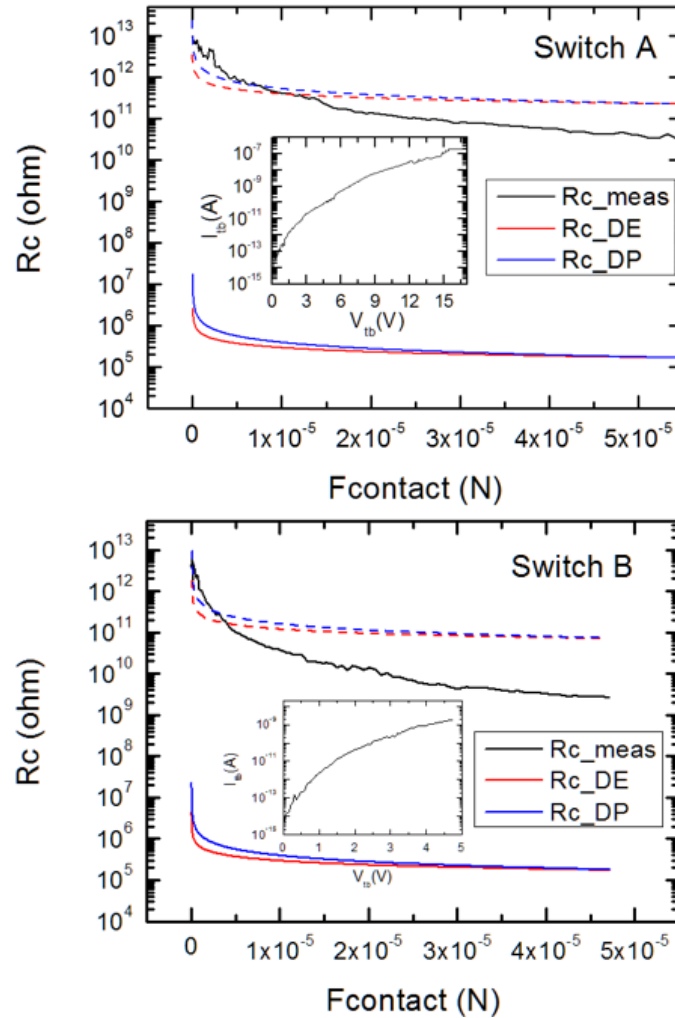


Figure 5.5 Contact force versus contact resistance curves from measured GENM switches A, and B, and two dynamic contact models of elastic and plastic deformations. Dotted lines: shifted contact resistance of two classical models to compare with the measured results. Insets: Measured responses between the applied voltage and the current from Switch A and Switch B after the 1st pull-in.

5.3.3 BI-STABLE NEM SWITCH

In general, during the characterization of a MEMS/NEMS contact switch by sweeping the applied voltage, the main adhesive force, preventing movable element away from the contact electrode, is the electrostatic force due to the polarized dielectric

layer.

In order to reduce the polarization effect inside of the dielectric layer, we modified the measurement configuration as shown in Figure 5.6, which applied voltage to bottom contact electrode and set top gate as ground. By using the reversed configuration, the oppositely polarized charge can be injected into the existed Cr_2O_3 and interacted with the remained charge. This approach was firstly applied to the device A, which had a stiction issue after the 1st pull-in operation. The measurement was conducted under the vacuum condition the room temperature.

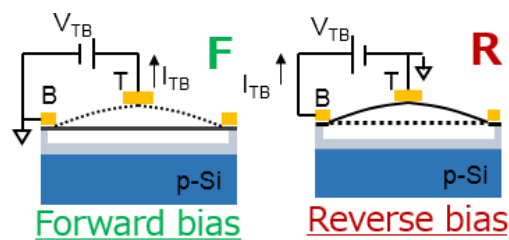


Figure 5.6 (a) Typical measurement configuration for characterizing a NEM switch. (b) New measurement configuration with a reversed biased

As shown in Figure 5.7, interesting results were observed after applying reversed bias for the switch A. Switch A started from an exponential increase in current, suggesting a direct contact between the doubly- clamped beam and the TG. After that, a sudden drop in current was observed as the applied voltage increased. When sweeping the voltage back from high voltage, only small current was measured. We suspected that at the voltage of 17.5 V, the graphene beam was retracted from the top gate and returned to its original position, literally, pull-out effect. For the second characterization, the normal measurement configuration was used again to observe the pull-in operation. As expected, a sharp increase of current was measured at the voltage of 27.8 V, indicating a physical contact. However, the beam was stick to the TG again after the pull-in operation. To pull out the graphene beam, the same method was applied for the third cycle, resulting in a clear drop in current after sweeping the voltages. Another pull-in effect was confirmed after the fourth cycle, which was shown in Figure 5.7.

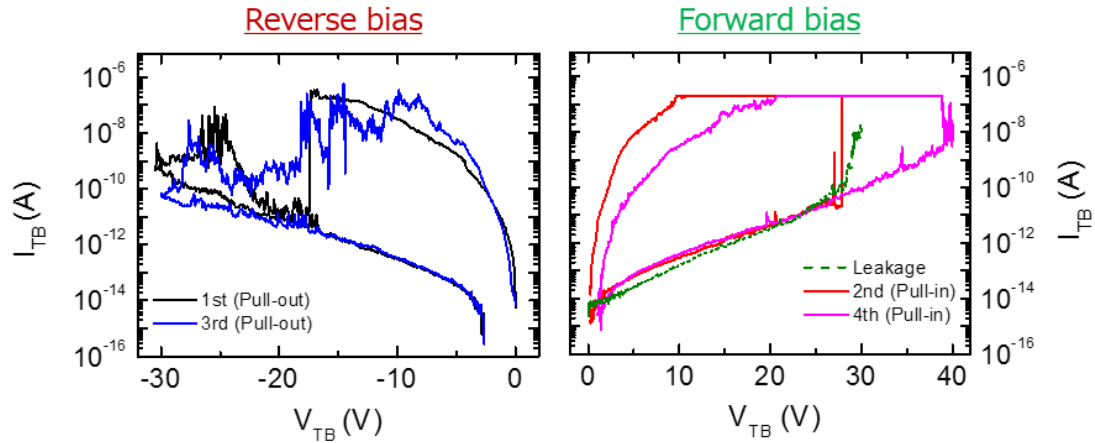


Figure 5.7 Characterization of Switch A with reversed bias configuration and normal switching configuration.

Once combining these four measurement results together (Figure 5.8), we can find that all of these results shared the same level of leakage current, which proved the pull-out of graphene at the first characterization of reversed bias. Besides, the pull-in voltage was shifted to a higher value, owing to the increase of injected charge from the movable graphene beam [2]. The sudden decrease in current was explained by the increase of energy barrier for transporting carriers due to a local oxidation of graphene at the graphene-metal contact [3]. However, our measurement was conducted in a high vacuum environment (10^{-4} mbar), which did not agree with the oxidation scenario. The observed pull-in and pull-out switching behaviour was proposed to be attributable to the polarization and charging effect of the dielectric layer at the bottom of the top gate.

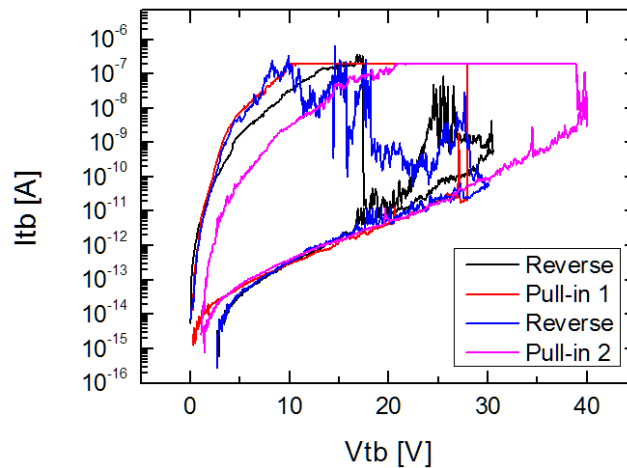


Figure 5.8 Combination of all the four measurement cycles (Switch A).

In this study, the dielectric layer was the naturally grown Cr_2O_3 which is highly disordered, the molecular dipole and intrinsic space charge inside of the Cr_2O_3 layer

polarized when applying the voltage. Moreover, the external spacing charge can easily inject into the dielectric layer since the amorphous Cr_2O_3 had large numbers of defect states. As explained in Chapter 2, the polarized dipole and intrinsic charges in dielectrics under an external electric field behaved opposite polarity to the electrodes. In contrast, the same polarity of free space charges with that of the contact electrode was injected into the dielectric. By injecting opposite sign of spacing charges from the reversed biasing, the magnitude of the internal electric field was decreased, thus reducing the stiction force due to the polarized dielectric. Consequently, the beam was pulled out from the top electrode once the mechanical restoring force overwhelmed adhesive force.

Although, the fabricated switch still suffered from stiction problem due to the polarized dielectric layer, interestingly, the observed bi-stable switching behaviour can be interpreted as a NEM non-volatile memory cell, which perfectly meet the two fundamental requirements, non-volatility and at least two stable states. For our graphene NEM switching device, two distinguished states were corresponding to two beam positions, which were at fully suspended or in contact, which was illustrated in Figure 5.9.

The bi-stable switching characteristics were also observed on Device D when applying the normal and reversed bias voltage. The first six cycles of measurement were shown in Figure 5.10. The graphene NEM memory cell was initially at “0” state. As the applied voltage increased, the device showed the clear pull-in behaviour at the first cycle, indicating the switching operation from “0” state to “1” state. The NEM non-volatile logic cell retain the state “1” when the applied voltage returned to 0 V. In terms of the 1st, the 3rd, and the 5th sweep, reversed bias was applied to inject charges with opposite polarity, resulting in the clear drop in measured current, which suggested the detachment of graphene beam from the contact interface. By performing a reversed bias voltage on the actuation electrode, the logic cell can be turned off from state “1” to “0”. As shown in the 2nd and the 4th cycles, the graphene beam can be pulled up and stuck with the top gate once sweeping the voltage on the actuation electrode, which referred to switch state from “0” to “1”. And the reasons behind the bi-stable characteristics were due to charge injection from metal and graphene to oxide layer, resulting in the charge storage and neutralization.

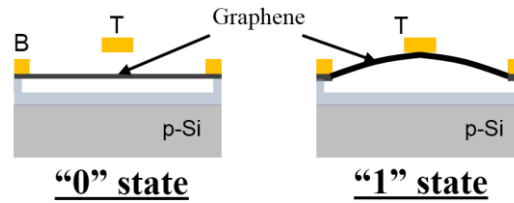


Figure 5.9 Graphene NEM memory states corresponding to the beam positions.

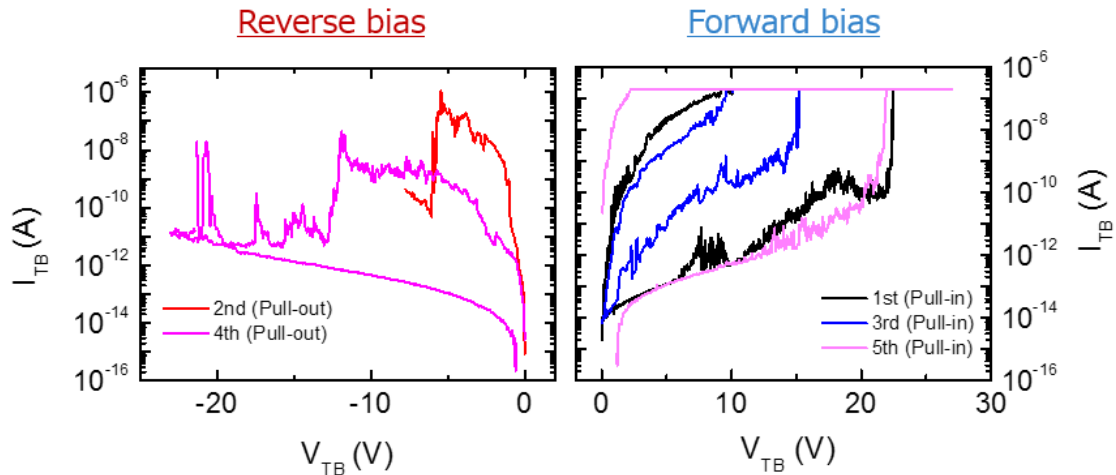


Figure 5.10 Characterization of a bi-stable non-volatile logic cell (Switch D) with reversed bias configuration and normal switching configuration.

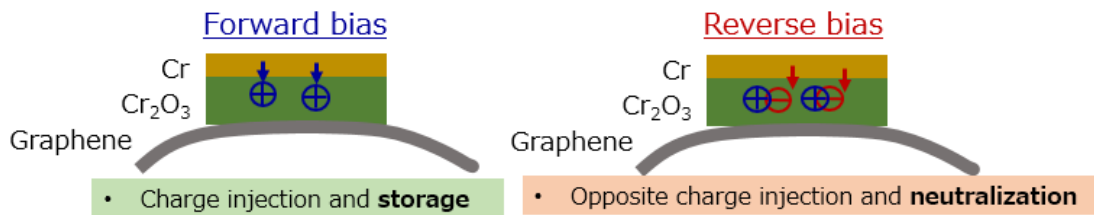


Figure 5.11 Explanation of charge storage when applying the forward bias and reverse bias.

Bi-stable and non-volatile states can be realized via our graphene NEM switch. Previously, Si-based NEM non-volatile logic cell was demonstrated by introducing a charging layer as oxide/nitride/oxide. The role of the oxide charging layer was to store charges, further resulting in non-volatility [4]. Our graphene NEM non-volatile memory cell shared the same concept by introducing the dielectrics (Cr_2O_3) as the charging layer. Two advantages of the graphene NEM non-volatile memory logic cell were extremely low standby power consumption and long retention time. The retention time of the GNEM non-volatile logic, which was determined by the relaxation time of the dipoles and the discharging time of injected charge, can take several days [2]. Utilizing the graphene NEM non-volatile memory cell is promising to overcome the

bottleneck of von Neumann, since the data storage and processing can be performed simultaneously in the non-volatile logic circuit [5].

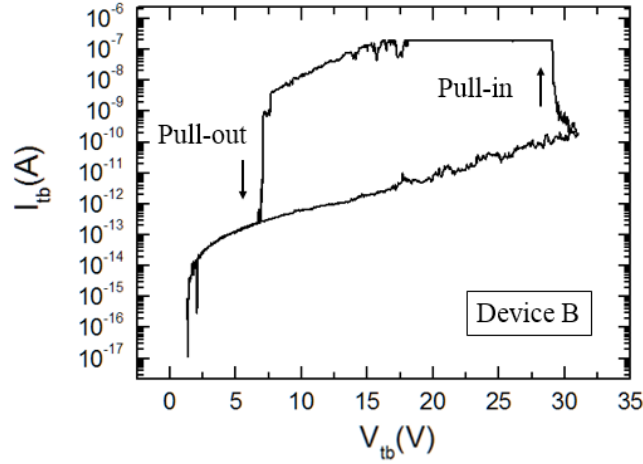


Figure 5.12 Pull-in and pull-out effect measured from Switch B

The device B was kept in vacuum chamber overnight. After 14 hours from the last measurement, another cycle was characterized by the normal two-terminal configuration. As shown in Figure 5.12, clear pull-in and pull-out operations were observed in this cycle. Comparing with previous measurements, weaker effect of dielectric polarization due to the overnight storage was supposed to be the reason behind the pull-out of graphene beam. Although only one cycle of volatile hysteresis was observed on this device due to the dielectric charging issue, it still indicated the flexibility of our graphene NEM switches, which can be integrated as either a non-volatile type or a volatile memory cell.

Finally, the scalability of graphene NEM switches was studied, which was mainly based on the analytical pull-in voltage, regarding as the threshold voltage (V_{th}). The device scaled down in three parameters (beam length L , beam width W and air gap distance g_0). The analytical equation of pull-in voltage considering with the scale factor k was listed below. Figure 5.13 showed the dependence of V_{th} on the channel length L for both Si-based and graphene-based NEM switches.

$$V_{\text{pull-in}} = k^{-0.5} * \sqrt{\frac{256Et^3g_0^3}{27\varepsilon_0L^4}} \quad (5.1)$$

where E is Young's modulus of the material, L and t are the length and thickness of the movable element, g_0 is the gap distance between actuation electrode and movable element. We started the scalability analysis of graphene NEM switches with the

geometry as L (100 μm), W (50 μm), g0 (10 μm) and t (2 μm). In comparison, the parameters of Si-based NEM switching devices were adapted from the reported experiment result (L: 60 μm , W: 10 μm , g0: 220 nm, t: 1.8 μm) [6]. According to the reference, the minimum air gap distance achieved by NEMS device was 4 nm []. Si-based NEM switches cannot shrink to sub-micro range due to the large thickness of the movable element. In contrast, the calculation predicted that graphene-based NEM switches can be downscaled to nm with a relatively low threshold voltage. By further reducing the graphene layer from 2 nm to monolayer graphene (~ 0.4 nm), the scalability of graphene NEM switches is expected to be improved.

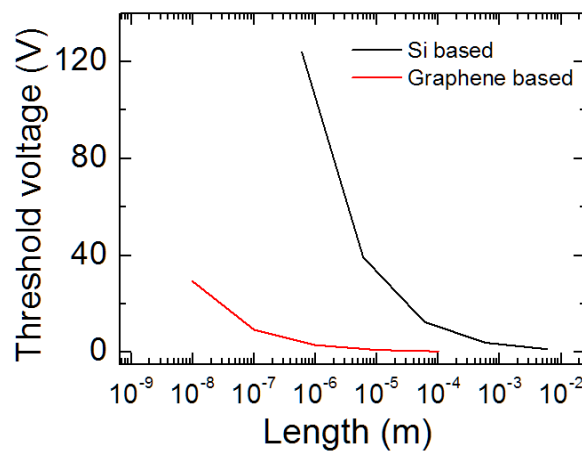


Figure 5.13 A comparison of the scalability between Si-based NEM switching devices and graphene-based NEM switching devices.

5.4 SUMMARY

Four bi-layer graphene NEM switches with local top electrode were characterized. A periodic pillar pattern was introduced into the contact interface to reduce the stiction force. Interestingly, bi-stable switching characteristic was obtained by applying normal and reversed voltage on top electrodes, which was attributed to the charge storage and charge neutralization at the contact (graphene/ Cr_2O_3 /Cr). A graphene NEM non-volatile memory cell was interpreted based on the bi-stable switching behaviour, offering the advantages like extremely low standby power consumption. A hysteresis with clear pull-in and pull-out was measured, which also demonstrated the flexibility in applications from a non-volatile memory cell to a volatile switch. Finally, we have theoretical demonstrated the scalability of graphene NEM switching devices with a comparison of Si-based switching devices.

5.5 REFERENCE

- [1] A. C. Ferrari *et al.*, “Raman Spectrum of Graphene and Graphene Layers,” *Phys. Rev. Lett.*, vol. 97, no. 18, p. 187401, Oct. 2006.
- [2] Z. Peng, X. Yuan, J. C. M. Hwang, D. Forehand, and C. L. Goldsmith, "Top versus bottom charging of dielectric in RF MEMS capacitive switches," *Proc IEEE Asian Pacific Microwave Conference*, pp. 1535-1539, 2006.
- [3] C. Wu, F. Li, Y. Zhang, and T. Guo, “Recoverable electrical transition in a single graphene sheet for application in nonvolatile memories,” *Appl. Phys. Lett.*, vol. 100, no. 4, p. 042105, Jan. 2012.
- [4] W. Y. Choi, H. Kam, D. Lee, J. Lai, and T. J. K. Liu, “Compact Nano-Electro-Mechanical Non-Volatile Memory (NEMory) for 3D Integration,” in *2007 IEEE International Electron Devices Meeting*, 2007, pp. 603–606.
- [5] J. Von-Neumann, “The principles of large-scale computing machines,” *Annals Hist. Comput.* no. 10, p. 243, 1989.
- [6] “Suspended-gate MOSFET: bringing new MEMS functionality into solid-state MOS transistor - IEEE Xplore Document.” [Online]. Available: <http://ieeexplore.ieee.org/document/1609384/>. [Accessed: 13-Feb-2017].
- [7] J. O. Lee, Y. Song, M. Kim, M. Kang, J. Oh, H. Yang & J. YoonA "Sub-1-volt nanoelectromechanical switching device", *Nat. Nanotechnol.* **8** 36-40, 2013.

6 Summary and future work

6.1 SUMMARY

In this thesis, I have demonstrated the study of graphene NEM switches from fabrication to device characterization. From the view of the fabrication process, first of all, graphene NEM switch with local bottom electrode was introduced. The pre-defined trench was used to offer the place deposit the local bottom gate. Both cantilever-type and double-clamped beam type of graphene NEM switches were achieved. The weakness of the trench approach was analyzed, and a comparison with Jian' s fabrication process was discussed. After that, the fabrication method of graphene contact device was given, which was basically followed the conventional method to fabricate the GNR device with a local top gate. In addition, TLM pattern and periodic pattern originating from the high-resolution HSQ pattern were explained in detail, which was introduced into the fabrication process to investigate the static and dynamic contact between graphene and metal.

In terms of the study of graphene contact, both cantilever-type and beam-type of graphene NEM switches with local bottom gate were measured at first, which showed abrupt pull-in at low voltage. However, both of the devices failed due to the stiction from Au-C bonding. After that, graphene contact devices were investigated. We reported graphene-metal contacts by fabricating the transmission line model (TLM) pattern of Au/Cr static contact electrodes onto a graphene nanoribbon (GNR), which was cointegrated with GNR nano-electro-mechanical (GNEM) switches and suspended top electrodes for dynamic contacts. The static contacts showed the linear channel length dependence of total resistance, which was amenable to the standard TLM theory. The slightly negative contact resistance extracted from the TLM analysis was attributable to the inhomogeneity of the GNRs due to the doping from the metal and the substrate. To investigate the Au/Cr – GNR dynamic contact properties, we introduced two types of Au/Cr actuation electrode surfaces with and without a lithographically

patterned periodic array of square concaves, which were expected to reduce the Au/Cr – GNR stiction effectively. For both surface structures, clear pull-in operations were observed for the GNEM switches with doubly clamped mono-, bi-, and multilayer GNRs. However, none of the GNEM switches achieved pull-out operation regardless of the introduction of the periodic surface pattern. It was found for the periodically patterned dynamic contacts that the GNRs first showed global pull-in onto the top surface of the pillar array and then exhibited local pull-in onto the slanted sidewall surfaces of the concave, resulting in an increase in stiction. Such a local pull-in phenomenon was confirmed by 3D FEM simulation. In addition, plastic deformation at the contact, increasing the vdW interaction, was observed as a result of the local pull-in failure mode, which completely hindered the GNRs from pulling out from the contact surface.

Finally, for the characterization of graphene NEM switches, four bi-layer graphene NEM switches with local top electrode were characterized. A periodic pillar pattern was introduced into the contact interface to reduce the stiction force. Clear pull-in and plastic deformation were observed from the initial measurement. Interestingly, bi-stable switching characteristic was obtained by applying normal and reversed voltage on top electrodes, which was attributed to the charge storage and charge neutralization the contact (graphene/Cr₂O₃/Cr). A graphene NEM non-volatile memory cell was interpreted based on the bi-stable switching behaviour, offering the advantages like extremely low standby power consumption. Moreover, the novel NEM non-volatile memory cell offered the possibility to overcome the bottleneck of the von Neumann architecture by realizing data storage and data processing simultaneously. Finally, a hysteresis with clear pull-in and pull-out was measured, which also demonstrated the flexibility in applications from a non-volatile memory cell to a volatile switch.

6.2 FUTURE WORK

From the study, we have known that the plastic deformation between graphene and Cr₂O₃, which is not good for the reliability of device operation. Besides, although the natural oxide layer can prevent the formation of chemical bonding, it also brings the issue of dielectric charging to the contact, which may shift the hysteresis leading to the non-volatile switching behavior. To achieve stable pull-in and pull-out operations of

GNEM switches, it is necessary to modify at least two parameters in the design, which are the thickness of Cr and the thickness of Cr₂O₃. Since Cr is relatively hard among the metal and also resists to the acid etching, increasing the thickness of Cr will be the way to enhance the hardness of contact electrode. Besides, due to the existence of instant oxidation of Cr, there will be no need to wait for the oxidation of Cr over a long time, which can minimize the effect from the dielectric charge, thus stabilizing pull-in and pull-out operation. In addition, the initial contact force is critical to the contact deformation, suggesting to gently increase the applied voltage.

Three-terminal graphene NEM switching device will be certainly developed shortly, which has the big advantage as being fully integrated with the conventional CMOS technology. In addition, three-terminal non-volatile logic cell, which enables to achieve data processing and data storage simultaneously in the logic circuit, will generate a novel logic architecture to overcome the von Neumann bottleneck.

According to Prof. Mizuta's roadmap towards the development of GNEM switches, a graphene to graphene contact NEM switch is under the development. Besides, other two-dimensional materials like boron nitride (BN) and MoS₂ were also recommended to be integrated into the contact interface to improve the stability.